

**AFRL-AFOSR-UK-TR-2011-0058**



## **LiH as Fuel for High Speed Propulsion**

**Claudio Bruno  
Domenico Simone**

**University of Rome  
Mechanics and Aerospace Department  
Via Eudossiana 18  
Rome, Italy 00184**

**EOARD GRANT 10-3091**

**October 2011**

**Final Report for 09 August 2010 to 09 August 2011**

**Distribution Statement A: Approved for public release distribution is unlimited.**

**Air Force Research Laboratory  
Air Force Office of Scientific Research  
European Office of Aerospace Research and Development  
Unit 4515 Box 14, APO AE 09421**

<b>REPORT DOCUMENTATION PAGE</b>				Form Approved OMB No. 0704-0188	
Public reporting burden for this collection of information is estimated to average 1 hour per response, including the time for reviewing instructions, searching existing data sources, gathering and maintaining the data needed, and completing and reviewing the collection of information. Send comments regarding this burden estimate or any other aspect of this collection of information, including suggestions for reducing the burden, to Department of Defense, Washington Headquarters Services, Directorate for Information Operations and Reports (0704-0188), 1215 Jefferson Davis Highway, Suite 1204, Arlington, VA 22202-4302. Respondents should be aware that notwithstanding any other provision of law, no person shall be subject to any penalty for failing to comply with a collection of information if it does not display a currently valid OMB control number. <b>PLEASE DO NOT RETURN YOUR FORM TO THE ABOVE ADDRESS.</b>					
<b>1. REPORT DATE (DD-MM-YYYY)</b> 06-10-2011		<b>2. REPORT TYPE</b> Final Report		<b>3. DATES COVERED (From – To)</b> 9 August 2010 – 09 August 2011	
<b>4. TITLE AND SUBTITLE</b>  <div style="text-align: center; font-weight: bold;">LiH as Fuel for High Speed Propulsion</div>			<b>5a. CONTRACT NUMBER</b> FA8655-10-1-3091		
			<b>5b. GRANT NUMBER</b> Grant 10-3091		
			<b>5c. PROGRAM ELEMENT NUMBER</b>		
<b>6. AUTHOR(S)</b>  Professor Claudio Bruno Dr. Domenico Simone			<b>5d. PROJECT NUMBER</b>		
			<b>5d. TASK NUMBER</b>		
			<b>5e. WORK UNIT NUMBER</b>		
<b>7. PERFORMING ORGANIZATION NAME(S) AND ADDRESS(ES)</b> University of Rome Mechanics and Aerospace Department Via Eudossiana 18 Rome, Italy 00184				<b>8. PERFORMING ORGANIZATION REPORT NUMBER</b>  N/A	
<b>9. SPONSORING/MONITORING AGENCY NAME(S) AND ADDRESS(ES)</b>  EOARD Unit 4515 BOX 14 APO AE 09421				<b>10. SPONSOR/MONITOR'S ACRONYM(S)</b> AFRL/AFOSR/RSW (EOARD)	
				<b>11. SPONSOR/MONITOR'S REPORT NUMBER(S)</b>  <b>AFRL-AFOSR-UK-TR-2011-0058</b>	
<b>12. DISTRIBUTION/AVAILABILITY STATEMENT</b>  Approved for public release; distribution is unlimited. (approval given by local Public Affairs Office)					
<b>13. SUPPLEMENTARY NOTES</b> The U.S. Government is authorized to reproduce and distribute reprints for Governmental purposes notwithstanding any copyright notation thereon.					
<b>14. ABSTRACT</b>  Aim of this report is to present the physical model describing LiH “combustion”, and to discuss by means of some approximated models the main topics associated with thermal fluxes, diffusion rate, lithium vaporization and combustion. To give a rough numerical estimate of the characteristic times involved in a “flight” configuration was investigated.  The analysis performed has shown that LiH, when used as fuel, offer performance comparable with those of commonly used fuels such as LCH4 and LH2.					
<b>15. SUBJECT TERMS</b>  EOARD, Chemical Propulsion, Propulsion, Fuels, Combustion Modeling					
<b>16. SECURITY CLASSIFICATION OF:</b>			<b>17. LIMITATION OF ABSTRACT</b>  <div style="text-align: center;">SAR</div>	<b>18. NUMBER OF PAGES</b>  <div style="text-align: center;">74</div>	<b>19a. NAME OF RESPONSIBLE PERSON</b> Brad Thompson
<b>a. REPORT</b> UNCLAS	<b>b. ABSTRACT</b> UNCLAS	<b>c. THIS PAGE</b> UNCLAS			<b>19b. TELEPHONE NUMBER</b> (Include area code) +44 (0)1895 616163

# **LiH as Fuel for High Speed Propulsion**

## **- Final Report -**

**Prof. Claudio Bruno, Dr. Domenico Simone**

University of Rome "La Sapienza"

claudio.bruno@uniroma1.it, domenico.simone@uniroma1.it

This material is based on research sponsored by the Air Force Research Laboratory, under agreement number FA8655-10-1-3091. The U.S. Government is authorized to reproduce and distribute reprints for Governmental purposes notwithstanding any copyright notation thereon.

The views and conclusions contained herein are those of the authors and should not be interpreted as necessarily representing the official policies or endorsements, either expressed or implied, of the Air Force Research Laboratory or the U.S. Government."

## Contents

<b>I</b>	<b>Introduction .....</b>	<b>3</b>
<b>I.1</b>	<b>The physical model .....</b>	<b>3</b>
<b>I.2</b>	<b>Inside the boundary layer .....</b>	<b>5</b>
<b>I.2.1</b>	<b>The Eckert reference enthalpy method .....</b>	<b>6</b>
<b>I.2.2</b>	<b>Convective heat transfer and shear stress .....</b>	<b>8</b>
<b>I.2.3</b>	<b>Species diffusion .....</b>	<b>10</b>
<b>I.2.3.1</b>	<b>Molecular diffusion .....</b>	<b>11</b>
<b>I.2.3.2</b>	<b>Turbulent mass transport .....</b>	<b>13</b>
<b>I.3</b>	<b>Liquid lithium droplets .....</b>	<b>17</b>
<b>I.3.1</b>	<b>Droplets diameter .....</b>	<b>17</b>
<b>I.3.2</b>	<b>Droplets evaporation and burning .....</b>	<b>20</b>
<b>II</b>	<b>Numerical Simulation -introduction .....</b>	<b>20</b>
<b>II.1</b>	<b>Grain regression model .....</b>	<b>20</b>
<b>II.2</b>	<b>Blowing .....</b>	<b>21</b>
<b>II.3</b>	<b>Numerical approach .....</b>	<b>23</b>
<b>II.3.1</b>	<b>Geometries .....</b>	<b>24</b>
<b>II.3.2</b>	<b>Blowing model .....</b>	<b>25</b>
<b>II.3.3</b>	<b>Test case .....</b>	<b>29</b>
<b>III</b>	<b>Results .....</b>	<b>29</b>
<b>III.1</b>	<b>Cylindrical configuration (<math>Dr = 1</math>) .....</b>	<b>30</b>
<b>III.2</b>	<b>Dump combustor (Configuration Dump05, <math>Dr = 1.1</math>) .....</b>	<b>30</b>
<b>III.3</b>	<b>Configuration Dump11 (<math>Dr = 1.2</math>) and comparisons .....</b>	<b>45</b>
<b>IV</b>	<b>Conclusions .....</b>	<b>57</b>
	<b>References .....</b>	<b>58</b>
	<b>Appendix .....</b>	<b>62</b>

## I. Introduction

Issues concerning LiH thermal decomposition and LiH and Li reactions with air, discussed in a general form in [1], have now to be investigated within the scramjet combustion chamber. Here, thanks to the compression operated by the oblique shock system, the supersonic flow possesses high temperature and high dynamic pressure; entering into the combustion chamber it flows over the solid grain and, as an effect of the shear stresses on the surface, a turbulent compressible boundary layer grows along the chamber while the grain surface regresses; the mass produced by the fuel consumption is injected into the boundary layer and increases its thickness. Thus inside the boundary layer and/or into the core flow the fuel must react with the hot air stream in a few milliseconds increasing the flow temperature and producing the thermal fluxes necessary to gasify the solid grain. For these reasons critical issues are: species diffusion into the hot stream, and their reaction rates with air; these issues in general make gaseous hydrogen preferable as fuel for scramjet application (because its chemical and diffusion times are shorter than those of other fuels when compared to convective time). From this viewpoint the particular behaviour of LiH, that can release gaseous hydrogen by thermal decomposition, together with light and highly reactive lithium, offers an ideal solution to both hydrogen storage and high energy density problems.

Aim of this report is to present the physical model describing LiH “combustion”, and to discuss by means of some approximated models the main topics associated with thermal fluxes, diffusion rate, lithium vaporization and combustion. To give a rough numerical estimate of the characteristic times involved a “flight” configuration was investigated similar to that proposed by Jarymovycz, Yang and Kuo and described in [1].

### I.1 The Physical Model

As a consequence of lithium hydride and lithium thermochemical properties examined in [2] and of the flow conditions into the combustion chamber summarized above, hereinafter we will assume (justifying each assumption in the following sections) the grain “combustion” to be described by the following steps:

- Due to the thermal fluxes produced by combustion in the gas phase the LiH grain surface liquefies; dealing with a phase change we can assume the interface between solid and liquid LiH (or “wall”) to be always at the LiH liquefaction temperature ( $T_{\text{liq}} = 950 \text{ K}$  at 1 atmosphere).
- Thanks to liquid LiH high thermal diffusivity, the small LiH droplets formed at the wall [Litfire], heated by the thermal fluxes reach the LiH decomposition temperature ( $T_{\text{dec}} = 1100 \text{ K}$ ); LiH decomposes fast when compared with the combustor convective time and before reacting with oxygen, its decomposition time being of the order of  $10^{-6} \text{ s}$ ;<sup>45, 46</sup> in fact the LiH reaction rates with oxygen is lower than its decomposition rate (at least by three orders of magnitude) and the oxygen concentration near the surface is too small to allow any kind of oxidation.<sup>24, 65</sup> As stated in [2], LiH does not react with air nitrogen in this range of temperatures.
- As an effect of the thermal decomposition, gaseous hydrogen leaves the drop surface bubbling vigorously and contributing to its fragmentation into smaller liquid lithium droplets. Hydrogen diffuses through the boundary layer and mixed with air oxygen by the highly turbulent stream, burns and releases heat. Some lithium particles

may be trapped into the hydrogen bubbles leaving the surface, burning with oxygen and increasing the heat released by hydrogen combustion.

- Liquid Li droplets are dragged away from the surface (as an effect of the intense shear stresses due to the high speed flow) into the turbulent boundary layer.
- The light liquid lithium droplets thus are mixed with air and hydrogen combustion products present into the boundary layer; passing through the hot gas in the core flow they are vaporized by the thermal fluxes, yielding highly reactive gaseous lithium that, transported by the turbulent stream, burns with air oxygen or with the radicals produced by the hydrogen combustion (see [2]). When allowed by the local oxygen concentration, lithium combustion occurs in proximity of the droplet surface, enhancing liquid lithium vaporization. Again, as stated in [2], liquid lithium doesn't react with air nitrogen in this range of temperatures.
- Where the combustion is well developed the water vapour concentration is so high that it can react with the liquid LiH near the surface; however the net effect of this reaction is the production of LiOH, which at these temperatures decomposes yielding liquid lithium and OH.

## I.2 Inside the boundary layer

The first step to assess the validity of this physical model is the evaluation of thermal fluxes and shear stresses acting on the grain surface. At the combustion chamber entrance, thanks to the compression operated by the oblique shock system, the air flow is at high temperature; thus we are in presence of high stagnation enthalpy over the grain that can heat the surface beyond the LiH liquefaction point. We therefore begin by investigating the heat transfer rate magnitude assuming non reacting flow conditions. The idea is that if the convective thermal fluxes due solely to flow conditions can promote the grain surface liquefaction, the heat released by the combustion surely will be able to feed a self-sustained combustion process.

The simplest preliminary estimate of the convective heat transfer between a wall and a fluid with variable properties is provided by:<sup>66</sup>

$$q_w = St \cdot \rho_e \cdot V_e \cdot (h_{aw} - h_w) \quad (I.1)$$

where  $\rho_e$  and  $V_e$  are, respectively, the flow density and (relative) velocity at the outer edge of the boundary layer and  $St$  is the Stanton number, a dimensionless heat transfer coefficient (representing a nondimensional thermal conductance). Finally  $h_{aw}$  (adiabatic wall enthalpy or recovery enthalpy) is the stagnation enthalpy that the wall-bounding streamline would attain if the wall were perfectly insulated (the corresponding temperature is known as the adiabatic wall temperature or recovery temperature). In fact, if conductive heat transfer within the fluid is neglected, a first law balance shows that  $h_{aw}$  is equal to the stagnation enthalpy of the flow: the free stream kinetic energy is completely converted by the viscosity into internal (thermal) energy. However, because of the small but finite thermal

conductivity of the fluid, thermal energy is conducted away from the stagnation point to the adjacent gas, thus lowering the value of  $h_{aw}$ ; to account for this phenomenon it is customary to introduce a recovery factor  $r$  ( $r < 1$ ):

$$h_{aw} = r \cdot \frac{V_e^2}{2} + h_e(T_e) \quad (I.2)$$

The term  $h_w$  (eqn I.1) is the static enthalpy at the surface, corresponding to the design value for cooled surfaces or to that of the propellant at the phase change temperature. Depending on its value (if higher or lower than  $h_{aw}$ ) it is possible to determine the thermal flux direction (figure 1).

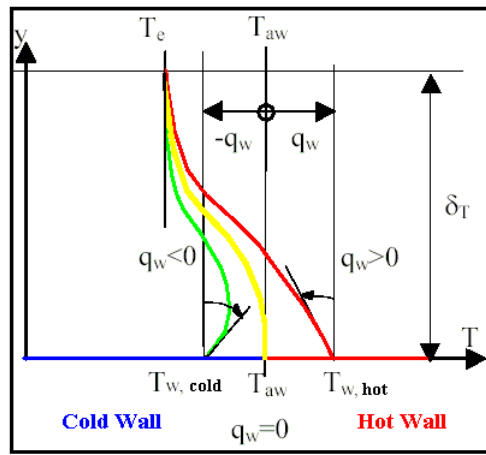


Fig. 1: Convective heat fluxes on a surface where  $V = 0$

To determine the adiabatic wall enthalpy, the recovery factor and the flow properties into the boundary layer, our analysis must account for the flow compressibility; in fact the presence of high velocities in the boundary layer gives rise to such large temperature differences that it is necessary to account for the changes on fluid properties together with that on volume. Furthermore the heat transfer plays an important part in the boundary layer behaviour leading to the appearance of strong interaction between the velocity field and the temperature field. As known in literature, it is possible to describe the compressible boundary layer by means of the same relations holding for incompressible flow (for both laminar and turbulent cases) on condition that the value of density and viscosity are taken at a suitably chosen reference temperature  $T^*$ .<sup>67, 68</sup> There exist in literature various methods to determine  $T^*$ ; for our rough analysis the reference temperature and the heat flux can be evaluated for a turbulent flow on a flat plate by the Eckert reference enthalpy method, assuming zero-pressure gradient, non reacting surface and constant wall temperature.<sup>66</sup>

### I.2.1 The Eckert reference enthalpy method<sup>66</sup>

This method is based on the assumption that a variable properties boundary layer can be cast in a form similar to that of a constant properties boundary layer when computed for a proper “reference” enthalpy (and temperature);

hereinafter the “reference” quantities used in estimating  $q_w$  will be designated with the superscript “\*”. First the reference enthalpy is found by solving simultaneously the following equations:

$$h^* = \frac{h_e + h_w}{2} + 0.22 \cdot r \cdot \frac{V_e^2}{2} \quad (I.3)$$

and

$$r = \sqrt[3]{Pr^*} = \sqrt[3]{\frac{\mu^* C_p}{k^*}} \quad (I.4)$$

This solution is iterative due to the interdependence between  $h^*$  (or  $T^*$ ) and the air properties. After calculating the reference  $h^*$  and the corresponding reference temperature  $T^*$ , the Stanton number for zero pressure gradient, constant wall temperature (and for a flat plate turbulent flow) is:

$$St^* = \frac{0.0296}{(Pr^*)^{\frac{2}{5}} (Re_x^*)^{\frac{1}{5}}} \quad (I.5)$$

with:

$$Re_x^* = \frac{\rho^* V_e x}{\mu^*} \quad (I.6)$$

$$\rho^* = \frac{p_e}{R T^*} \quad (I.7)$$

and

$$Pr^* = \frac{\mu^* C_p}{k^*} \quad (I.8)$$

In this simplified analysis the convective heat transfer at the interface is thus:

$$q_w = St^* \rho^* V_e (h_{aw} - h_w) \quad (I.9)$$

At the same temperature  $T^*$  we can estimate other boundary layer properties such as its thickness  $\delta^*(x)$ :

$$\frac{\delta^*(x)}{x} = \frac{0.370}{(Re_x^*)^{\frac{1}{5}}} \quad (I.10)$$

and the turbulent skin friction coefficient (Reynolds analogy):

$$c_f^* = \frac{0.370}{(Re_x^*)^{\frac{1}{5}}} = 2 St^* (Pr^*)^{\frac{2}{3}} \quad (I.11)$$

### I.2.2 Convective heat transfer and shear stresses

As stated in the introduction, the order of magnitude of convective heat flux and shear stress have been examined using as reference case a “flight” configuration similar to that proposed by Jarymovycz, Yang and K. Kuo.<sup>24</sup> In our case we have assumed the flow entering into a two-dimensional planar combustion chamber with a Mach number  $M = 2$ , static pressure  $p_e = 1$  atm and static temperature  $T = 1400$  K, corresponding to a free stream velocity  $V_e = 1451$  m/s. The chamber length was assumed to be  $L = 1$  m, its height about 20 cm while the LiH grain surface spans 50 cm along the lower boundary of the chamber, thus allowing space for chemical reactions downstream of the fuel grain.

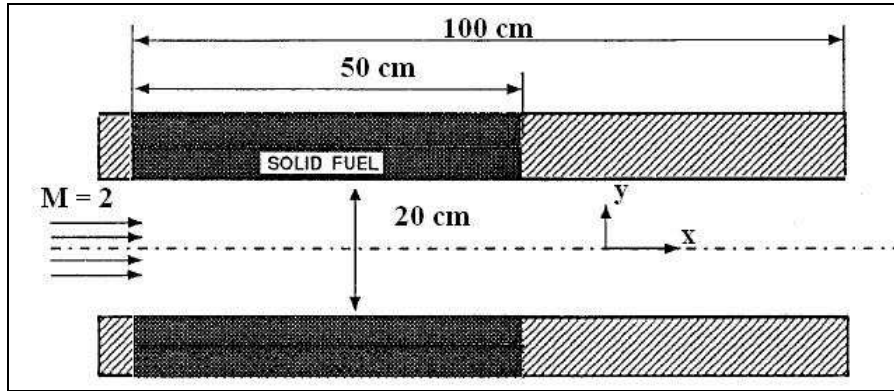


Fig. 2 : Schematic view of the combustion chamber used

The Air and LiH properties (enthalpies, constant pressure heat ratio, viscosity and thermal conductivity) were calculated using the NASA CEA600 database and extrapolating data from the Dry Air Properties Table.<sup>69</sup>

As a first step the reference enthalpy  $h^*$  (and thus the corresponding  $T^*$ ) was calculated using the Eckert method; the first tentative  $Ti^*$ , useful to evaluate at the first iteration the air properties in (I.4), was calculated using the Dorrance formula:

$$T_i^* = T_e \left[ 1 + 0.032 M_e^2 + 0.58 \left( \frac{T_w}{T_e} - 1 \right) \right] \quad (I.12)$$

where  $T_e$  and  $M_e$  are respectively the static temperature and the Mach number of the flow at the edge of the boundary layer while  $T_w$  is the LiH surface temperature ( $T_w = 950$  K) assumed constant, since it is the phase change temperature. Thus using (I.9) and (I.11) and remembering that:

$$\tau_w = \frac{1}{2} \rho_e V_e^2 c_f^* \quad (I.13)$$

the heat fluxes and the shear stress along the grain surface were calculated; results are shown in figure 3.

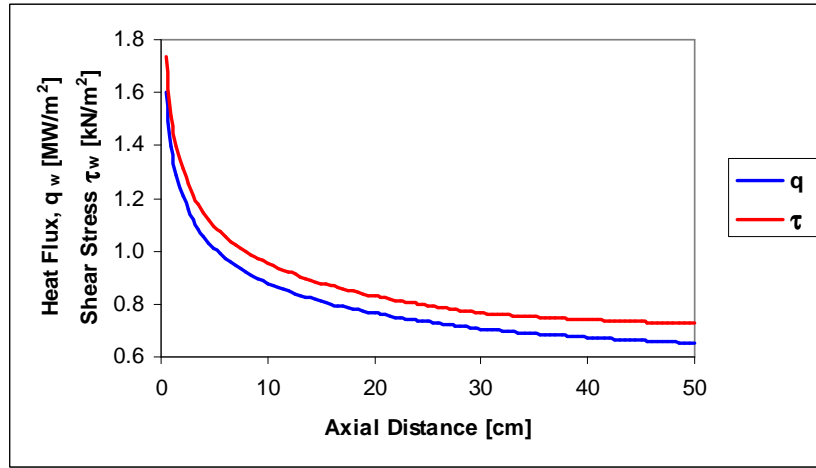


Fig. 3: Heat fluxes and shear stresses

The convective heat fluxes and shear stresses due only to the energy recovery from the flow entering and passing on the surface are high and follow the boundary layer profile. To assess the effect of these thermal fluxes on the surface, a rough estimate of the lithium hydride liquefaction rate was done. We assume that the heat absorbed locally by the interface is the sum of the latent heat of liquefaction (see table 1, where a comparison is made with other fuels used in literature for studies of solid fuelled scramjets (see [1])) and the heat required to increase the liquid LiH temperature from 950 K up to 1100 K ( $\Delta H = 875$  kJ/kg).

Fuel	Average molecular formula [-]	Mass density [kg/m <sup>3</sup> ]	Molar mass [kg/kmol]	Heat of formation [kJ/mol]	Melting point [K]	Thermal conductivity [W/(m-K)]	Heat of gasification [kJ/kg]
Plexiglass or PMMA	(C <sub>5</sub> H <sub>8</sub> O <sub>2</sub> ) <sub>n</sub>	1180	100	-430,5	527.6	0.17-0.19	1300-2700
PolyEthylene	(C <sub>2</sub> H <sub>4</sub> ) <sub>n</sub>	910-965	28	-53,8	400	0.40-0.46	3000-5600

(PE)							
PolyStyrene (PS)	$(C_8H_8)_n$	1050	104	+18,4	510	0.1-0.13	2700
HTPB	$(C_{10}H_{15.538}O_{0.073})_n$	930	138	-51,8	N/A	0.217	1800
Lithium Hydride	LiH	800	7.9	-90.63	950	7.1	2625*

\* latent heat of liquefaction

**Table 1: Comparison among fuels for scrj applications**

In fact, since liquid LiH thermal diffusivity is  $D^{\text{th}} \approx 10^{-6} \text{ m}^2/\text{s}$ , the characteristic heating time of a  $1 \mu\text{m}$  deep liquid layer is about  $10^{-6} \text{ s}$ ; thus we can assume the liquefaction and heating processes to happen by means of a unique continuous step with a total local heat required of about  $3400 \text{ kJ/kg}$ . So, for a thermal flux  $q_w \approx 1 \text{ MW/m}^2$ , corresponding to  $q_w = 1 \text{ J/s} \cdot \text{mm}^2$ , since the liquid LiH density  $\rho_l = 5 \times 10^{-7} \text{ kg/mm}^3$  the local flowrate is  $m_v \approx 0.6 \text{ mm}^3/\text{s}$  corresponding to a local regression rate of the surface of about  $0.6 \text{ mm/s}$ ; since the convective time is of order  $10^{-3} \text{ s}$ , the thickness of the liquid layer formed during one millisecond on the surface is  $h_l \approx 0.6 \mu\text{m}$ . This result will be useful in the following section to assess (together with other considerations) the size of the droplets leaving the surface.

Notice that the surface regression rate (corresponding to the convective heat flux just calculated) is of the order  $0.6 \text{ mm/s}$ ; this value is slightly lower than typical regression velocities of fuels commonly used in space application. However in this “conservative” analysis the heat flux contribute due to gas phase chemical reactions was neglected; this last will enhance strongly the combustion performance by increasing the regression rate and thus the amount of gaseous fuel produced. An example of the thermal power available if all the fuel mass flow rate calculated ( $m_v = 0.6 \text{ mm}^3/\text{s}$ ) reacts in the gas phase is given in table 2 :

Reactants	Products	$\Delta H_{\text{reaction}}$ [kJ/mol]	Thermal Power [W]
Li + O <sub>2</sub>	Li <sub>2</sub> O	242	10.9
Li + O <sub>2</sub> H	Li <sub>2</sub> O + H	435	19.6
Li + O <sub>2</sub> H	LiOH + O <sub>2</sub>	600	27
Li + OH	LiOH	633	28.5
H <sub>2</sub> + O <sub>2</sub>	H <sub>2</sub> O	253	5.7

**Table 2: Thermal powers corresponding to  $m_v$**

where the thermal power obtainable by the lithium in  $m_v$  (assumed to react completely following one among the presented reactions) is compared to that of the reaction among the hydrogen mass contained in  $m_v$  and the air oxygen.

### I.2.3 Species diffusion

As a result of the thermal decomposition gaseous hydrogen is released from near the surface and is transported by the turbulent stream; in the same way liquid lithium drops exposed to the high temperature flow vaporize releasing gaseous

lithium. In the following sections the contribute of both molecular and turbulent mass transport will be valued and compared to assess the ability of these gaseous species to diffuse through the non reacting boundary layer up to the core flow.

### I.2.3.1 Molecular diffusion

As a first step the convective characteristic time  $t_c$  was compared with both hydrogen and gaseous lithium diffusive times defined as:

$$t_d = \frac{\delta^2(x)}{D_{ij}} \quad (I.14)$$

where  $\delta$  is the boundary layer thickness ad  $D_{ij}$  is their binary diffusivity into the air. Data on hydrogen diffusivity are available in [Svelha]<sup>70</sup> while those concerning lithium were calculated (assuming the flow to be nonreacting, f.i., the air to be composed of gaseous oxygen only) using the following relation:<sup>71, 72</sup>

$$D_{ij} = \frac{2}{3} \sqrt{\frac{k_B^3}{\pi^3}} \sqrt{\frac{1}{m_i} + \frac{1}{m_j}} \frac{T^{\frac{3}{2}}}{(r_i + r_j)^2 p} \quad (I.15)$$

where  $k_B = 1.38 \times 10^{-23}$  [J/K] is the Boltzmann constant and  $r_i$  is the Li atomic radius or two times the Van der Waals radius for H<sub>2</sub> and N<sub>2</sub> molecules while  $m_i$  is the mass of gaseous species. To verify the correctness of the values obtained, equation I.15 was used also to calculate the hydrogen diffusivity which was successively compared with [70]. Molecular masses and radii used are reported in table 3:

	Li	H2	O2
mass [kg*10 <sup>-26</sup> ]	1.146	0.332	4.65
radius [pm]	182	240	304

Table 3

Alternatively Kuo suggests a method based on the bifurcation approximation of Bird,<sup>73</sup> used to evaluate the molecular diffusion flux in the Reynolds-averaged Navier-Stokes equations; in this method the diffusion coefficient  $D_{ij}$  is replaced by

$$D_{ij} = \frac{\bar{D}(\bar{T}, \bar{p})}{g_i g_j} \quad (I.16)$$

where  $\bar{D}$  is a reference diffusion coefficient given by:

$$\bar{D} = \frac{1.719 \times 10^{-5}}{\bar{p}} (\bar{T})^{1.659} \quad (I.17)$$

where  $D$  is in  $\text{cm}^2/\text{sec}$ ,  $\bar{T}$  is in Kelvin and  $\bar{p}$  is in atmospheres. The  $g_i$  coefficients are referred to as diffusion factor for species  $i$  and can be calculated from:

$$g_i = \left( \frac{W_i}{26.7} \right)^{0.489} \quad (I.18)$$

For most gas systems, these correlation are within 5% of more exact values for temperatures up to 3000 K. Both methods give results which are in good agreement (for the hydrogen case) with [70]; hydrogen and lithium diffusivities calculated using equation ( I.16) are plotted in figure 4.

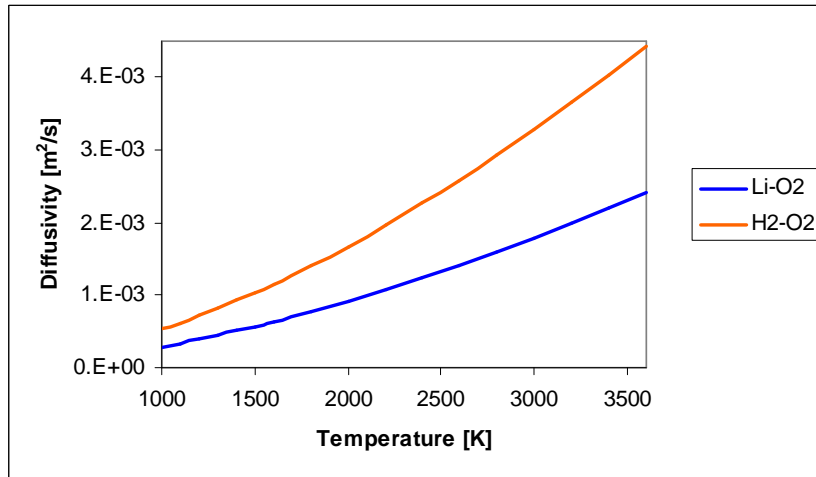


**Fig. 4: Diffusivities as a function of temperature**

Thus values corresponding to the non reacting flow temperature ( $T = 1400$  K; this value was used as conservative lower limits) were used to calculate the characteristic diffusion times; results are shown in figure 5

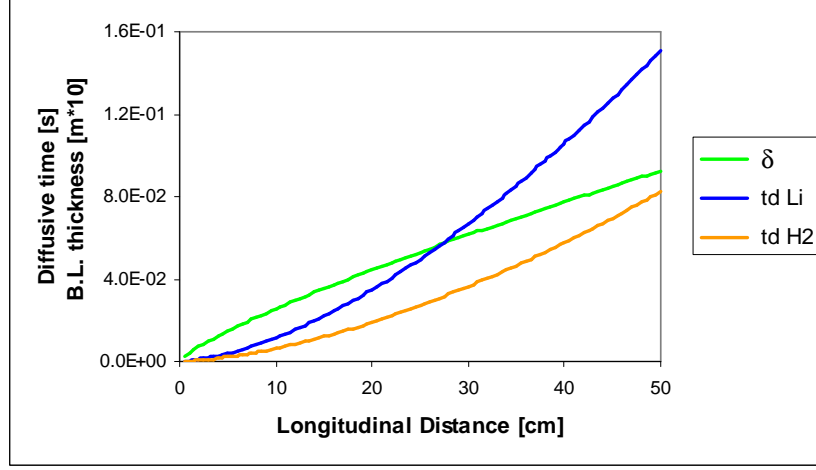


**Fig. 5: Molecular diffusion times and boundary layer thickness along the chamber axis**

As stated before this is the minimum time that both hydrogen and lithium take to diffuse through a non reacting boundary layer along the combustion chamber axis; hydrogen and lithium take a time lower than convective time only in the first part of the grain (about 1/5 of the grain length); however the species diffusion is enhanced by the increase in temperature due to the combustion; furthermore while hydrogen diffuses from the surface, lithium drops vaporize (see next sections) on the way; gaseous lithium thus can diffuse while the vaporizing lithium particle is near the upper border of the boundary layer, so reaching immediately the core flow.

### I.2.3.2 Turbulent mass transport <sup>74</sup>

A simplest estimate of the turbulent mass transport due to the turbulence was made using the concept of eddy mass diffusivity  $D_T$ . As well known in literature, when dealing with the time (Reynolds) averaged Navier-Stokes equations the eddy viscosity  $\nu_T$ , the turbulent thermal diffusivity  $\alpha_T$  and the eddy mass diffusivity  $D_T$  are used to express the correlations among fluctuating velocities, enthalpy and species in terms of mean flow quantities so achieving the equation system closure. In particular the eddy mass diffusivity is connected to the eddy viscosity  $\nu_T$  by means of the turbulent Schmidt number  $Sc_T$ :

$$D_T = \frac{\nu_T}{Sc_T} \quad (I.19)$$

In most of models developed to describe the evolution of turbulent boundary layers the turbulent Schmidt number is assumed to be a constant ( $0.7 < Sc_T < 0.9$ ); this circumstance allows us to evaluate the turbulent mass transport rate by means of the eddy viscosity. This last, in turn, is a local flow property and must be modelled carefully by employing one of the literature-known models. Following the Prandtl mixing-length theory the eddy viscosity was assumed to be:

$$\nu_T = l_m V_T \quad (I.20)$$

where  $l_m$  is the mixing length and  $V_T$  the turbulent velocity. Typically for flows near a wall  $V_T$  is assumed to be proportional to the product of the mixing length and the magnitude of the mean velocity gradient:

$$V_T = l_m \left| \frac{d\bar{u}}{dy} \right| \quad (\text{I.21})$$

The formulation of both  $l_m$  and  $V_T$  is made assuming the boundary layer to be a composite layer consisting of inner and outer regions merging in a overlap layer which represents the turbulent boundary layer core. The extension of this last region increases with Re along the boundary layer thickness.

To describe the velocity and gradients profiles through the boundary layer is useful to define viscous scales that are the appropriate velocity scales and length scales in the near-wall region. These are the friction velocity

$$u^* = \sqrt{\frac{\tau_w}{\rho}} \quad (\text{I.22})$$

and the viscous length scale:

$$\delta_v = \nu \sqrt{\frac{\rho}{\tau_w}} = \frac{\nu}{u^*} \quad (\text{I.23})$$

Thus the distance from the wall measured in viscous lengths (or wall units) is defined as:

$$y^+ = \frac{y}{\delta_v} = \frac{u^*}{\nu} y \quad (\text{I.24})$$

while the non dimensional local mean velocity is:

$$u^+ = \frac{u}{u^*} \quad (\text{I.25})$$

Inner and outer regions, together with their sublayers, are defined on the basis of  $y^+$ : in the viscous wall region ( $y^+ < 5$ ) shear stresses are strongly dependents on the molecular viscosity; in the outer layer ( $y^+ > 50$ ) the viscosity effect is negligible.

Within the viscous wall region, the Reynolds shear stress is negligible compared with the viscous stress in the viscous sublayer ( $y^+ < 5$ ); they are of the same order in the buffer layer ( $5 < y^+ < 50$ ). Furthermore increasing Re the fraction of the boundary layer occupied by the viscous wall region decreases: in fact,  $y^+$  being similar to a local Reynolds number, we can write:

$$y^+ \Big|_{y=\delta} = \frac{\delta}{\delta_\nu} = \frac{u^* \delta}{\nu} = \text{Re}^* \quad (\text{I.26})$$

showing that  $\delta_\nu / \delta$  varies as  $\text{Re}^{*-1}$ .

Using the viscous scales together with equations (IV.24) and (IV.25) the mixing length definitions and velocity gradients obtained by the universal law of the wall can be summarized in each sublayer as:

**Inner layer – viscous (laminar) sub-layer** (  $y^+ < 5$  ) : in this region velocity and transversal velocity gradient are given by:

$$u^+ = y^+ \quad \text{and} \quad \left[ \frac{du}{dy} \right] = \frac{u^{*2}}{\nu} \quad (\text{I.27})$$

while the mixing length is defined by the van Driest equation:

$$l_m = ky \left[ 1 - \exp \left( -\frac{y^+}{A^+} \right) \right] \quad (\text{I.28})$$

where the suggested constant values for  $k$  and  $A^+$  are respectively 0.4 and 26.

**Inner layer -buffer sub-layer** (  $5 < y^+ < 30$  ) : in this region velocity and transversal velocity gradient are given by:

$$u^+ = -3.05 + 5.0 \ln y^+ \quad \text{and} \quad \left[ \frac{du}{dy} \right] = \frac{u^*}{0.2 y} \quad (\text{I.29})$$

while the van Driest mixing length equation is still valid.

**Overlap region** (  $30 < y^+; \quad y < 0.2 \delta$  ) : here velocity and transversal velocity gradient are given by:

$$u^+ = 5.5 + 2.5 \ln y^+ \quad \text{and} \quad \left[ \frac{du}{dy} \right] = \frac{u^*}{0.4 y} \quad (\text{I.30})$$

and the mixing length is:

$$l_m = ky \quad (\text{I.31})$$

where  $k = 0.41$  is the Kendall constant.

**Outer layer - wake region** (  $y > 0.2 \delta$  ):

$$u^+ = 5.5 + \frac{1}{k} \ln y^+ + \left[ \frac{\Pi}{k} w\left(\frac{y}{\delta}\right) \right] \quad (\text{I.32})$$

where  $k$  is the Kendall constant and the term in squared brackets is a function called the law of the wake; in particular for zero pressure gradient flow the *wake strength parameter*  $\Pi = 0.48$  and the *wake function*  $w$  is:

$$w\left(\frac{y}{\delta}\right) = 2 \sin^2\left(\frac{\pi y}{2 \delta}\right) \quad (\text{I.33})$$

Thus the velocity gradient is:

$$\left[ \frac{du}{dy} \right] = \frac{u^*}{k y} + u^* \frac{2\pi \Pi}{\delta k} \sin\left(\frac{\pi y}{2 \delta}\right) \cos\left(\frac{\pi y}{2 \delta}\right) \quad (\text{I.34})$$

while the mixing length is assumed to be a constant equal to:

$$l_m = 0.09 \delta \quad (\text{I.35})$$

Using equations (I.29) – (I.35) together with (I.19), (I.21) velocity profiles, mixing lengths and turbulent mass diffusivities were calculated along the boundary layer thickness at two locations ( $x = 25$  cm and  $x = 50$  cm); the velocity range available in each region of the boundary layer at  $x = 25$  is summarized in table 4 while the turbulent mass diffusivities profiles are plotted in figure 6.

	Vert. Distance [mm]	Velocity [m/s]
$y^+ < 5$	$y < 0.025$	$0 < u < 350$
$5 < y^+ < 30$	$0.025 < y < 0.135$	$350 < u < 750$
$y < 0.2 \delta$	$0.135 < y < 1.8$	$750 < u < 1100$
$y > 0.2 \delta$	$1.8 < y < 9$	$1100 < u < V_e$

Table 4

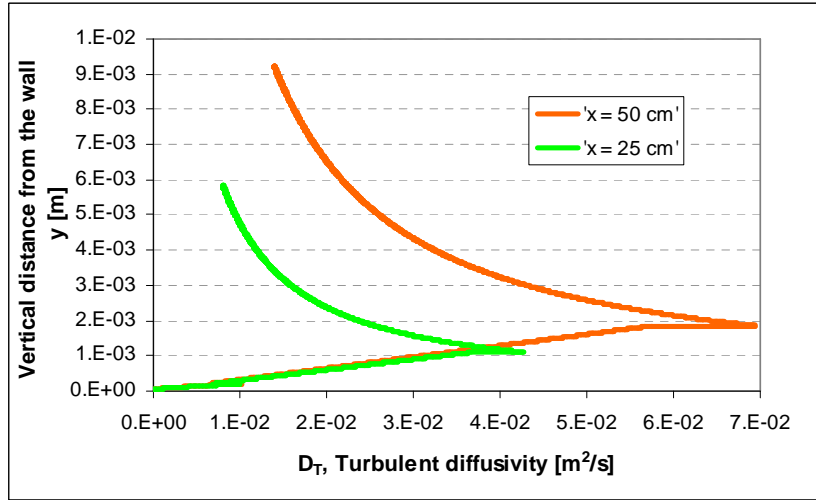


**Fig 6: Turbulent mass diffusivity profiles at  $x = 25$  and  $x = 50$**

As shown by the plot the turbulent mass diffusivity is more than one order of magnitude larger than the hydrogen molecular diffusion coefficient; maximum values are localized in the core of the overlap region where the molecular viscosity is negligible. Furthermore  $D_T$  increases with the longitudinal distance allowing diffusion time lower than convective time along all the grain.

### I.3 Liquid Lithium Droplets

While the gaseous hydrogen diffuses and burns, droplets of liquid lithium produced by LiH thermal decomposition are dragged away along the combustion chamber. The analysis of their behaviour is important to understand the impact of a liquid phase on the engine final performance.

In fact due to its high boiling temperature and latent heat of vaporization (see [2]), liquid lithium acts as a heat sink: depending on thermal fluxes, droplet diameter and time of residence into the combustion chamber, it can exit as a unburnt liquid from the nozzle taking away the heat trapped along the path; otherwise it can vaporize (partially or completely) and burn so releasing heat useful to increase the flow temperature.

Moreover from the point of view of the mathematical model development, the presence of a liquid phase evolving into a gaseous stream poses nontrivial problems that must be simplified by modelling the droplet behaviour.

A brief analysis of droplets evolution based on simplified models is presented in the following sections.

#### I.3.1 Droplets Diameter

Assuming known the temperature path and the thermophysical properties of the heterogeneous mixture, the driving factor in the droplet lifetime analysis is the droplet diameter. Large drops could vaporize and burn with characteristic time longer than the particle residence time in the combustion chamber.

To assess the approximate dimension of the droplets for the case under examination we move from some simple considerations:

- Depending on the solid grain solution design we can decide a priori the most effective granulometry. As an example, if LiH is dispersed into HTPB or other polymeric binders, we can use (as in the case of AP/HTPB solid propellant) LiH particles having diameters of the order of few micrometers. These particles once liquefied, produce droplets with diameters of the same order of magnitude.
- When designed without a binder, the whole grain surface is composed of solid LiH: as shown in the preceding sections thermal fluxes liquefy the grain surface producing a thin film of liquid LiH which height is of the order of few micrometers. When dragged away, this film can produce droplets with maximum diameters of the same order of magnitude.
- As shown in the experiments presented (see [2]) the gaseous hydrogen formed by thermal decomposition of LiH bubbles violently into the droplet, favouring its fragmentation into smaller particles.

Moreover these droplets when dragged away from the surface are thrown into a high speed turbulent stream; the flow dynamic pressure acting on the droplet surface contributes to its fragmentation into smaller droplets.

The problem of aerodynamic break-up of liquid drops has a large literature. Most works analyze the break-up dynamics as a function of the ratio between the aerodynamic force acting on the particle and the restoring force due to surface tension; this non dimensional ratio is defined as the Weber's number :

$$We_d = \frac{\rho_g v^2 D}{\sigma} \quad (I.36)$$

where  $D$ ,  $v$ ,  $\sigma$  and  $\rho$  are respectively the droplet diameter, velocity (relative to the stream), surface tension and the air density. As stated by Pilch & Erdman (1987) the break-up dynamic by means of shadowgraph techniques,<sup>75</sup> increasing the flow speed the break-up dynamic range from the simple separation into smaller droplets ( $We \approx 12$ ) up to a catastrophic nebulization into tens of very small droplets ( $We > 350$ ); conversely, for assigned liquid properties and flow speed there is only one range of drop diameters compatible with a specific break-up dynamics regime. It is possible thus to define a Weber number (called Critical Weber's Number  $We^c$ ) under which the drop break-up cannot be observed within times significant in practical applications. An experimental correlation between the critical Weber and the Ohnesorge number:<sup>76</sup>

$$Oh = \frac{\mu_l}{\sqrt{\rho_l \sigma D}} \quad (I.37)$$

where  $\mu_l$ ,  $\rho_l$  and  $D$  are respectively the droplet viscosity, density and diameter was proposed by Brodkey (Figure 7)<sup>77</sup>

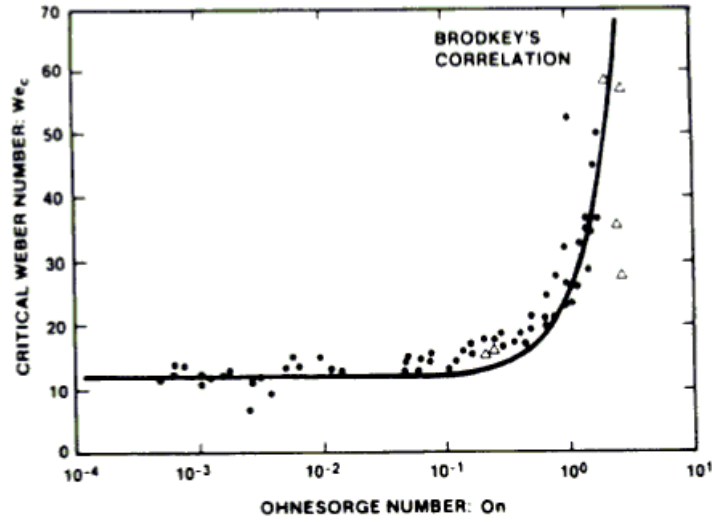


Fig. 7: Brodkey correlation

As shown in the picture, the critical Weber is about 12 for Ohnesorge numbers  $< 0.1$ , increasing dramatically for  $Oh > 0.1$ . In other words, if  $Oh > 0.1$  (e.g. when the fluid viscosity increases) the drops break-up becomes quite impossible. The Brodkey correlation can be expressed analytically as:

$$We_d^c = 12 \left( 1 + 1.077 Oh^{1.6} \right) \quad (I.38)$$

To determine the maximum diameter compatible with the flow condition for the case under examination, we have calculated using (I.37) and (I.38) the critical liquid lithium Ohnesorge number as a function of the drop diameter, assuming its viscosity, density and surface tension at the LiH decomposition temperature (about 1100 K); then the flow Weber number was calculated as a function of the drop diameter for air speeds ranging from 500 up to 1500 m/s assuming its density valued at the air stream temperature at the combustion chamber entrance ( $T = 1400$  K). Results are plotted in figure 8.

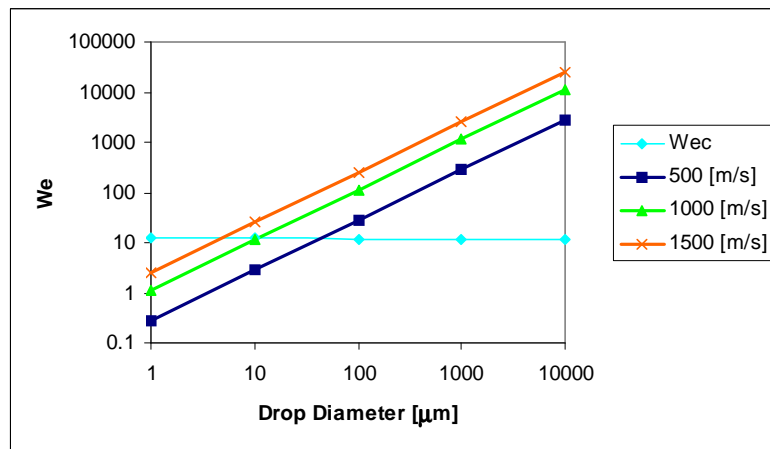


Fig 8: Liquid Li drop diameter compatible with the SCRJ flow conditions assumed

As shown in the picture for high speed flow the Weber number of droplets having diameters  $> 50 \mu\text{m}$  is always greater than the critical Weber number; in particular, for the flow conditions expected in the core of the boundary layer, the maximum allowed droplet diameter is of order of  $10 \mu\text{m}$ .

### **I.3.2 Droplet evaporation and burning**

Once the droplets maximum diameter is known we can estimate its gasification rates and lifetime, a key issue in evaluating the heat subtracted or added by lithium to the flow while moving along the combustion chamber. Incomplete evaporation could in fact signify potential heat trapped into the drop and transported out of the combustor, thus ineffective for propulsion. Conversely, fast evaporation yields gaseous lithium that can react while vaporizing, or diffuse away from the drop (e.g.; when the oxidizer(s) concentration is too small to allow any reaction) and burn. This second case allows us to justify the idea of lithium hydride as a powerful dual-fuel system: in fact we can roughly consider LiH as a special hydrogen storage system in which the storage medium (lithium) is, in turn, a highly energetic fuel.

With appropriate and simple assumptions, the evaporation and burning of spherical liquid droplets is relatively simple to analyze; for both cases we have used models based on closed-form analytic solutions of the simplified governing conservation equations and that are well known in the literature.<sup>71, 72</sup> These solutions have allowed us to explore the influence of droplet size and ambient conditions on droplet evaporation and burning times (see Appendix A1) and to definitively conclude that almost all liquid drops vaporize and burn before exhausting from the combustion chamber, and contribute to the heat release in the airstream.

## **II Numerical simulation - Introduction**

As stated in [2], the attention of almost all supersonic combustion researchers being focused on liquid fuels, numerical and experimental data related to solid fuel scramjet study are quite scarce or nonexistent in the open literature. For this reason, to simulate the LiH fuelled SFSCRJ we have investigated the geometrical configurations and the “flight” conditions presented in [1].<sup>21-25</sup>

In this section we will focus on issues associated with the boundary conditions, with particular attention to the injection of mass from the grain surface (blowing effect).

Then the numerical method will be described, stressing the solution adopted (the “sources” method) to account for the blowing and its effect on the boundary layer.

### **II.1 Grain regression model**

From the physical viewpoint a solid fuelled scramjet presents many similarities with hybrid rockets; the oxidizer diffuses into the boundary layer and reacts with the gaseous fuel pyrolyzed and released by the solid grain surface. It is thus reasonable to assume (accounting for the specific differences) one among the well known models present in the open literature to investigate the surface regression.

The most plausible (and used) model of hybrid combustion was developed by Marxman and Gilbert in 1963.<sup>79, 80</sup> It is based on the concept of diffusive flame; in a hybrid system the combustion is localized in a narrow zone of the boundary layer where the air oxygen diffusing from the main stream meets the fuel released by the surface. As stated by Carmicino this feature allows to study of flame zone as a discontinuity of the temperature gradient and of the mixture composition.<sup>80</sup>

In this model the grain regression rate is governed by the local thermal flux at the surface; in fact we can write:

$$\rho_g v_g = (\rho v)_w = \frac{\dot{q}_w}{H_v} \quad (\text{II.1})$$

where  $\rho_g$  is the density and  $v_g$  the velocity of the gaseous fuel leaving the surface;  $\dot{q}_w$  (J/m<sup>2</sup>s) is the thermal flux at the wall while  $H_v$  (J/kg) is, in general, the total heat required to vaporize the solid fuel. In the case of a LiH grain, the surface temperature being that of the phase change (LiH solid to liquid; 950 K),  $H_v$  accounts for the heat necessary to vaporize and decompose LiH: as discussed in [2],  $H_v = 11$  MJ/kg.

The equation describing the regression rate  $\dot{r}$  is obtainable using equation II.1:

$$\rho_s \dot{r} = \rho_g v_g = (\rho v)_w = \frac{\dot{q}_w}{H_v} \quad (\text{II.2})$$

that is:

$$\dot{r} = \frac{\dot{q}_w}{\rho_s H_v} \quad (\text{II.3})$$

Thus the key point of the model is the evaluation of thermal flux at the surface; neglecting the conduction heat exchange inside the grain, total thermal flux is the sum of radiative and convective heat fluxes. This last, in turn, is affected by the injection of gaseous fuel (at 950 K) from the surface.

## II.2 Blowing

To assess the impact of the fuel injection (also known as blowing) from the surface on the convective heat flux, we must account for its influence on the local velocity profile in the boundary layer. In fact the heat transfer coefficient is determined using the Stanton number, which, in turn, is computed from the skin friction coefficient calculated by using the wall functions.

The first theoretical analysis of blowing was made in 1942 by H. Schlichting; successively experimental as well as theoretical investigation have been performed by J. C. Rotta. Figures 9 – 10 show some of Rotta's results.<sup>68</sup>

Injecting gas from the surface, the boundary layer thickness grows. Figure V.4 shows the variation of momentum thickness  $\delta_2(x)$  along a porous flat plate with homogeneous blowing (and suction) at various values of the blowing velocity ( $v_w$ ) at the wall. In this case the external velocity was  $U_e = 20$  to 30 m/s and the normal wall velocity ranged from  $v_w = -0.1$  m/s (suction) up to 0.13 m/s (blowing).

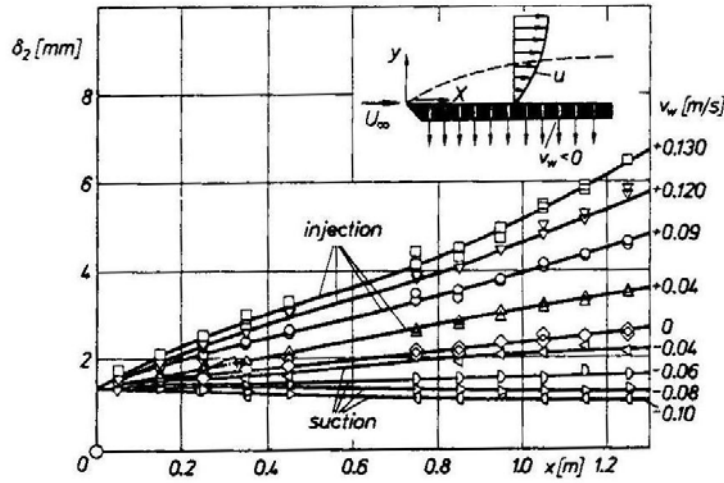


Fig 9 : Momentum thickness variation along a flat plate with blowing and suction <sup>68</sup>

As a consequence of this variation, the velocity profiles in the boundary layer change; to calculate the new profiles, Rotta performed a theoretical formulation, based on the Prandtl's mixing length assumption, that is summarized in the following equation:<sup>68</sup>

$$\frac{u}{v_*} = \frac{1}{x} \ln \eta + C + \frac{1}{4} \frac{v_w}{v_*} \left( \frac{1}{x} \ln \eta + C \right)^2 \quad (\text{II.4})$$

where  $\eta = y v_* / \nu$  is the nondimensional distance from the wall,  $\nu$  the viscosity, and  $v_* = (\tau_w / \rho)^{1/2}$  is the friction velocity.

Curves calculated by Rotta using this equation are plotted in figure 10 ,while figure 11 shows a comparison between theoretical and experimental data.

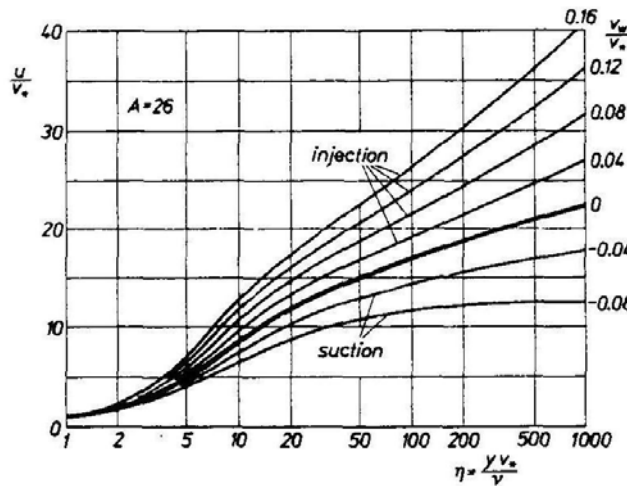


Fig. 10 : Velocity distribution in the B.L. according to eqn. II.10

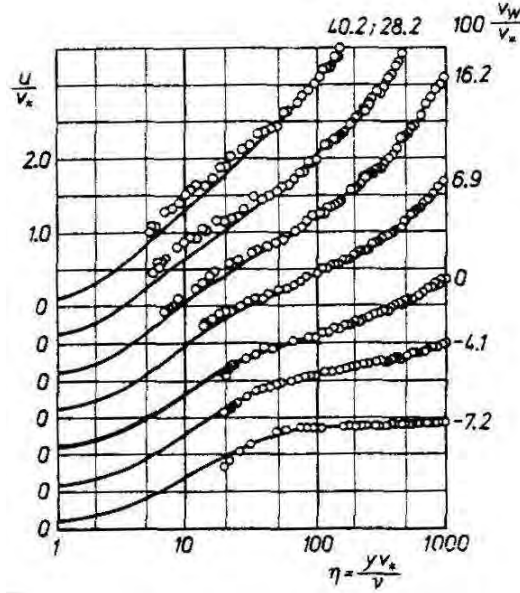


Fig 11 : Comparison between theoretical (lines) and experimental (circles) data

The injection of a gas through a porous wall into a compressible flow, up to Mach 3.6, was investigated by L. C. Squire; its calculations showed that Rotta's assumption were still valid leading to satisfactory results.

So, what happens really in a scramjet combustor chamber? High temperature (1450 K) and high flow velocity (1400 m/s) indicate high friction velocities along the grain (up to 90 m/s). At the same time, for regression rates of order 1 mm/s (or less), from equation II.4 we can see that the expected blowing velocities are of order of few m/s: thus the  $v_w/v_*$  ratio is very small, of order of 0.01. Now, observing figure 11, we can see that, for  $\eta < 20$ , the  $u/v_*$  ratio is  $< 0.1$ . This means that the blowing impact on velocity profiles and heat fluxes at the wall is (in this case!) negligible. This assumption however does not account for the cooling effect due to the gas injection temperature; furthermore there are zones in which the boundary layer behaviour does not agree with the theoretical model developed for a flat plate (e.g: in the flameholder recirculation zone or in regions with shock-boundary layer interactions). In these regions, the blowing effect will be investigated analyzing simulation results.

### II.3 Numerical approach

Our simulations will be carried on using FANS and an axisymmetric domain. Numerical computations are carried out using the Fluent™ 6.3 computational fluid dynamics package.

### II.3.1 Geometries

The geometries considered in this analysis (hereinafter referred respectively as cylindrical and dump combustor) are shown in figure 12 and 13.

Figure 12 shows the longitudinal half-section of the cylindrical combustor.

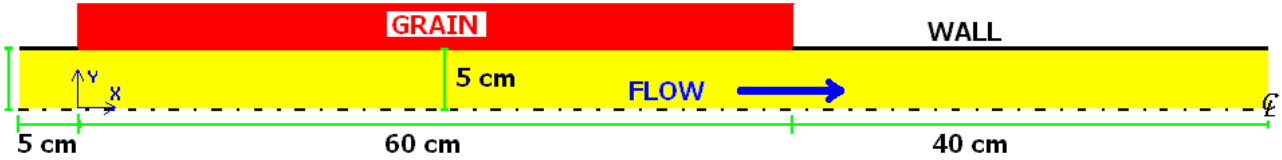


**Fig 12: Cylindrical combustor**

As in the cases investigated by Jakymowycz, Yang and Kuo, and by Ben-Arosh and Gany, the LiH grain is located along the upper surface of the 2-D half-section, with an inlet height of 5 cm; the LiH grain, 60 cm long, is located after a short adiabatic wall (5 cm, the inlet prosecution); then another adiabatic wall (or inert plate), spanning 40 cm along the chamber, is the final part of the combustor.

Figure 13 shows the longitudinal half-section of the dumped combustor (configuration Dump1).

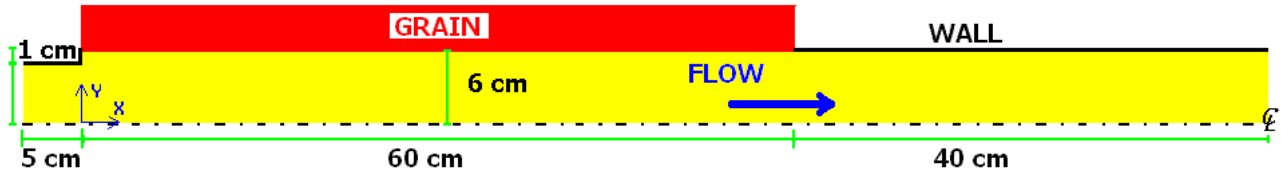


**Fig 13: Dump combustor (configuration D1)**

The dump combustor differs from the cylindrical one for the presence of a sudden expansion, with a dump height of 1 cm.

We have also investigated a third dump configuration (configuration Dump05), that differs from Dump1 only in the dump height (0.5 cm).

The numerical technique is a finite volume approach with quadrilateral control volumes and structured mesh. For all the calculations we use a Cartesian grid. In particular we have used three different meshes:

The cylinder configuration (fig 12) has a grid composed by 155000 cells: in the longitudinal direction over the grain the grid spacing is regular with a uniform 0.5 mm mesh. The mesh increases downstream the grain, with the largest grid measuring 2 mm in length. In the vertical direction, the grid has an exponential progression with an exponential ratio of 0.17 and the smallest grid (near the surface) measuring 50μm in height.

The Dump1 configuration of the dump combustor (fig 13) has a grid composed by 216900 cells: in the longitudinal direction over the grain the grid spacing is regular with a uniform 0.25 mm mesh. The mesh increases downstream the grain, with the largest grid measuring 2 mm in length. In the vertical direction, the grid has an exponential progression with an exponential ratio of 0.11.

Finally the Dump05 configuration of the dump combustor has a grid composed by 162900 cells: in the longitudinal direction over the grain the grid spacing is regular with a fixed mesh of 0.25 mm. The mesh increases downstream the grain, with the largest grid measuring 2 mm in length. In the vertical direction, the grid has an exponential progression with an exponential ratio of 0.11.

Even though a flow with injection of fluid normal to a wall can lead to intrinsic instabilities,<sup>81</sup> we have assumed a steady state approach using a coupled, implicit, second order upwind formulation scheme. The turbulent equations are modelled using a standard k-ε model.<sup>21 – 25, 81, 82</sup>

The method adopted to implement the boundary condition at the grain surface requires some detailed considerations and will be presented in the following section.

For the gas phase combustion we have adopted a six species simplified mechanism involving the following reactions:

LiH decomposition:<sup>45, 65</sup>



One-step reaction for hydrogen combustion:<sup>65, 82</sup>



and one-step reaction for lithium oxidation:<sup>63, 64, 65</sup>



This mechanism does not account for backward reactions since their characteristic times (as stated in [2]) are higher than flow convective time. The coupling between chemical kinetics and turbulence is modelled using the Eddy Dissipation Concept (EDC) model. A description of the Fluent<sup>TM</sup> solver along with k-ε and EDC models is available in Fluent User's Guide manual.<sup>82</sup>

Thermodynamic data (formation enthalpy and entropy at 298.15 K, constant pressure specific heat) data for each chemical species have been calculated using the CEA2 database; in particular, we have calculated the constant pressure specific heats from 300 K up to 6000 K and successively we have implemented them in Fluent by means of polynomials.

In the same range of temperatures (300K -6000K) we have calculated all the molecular viscosities μ using the following equation (from kinetic theory):

$$\mu = \frac{2}{3} \frac{1}{\sigma} \sqrt{\frac{mkT}{\pi}}$$

where  $k = 1.38 \times 10^{-23}$  [J/K] is the Boltzmann's constant,  $m$  the mass of a molecule and  $\sigma = \pi d^2$ , with  $d$  molecular diameter. Curves obtained have been thus interpolated using third order polynomial and then implemented in Fluent. Finally we have calculated for all species the binary molecular diffusion coefficients from 300 K to 6000K using the model presented in I.3.2.1 (equations I.16 – I.18). These values have been also interpolated by means of third order polynomial and implemented in Fluent as well.

### II.3.2 Blowing model

In order to model injection of fluid from the wall, we have to account for the characteristic length scales involved in the process. If the characteristic length between two injection points is much smaller than the length scales of the turbulent channel flow, the details of injection at this scale are not important and the injection can be modelled by a continuous model. Furthermore, the model must account for the viscous drag, together with the mass, momentum and enthalpy generation from the fluid injected. In our study, we have modelled directly the physical phenomenon, instead of using additional terms in the wall functions.

The blowing model adopted, the so-called 'sources model', consists in applying mass, momentum and energy sources at the first cell above an impermeable adiabatic wall

We have implemented the sources terms writing in C language an UDF (User Defined Function). A user-defined function, or UDF, is a function that we program and that can be dynamically loaded with the solver to change or enhance the standard features of the code. Our UDF operates on the source term of conservation equations; that is, writing these equations in a generalized form we have:

$$\text{div}[\rho V \phi - \Gamma_{\phi} \text{grad} \phi] = S_{\phi} \quad (\text{II.8})$$

where the first and second left-hand side term represent convection and diffusion, respectively, and the right-hand side term is a source term. In the equation  $\phi$  stands for the conserved property and  $\Gamma_{\phi}$  the appropriate diffusivity coefficient. To create an appropriate model of blowing, we have defined, among with a mass source (for every cell over the grain surface), also a momentum source, a species source and an energy source. In fact, defining only a mass source, that mass would enter the domain with no momentum or thermal energy. The mass will therefore have to be accelerated and heated at the expense of the main airstream into which is injected, and consequently there might be a drop in velocity and/or temperature. This drop may or may not be significant, depending on the size of the source; in both cases it could modify significantly the solution. Finally, the energy conservation being written in terms of total energy, the energy source term must account also for the kinetic energy of the gas leaving the surface.

The source term adopted for the variables are:

**Mass source** 
$$S_{mass} = \rho_g v_g \frac{A}{V}$$

**Y – Momentum source** 
$$S_{momentum} = \rho_g v_g^2 \frac{A}{V}$$

**Species (LiH) source**  $S_{LiH} = \rho_g v_g \frac{A}{V}$

**Energy source :**  $S_{energy} = \rho_g v_g h_{950} \frac{A}{V} + \rho_g \frac{v_g^2}{2}$

where A and V are, respectively, the area of the cell surface adjacent to the solid grain and the cell volume.

These sources are directly connected with equation II.1 and II.3. Using the equation II.1 we define the gas mass flow rate as a function of the heat flux arriving on the surface. Analogously, using equation II.3, we can calculate the local regression rate as a function of the surface heat flux. The key point is thus how to calculate the heat fluxes on the basis of velocity, density, pressure and temperature field calculated by the solver in the gas above the surface.

To accomplish this task, we have implemented in the UDFs the same model (based on the standard wall function) used by the solver to calculate the total surface heat flux and summarized in the following.

The wall functions in the code are based on the proposal of Launder and Spalding:<sup>82</sup> the law-of-the-wall for the mean velocity yields

$$U^* = \frac{1}{k} \ln(Ey^*) \quad (II.9)$$

where

$$U^* \equiv \frac{U_P C_\mu^{1/4} k_P^{1/2}}{\tau_w / \rho} \quad (II.10)$$

$$y^* \equiv \frac{\rho C_\mu^{1/4} k_P^{1/2} y_P}{\mu} \quad (II.11)$$

with:

$k$	von Kármán constant (= 0.4187)
$E$	empirical constant (= 9.793)
$U_P$	mean velocity of the fluid at point $P$
$k_P$	turbulence kinetic energy at point $P$
$y_P$	distance from point $P$ to the wall
$\mu$	dynamic viscosity of the fluid
$C_\mu$	k-ε model constant (= )

The logarithmic law for mean velocity is known to be valid for  $30 < y^* < 300$ . In the code, the log-law is employed when  $y^* > 11.225$ . When the mesh is such that  $y^* < 11.225$  at the wall-adjacent cells, Fluent applies the linear (laminar) stress-strain relationship that can be written as

$$U^* = y^* \quad (\text{II.12})$$

We write a similar logarithmic law for mean temperature by using the Reynolds analogy between momentum and energy transport; as in the law-of-the-wall for the mean velocity, the wall functions for temperature employed by Fluent comprises the following two different laws:

- linear law for the thermal conduction sublayer, where molecular conduction is important
- logarithmic law for the turbulent region where the effect of turbulence dominate.

In highly compressible flows, the temperature distribution in the near-wall region can be significantly different from that of subsonic flows, due to the heating by viscous dissipation. In Fluent, the temperature wall functions include the contribution also from the viscous heating and have the following composite form:

$$T^* \equiv \frac{(T_w - T_p) \rho c_p C_\mu^{1/4} k_p^{1/2}}{\dot{q}} \quad (\text{II.13})$$

$$T^* = \text{Pr} y^* + \frac{1}{2} \rho \text{Pr} \frac{C_\mu^{1/4} k_p^{1/2}}{\dot{q}} U_p^2 \quad (y^* < y_T^*) \quad (\text{II.14})$$

$$T^* = \text{Pr}_t \left[ \frac{1}{k} \ln(E y^*) + P \right] + \frac{1}{2} \rho \frac{C_\mu^{1/4} k_p^{1/2}}{\dot{q}} \{ \text{Pr}_t U_p^2 + (\text{Pr} - \text{Pr}_t) U_c^2 \} \quad (y^* > y_T^*) \quad (\text{II.15})$$

where  $P$  is computed by using the formula given by Jayatilleke:<sup>82</sup>

$$P = 9.24 \left[ \left( \frac{\text{Pr}}{\text{Pr}_t} \right)^{3/4} - 1 \right] \left[ 1 + 0.28 e^{-0.007 \text{Pr} / \text{Pr}_t} \right] \quad (\text{II.16})$$

and

$\text{Pr}_t$	turbulent Prandtl number (0.85 at the wall)
$\text{Pr}$	Molecular Prandtl number ( $\mu c_p / k_f$ )
$c_p$	specific heat of fluid

$U_c$	mean velocity magnitude at $y^* = y_T^*$
$k_P$	turbulent kinetic energy at point $P$
$y_P$	distance from point $P$ to the wall
$\mu$	dynamic viscosity of the fluid
$C_\mu$	k- $\epsilon$ model constant (= )
$T_P$	temperature at the cell adjacent to wall
$T_w$	temperature at the wall
$\rho$	density of fluid

The non-dimensional thermal sublayer thickness,  $y_T^*$ , in equations II.14,15 is computed as the  $y^*$  value at which the linear law and the logarithmic law intersect, once the molecular Prandtl number of the fluid being modelled is known or assumed.

The procedure used by Fluent to apply the law-of-the-wall for temperature is as follows. Once the physical properties of the fluid are specified, its molecular Prandtl number is calculated. Then, given the molecular Prandtl number, the thermal sublayer thickness is computed from the intersection of the linear and logarithmic profiles, and stored. During the iteration, depending on the  $y^*$  value at the near-wall cell, either the linear or the logarithmic profile in Equation II.14 or II.15 is applied to compute the heat flux (depending on the type of the boundary conditions on the wall).

### II.3.3 Test Case

To simulate the LiH fuelled SFSCRJ and to compare our results, we have investigated geometrical configurations and “flight” conditions similar to those presented in [1] in particular we have selected as inlet conditions the following::

Inlet Mach	Static Temperature [K]	Static Pressure [atm]	Total Pressure [atm]	Flow velocity [m/s]
2	1550	1	7.8	1490

**Table 6: Inlet conditions**

These conditions have been applied to each geometrical configuration presented in this section.

## III. Results

Figures 14 and 15 show the schematic geometry and the reference system used (here reported for the cylindrical and for the Dump1 configuration).

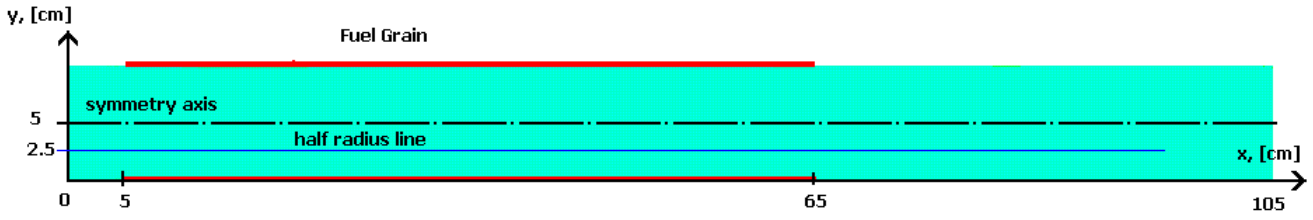


Fig. 14: Cylindrical configuration: reference system

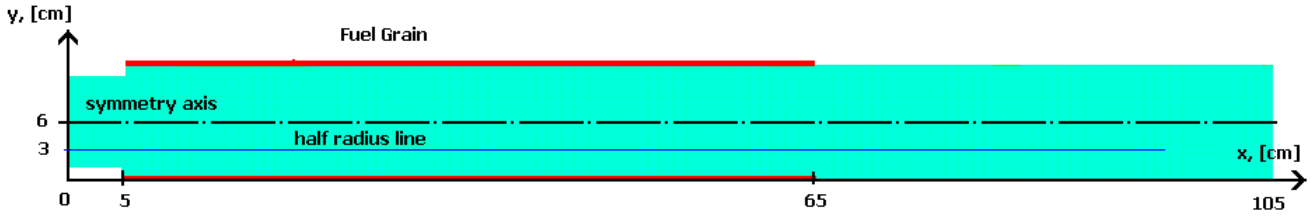


Fig. 15: Dump1 configuration: reference system

The fuel grain (red line) spans 60 cm, from  $x = 5$  to  $x = 65$  cm; the dump ratio  $D_r$ , is defined as:

$$D_r = \frac{R_c}{R_i}$$

where  $R_c$  is the combustor internal radius and  $R_i$  is the inlet internal radius.

Furthermore we have defined a control line, (half radius line) located at  $R_c/2$ , that we will use to plot pressure and temperature along the combustor.

Finally, for all the configurations, we have performed comparisons between reacting and non reacting cases, assuming the non reacting case to represent the flow condition immediately before the start of the surface decomposition.

### III.1 Cylindrical configuration ( $D_r = 1$ )

Figure 16 shows the static temperature contours of both non reacting and reacting case.

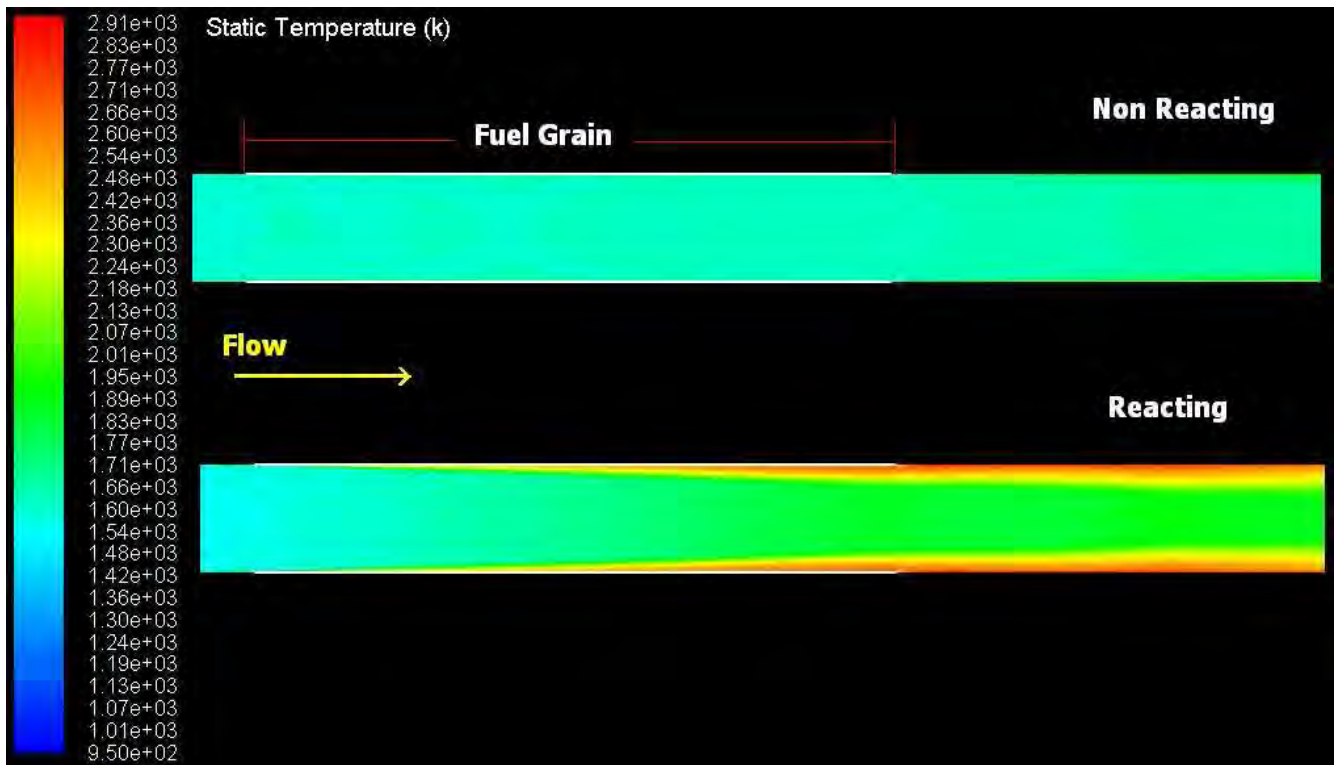


Fig. 16: Contours of static temperature (reacting and non reacting case)

As we can see, an intense flame is present over the fuel grain, growing along the combustor and up to its end. As an effect of the gas phase combustion, the heat flux (figure 17) is much higher (up to three times) than that due only to the hot airstream entering the combustor in the non reacting case.

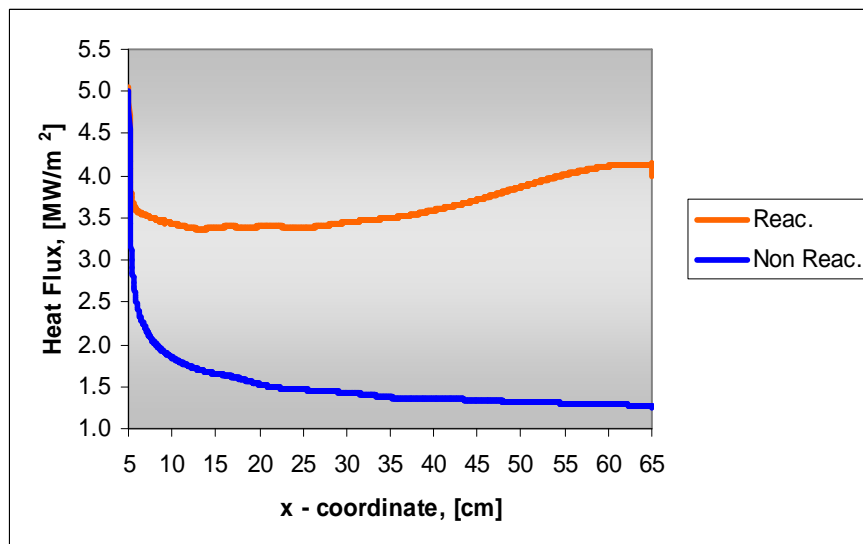


Fig. 17: Heat flux over the grain surface

As a consequence of this significant heat flux, the grain surface decomposes and regresses with a regression rate of the same order of that calculated by Jarymowycz and Kuo;<sup>21</sup> figures 18 - 20 show respectively the regression rate, the LiH mass flow rate produced and the associated blowing velocity.

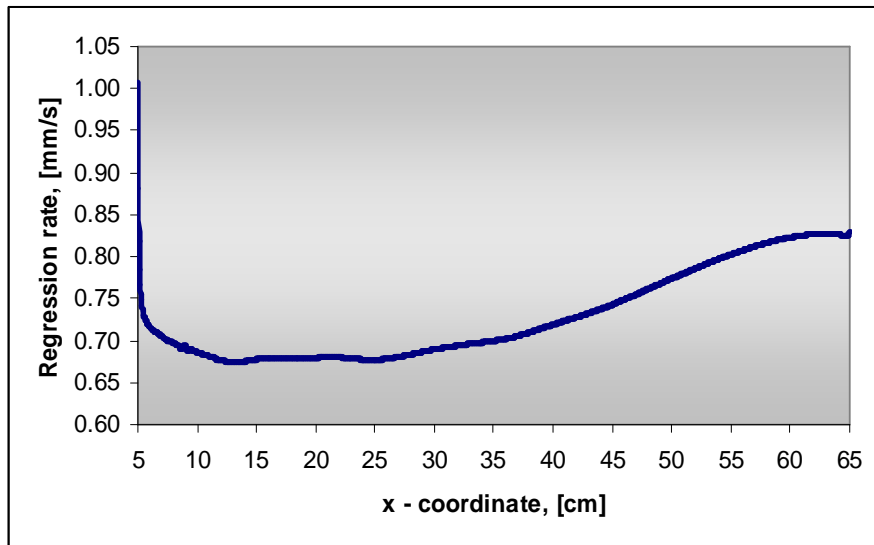


Fig. 18: Grain regression rate

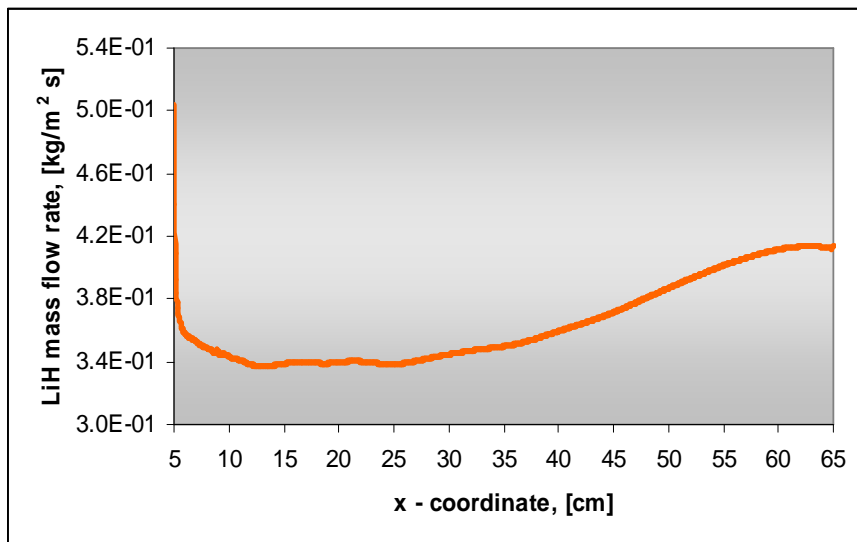
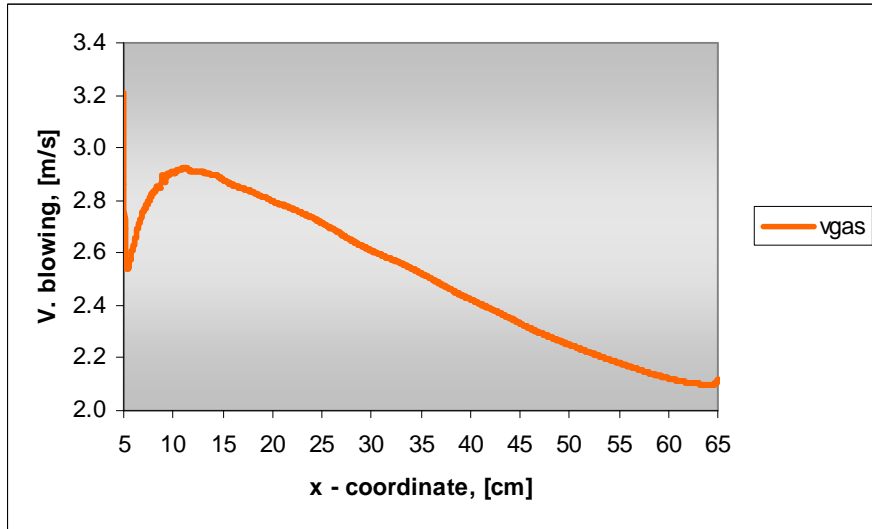


Fig. 19: LiH local mass flow rate



**Fig. 20: Blowing velocity**

The total LiH mass flow rate injected into the chamber is 0.065 kg/s while the mass flow rate of the air entering the combustor is 2.77 kg/s; thus the scramjet is working at an air to fuel mass ratio (O/F) of 42.2

The maximum temperature reached along the combustor is 2950 K, located downstream of the entrance and toward the end of the grain (figure 21).

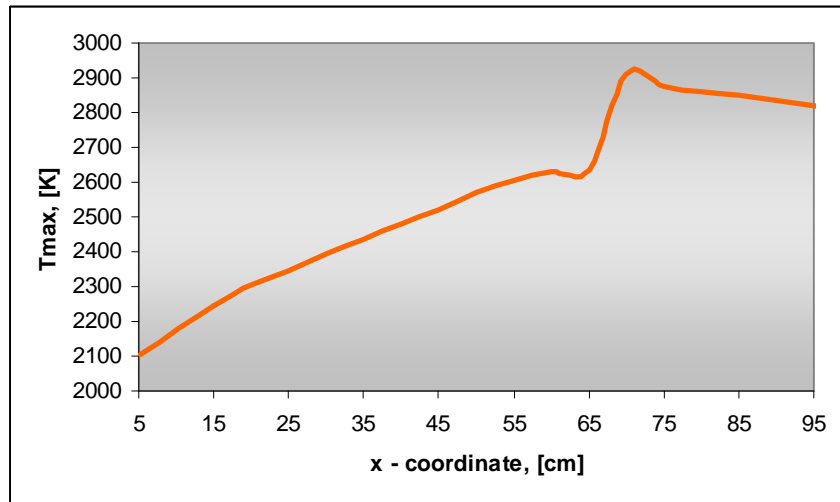


**Fig. 21: Maximum temperature along the chamber**

The net temperature increase for  $x > 65$  (the final part of the grain) is connected to the end of the cooling effect of the gas (which is at a temperature of 950 K) injected in the reacting boundary layer from the decomposing and regressing surface. Furthermore, as a consequence of the ceased mass injection, the thickness of the reacting zone decreases slowly (figure 16), allowing an expansion of the core flow. This effect is also visible in figures 22, 23 where we have reported the temperature calculated along the chamber axis and along the half radius line, compared with the non reacting case (that is: when the blowing is not present),.

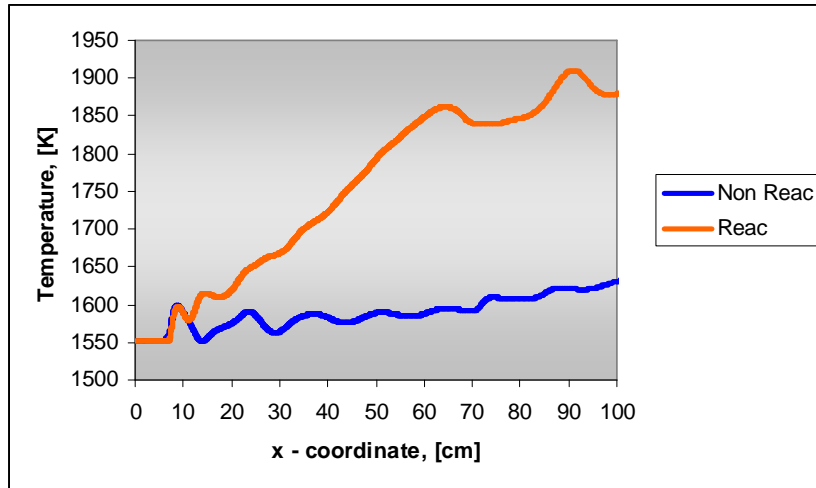


**Fig. 22: Static Temperature along the chamber axis**

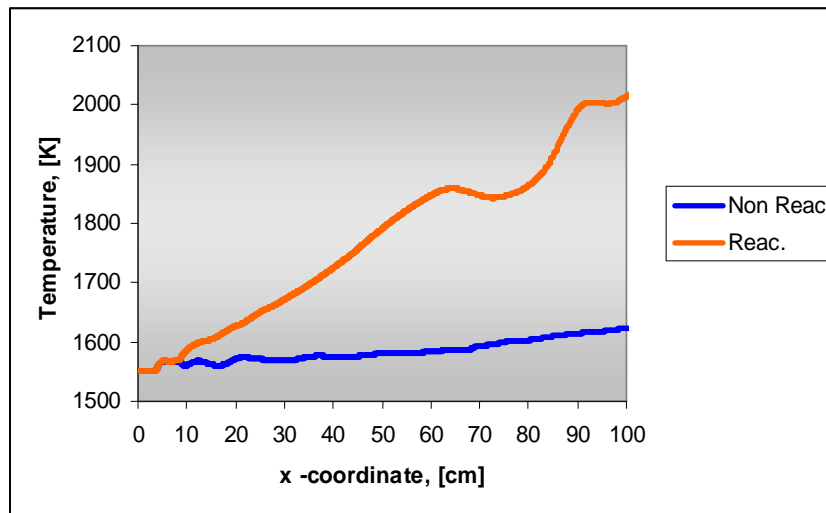


**Fig. 23: Static Temperature along the half radius line**

Downstream of this first expansion, the reacting zone thickness increases due to the increasing combustion temperature, allowing a certain amount of flow recompression; this effect is shown in figures 24, (where the non reacting and the reacting case are compared), and in figures 26, 27 (where the pressure along the axis and the half radius line is plotted).

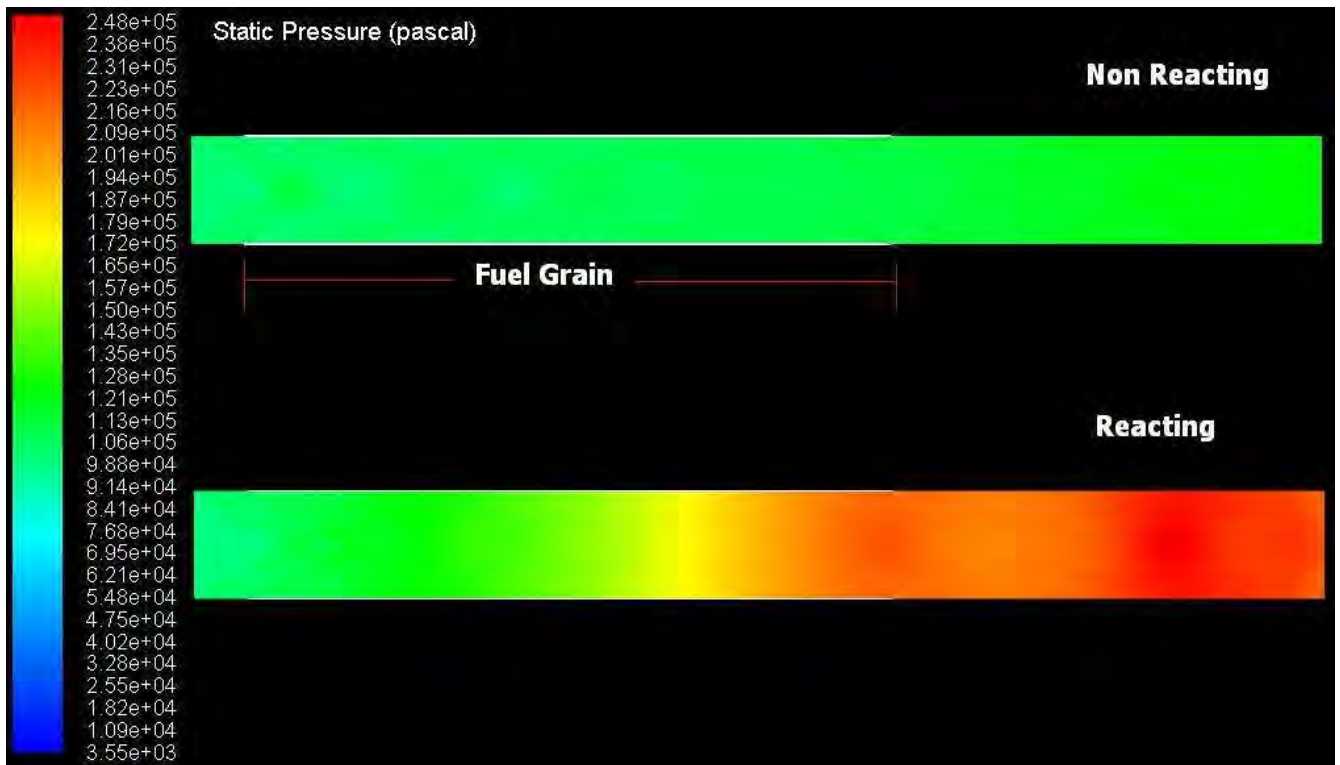


Fig. 24: Contours of static pressure (reacting and non reacting case)

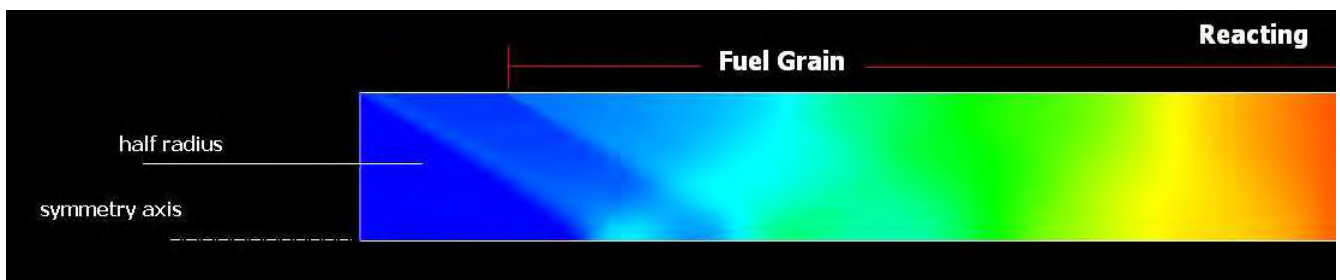


Fig. 25: Contours of static pressure (detail of the combustor half section)

Figures 26 and 27 show also the effect of the complex oblique shock system on initial part of the grain (figures 25). As we can see an oblique shock is located exactly at the grain inlet; the consequent compression, increases as an effect of the waves reflecting along the chamber, causing the decreasing trend of the blowing velocity.

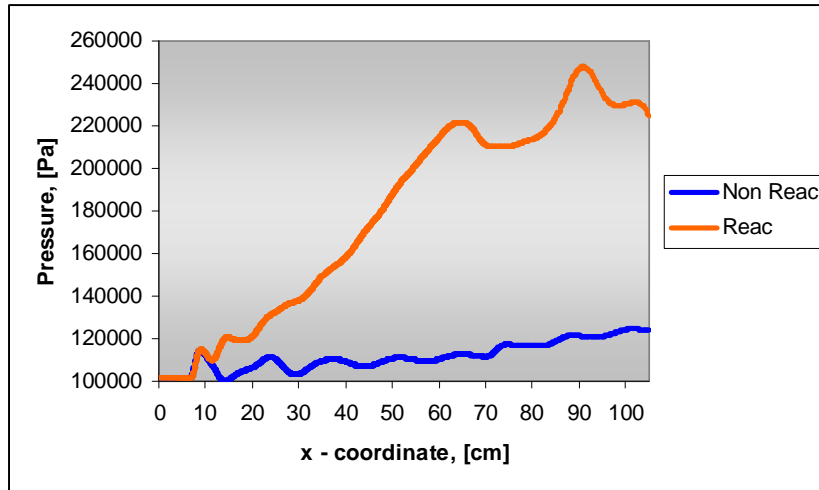


Fig. 26: Static pressure along the chamber axis

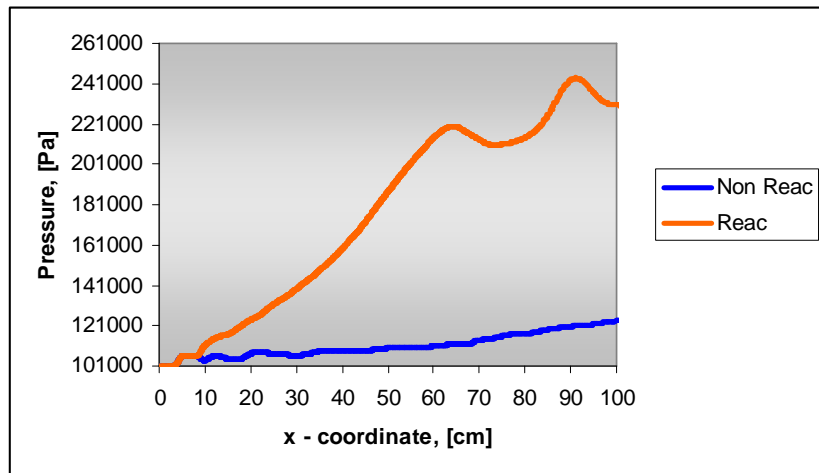
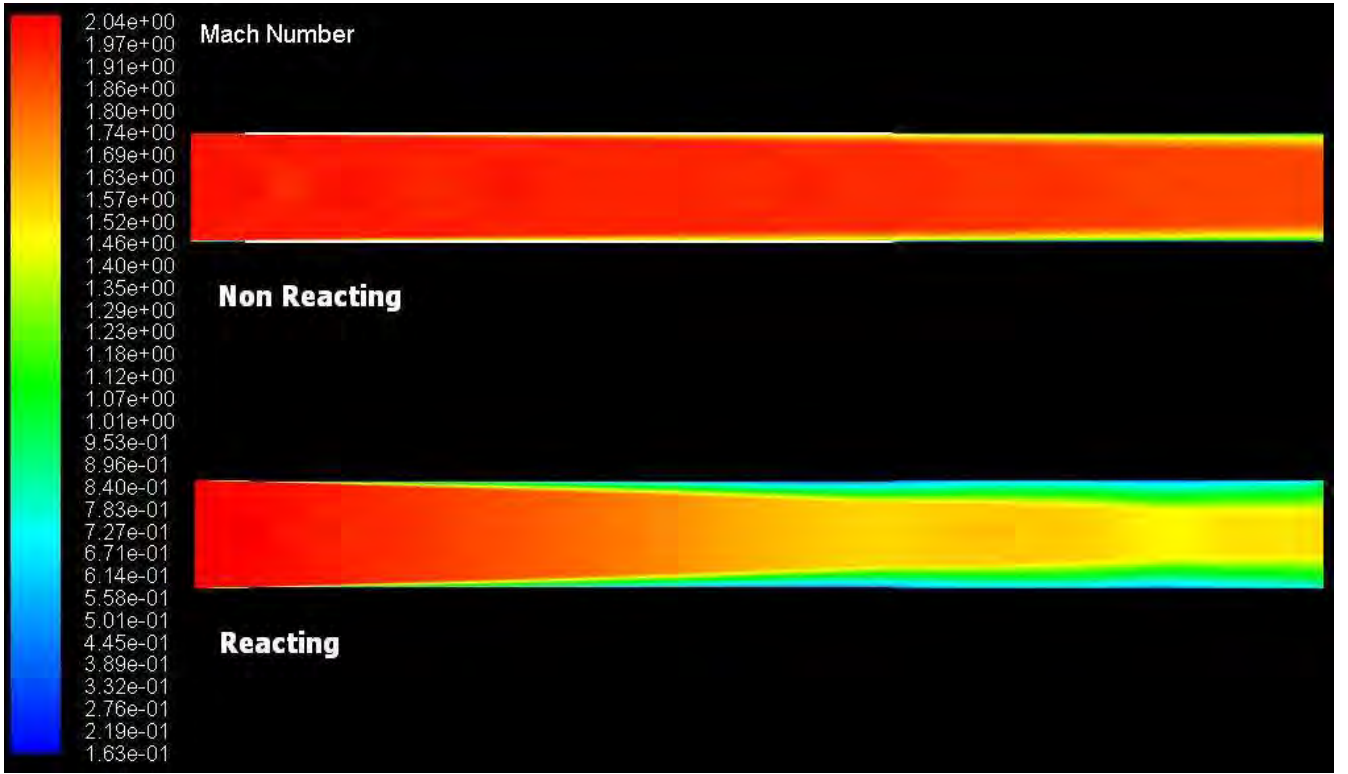


Fig. 27: Static pressure along the half radius line

This feature is also visible in figure 28 where the Mach number contours for the non reacting and reacting cases are compared. Notice that despite the complex wave system the flow at the exit section is largely supersonic.



**Fig. 28: Contour of Mach number (reacting and non reacting case)**

Finally, figure 29 shows the contours of mixing time, calculated as:

$$t = \frac{\eta^2}{D^{th}}$$

where  $D^{th}$  is the turbulent diffusivity and  $\eta$  is the Taylor microscale, calculated as:

$$\eta = \left( \frac{\nu k}{\varepsilon} \right)^{1/2}$$

whit  $\nu$  kinematic viscosity,  $k$  turbulent kinetic energy and  $\varepsilon$  the turbulent dissipation rate.

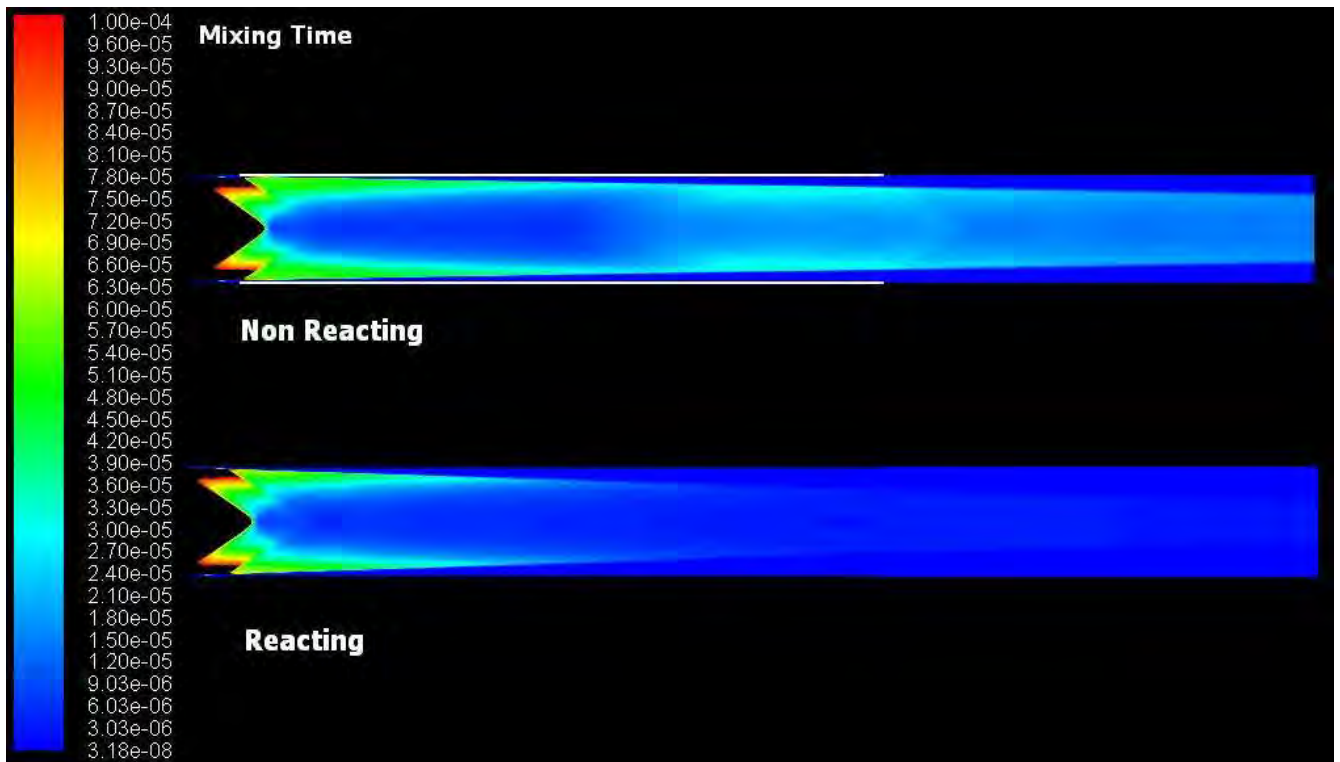
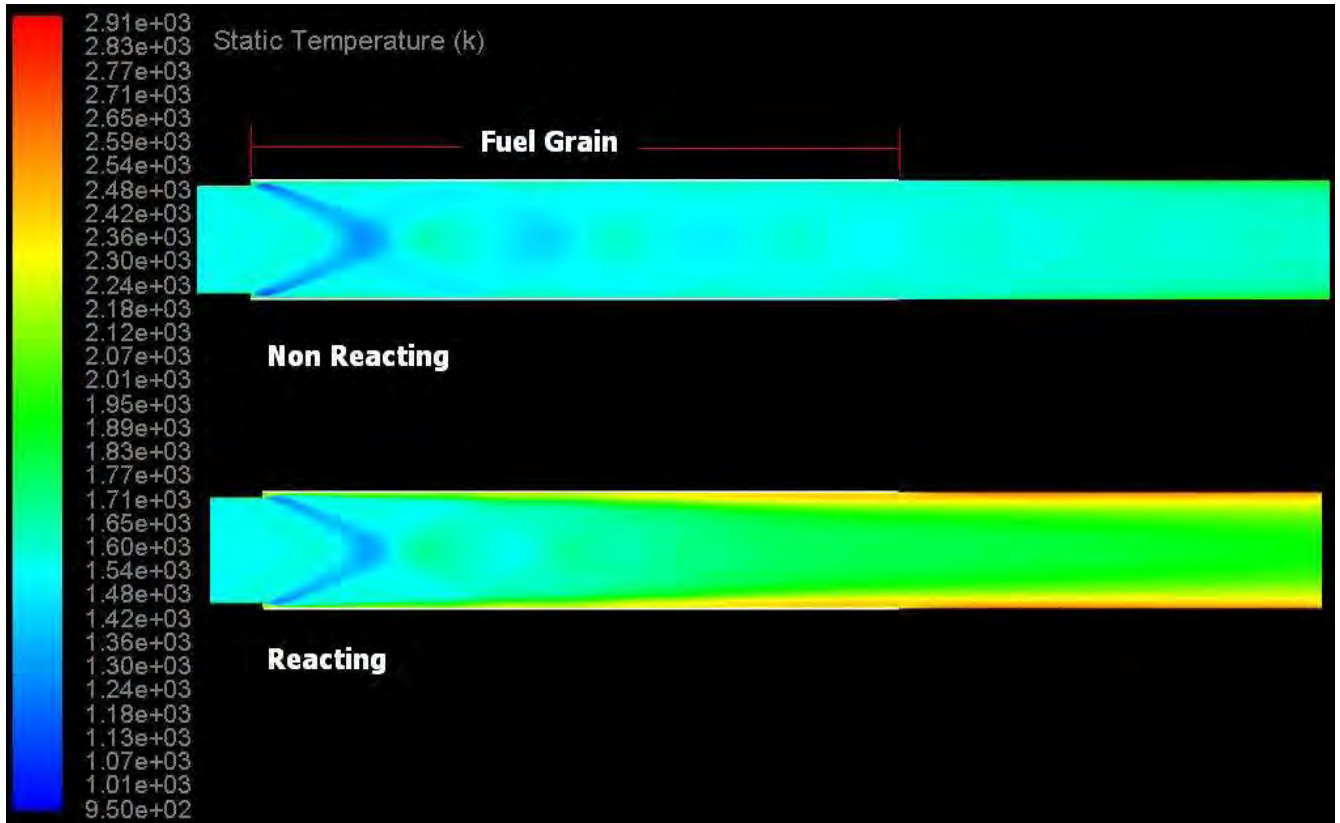


Fig. 29: Contour of mixing time (reacting and non reacting case)

As shown, due to the highly turbulent flow, in the boundary layer, the mixing time is very short (of order of  $10^{-7}$  s); moreover, in presence of combustion, thanks to the growth of the boundary layer and to the consequent complex wave system, the mixing time decreases also in the core flow.

### III.2 Dump combustor (configuration Dump05, $Dr = 1.1$ )

Figure 30 shows the static temperature contours of both non reacting and reacting cases.



**Fig. 30: Contours of static temperature (reacting and non reacting case)**

As we can see, also in this case an intense flame is present over the fuel grain, growing from the recirculation zone near the sudden area increase up to the exit section. As an effect of the gas phase combustion, the heat flux (figure 31) is much higher than that due only to the hot flow entering the combustor (that is, in the non reacting case).

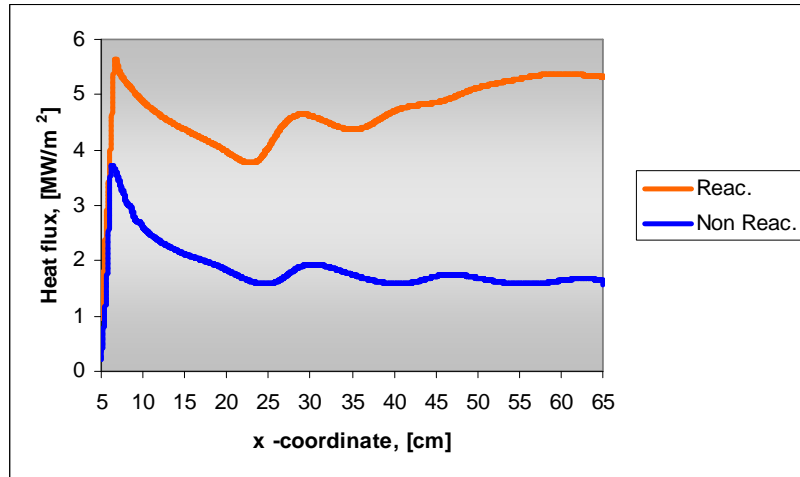


Fig. 31: Heat flux over the grain surface

As a consequence of the heat flux, the grain surface decomposes and regresses with a regression rate of the same order of calculated by Ben-Harosh and Gany;<sup>25</sup> figures 32 - 33 show respectively the regression rate, the LiH mass flow rate produced and the consequent blowing velocity.

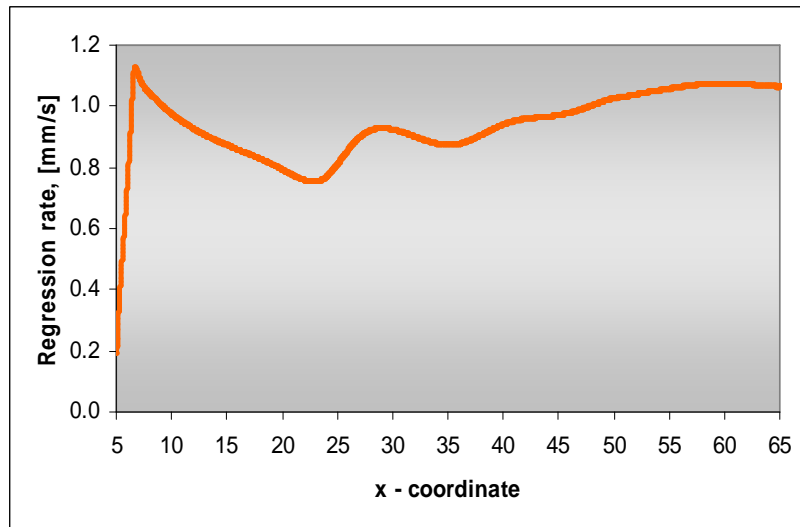


Fig. 32: Local regression rate

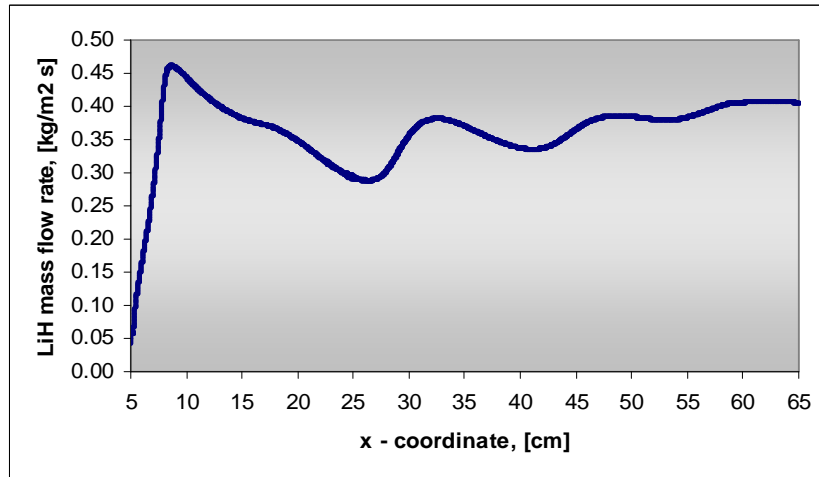


Fig. 33: LiH local mass flow rate

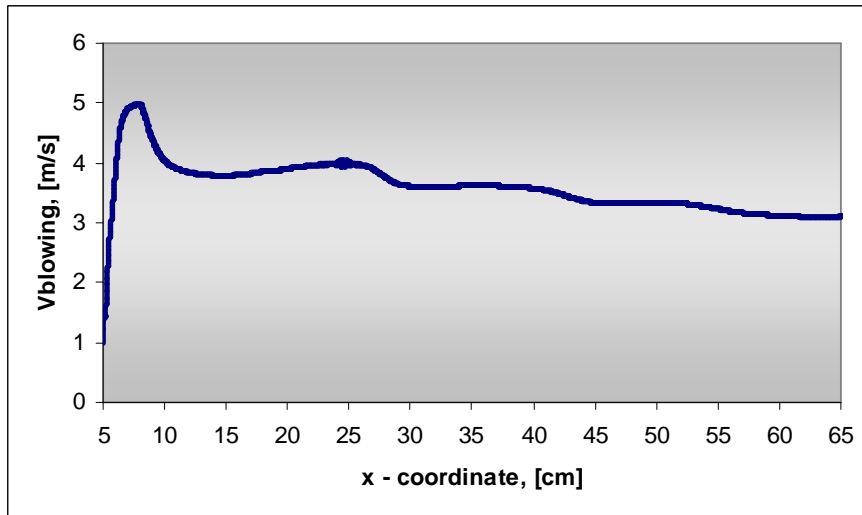
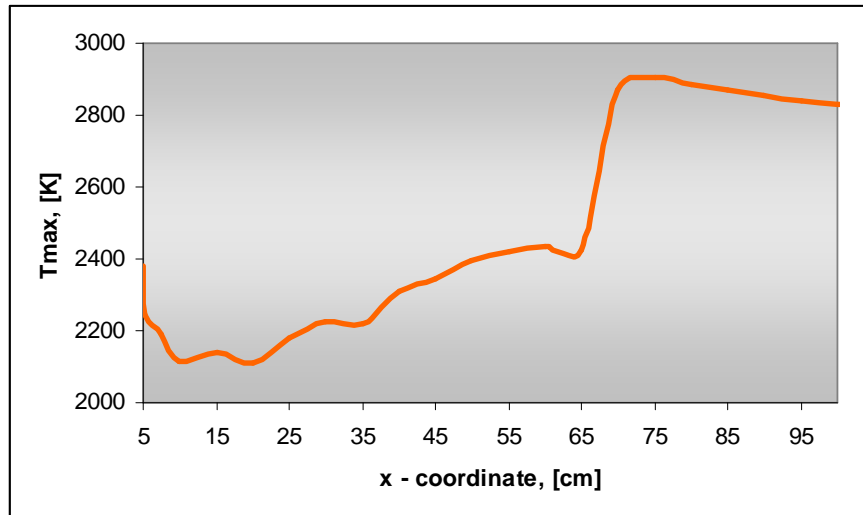


Fig. 34: LiH local mass flow rate

The total LiH mass flow rate injected inside the chamber is 0.075 kg/s while the mass flow rate of the air entering the combustor is 2.77 kg/s; thus the scramjet is working at a air to fuel mass ratio (O/F) of 37.05.

The maximum temperature reached along the combustor is 2906 K, located downstream, near the end of the grain (figure 35).



**Fig. 35: Maximum temperature along the chamber**

Once again, the net temperature increase after  $x = 65$  (the final part of the grain) is connected to the end of the cooling effect of the gas (which as a temperature of 950 K) injected in the reacting boundary layer from the surface. Furthermore, in the first part of the grain, from about  $x = 10$  to  $x = 20$  cm, the cooling effect due to the expansion wave located in the upper corner of the dump is well visible. This effect is clearer examining figures 36, 37 where we have reported the temperature calculated along the chamber axis and along the half radius line, compared with the non reacting case.

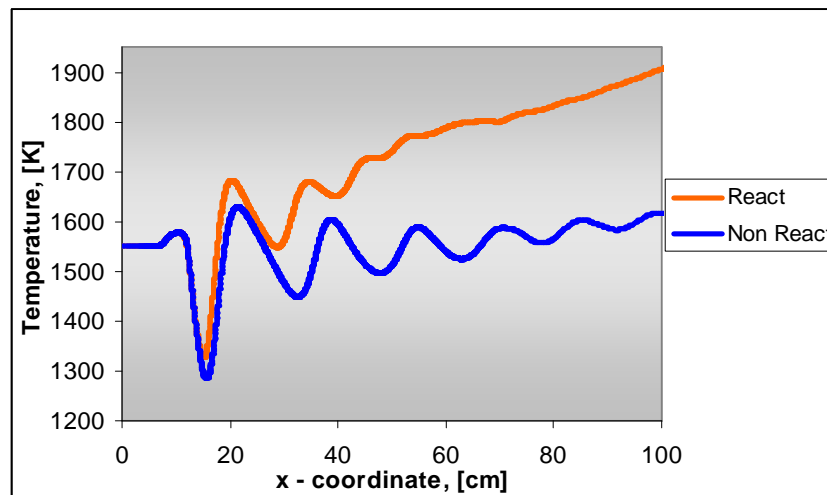


**Fig. 36: Static temperature along the chamber axis**

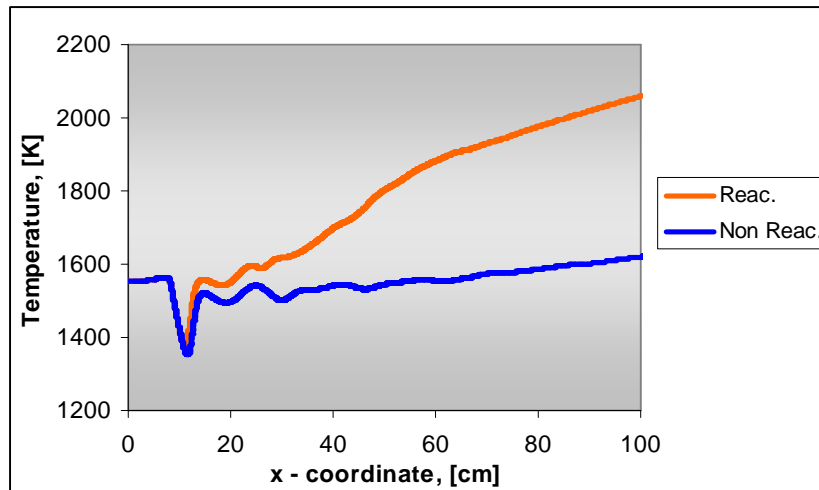


Fig. 37: Static temperature along the half radius line

In fact, as we can see comparing figures 30 and 36 – 38, this expansion wave lowers the core flow temperature up to 1300 K; the following reflecting waves (figure 38) create alternatively compression and expansion regions, affecting greatly the reacting zone. This feature is shown more clearly in figures 39, 40, where a detail of the first part of the grain is stressed.

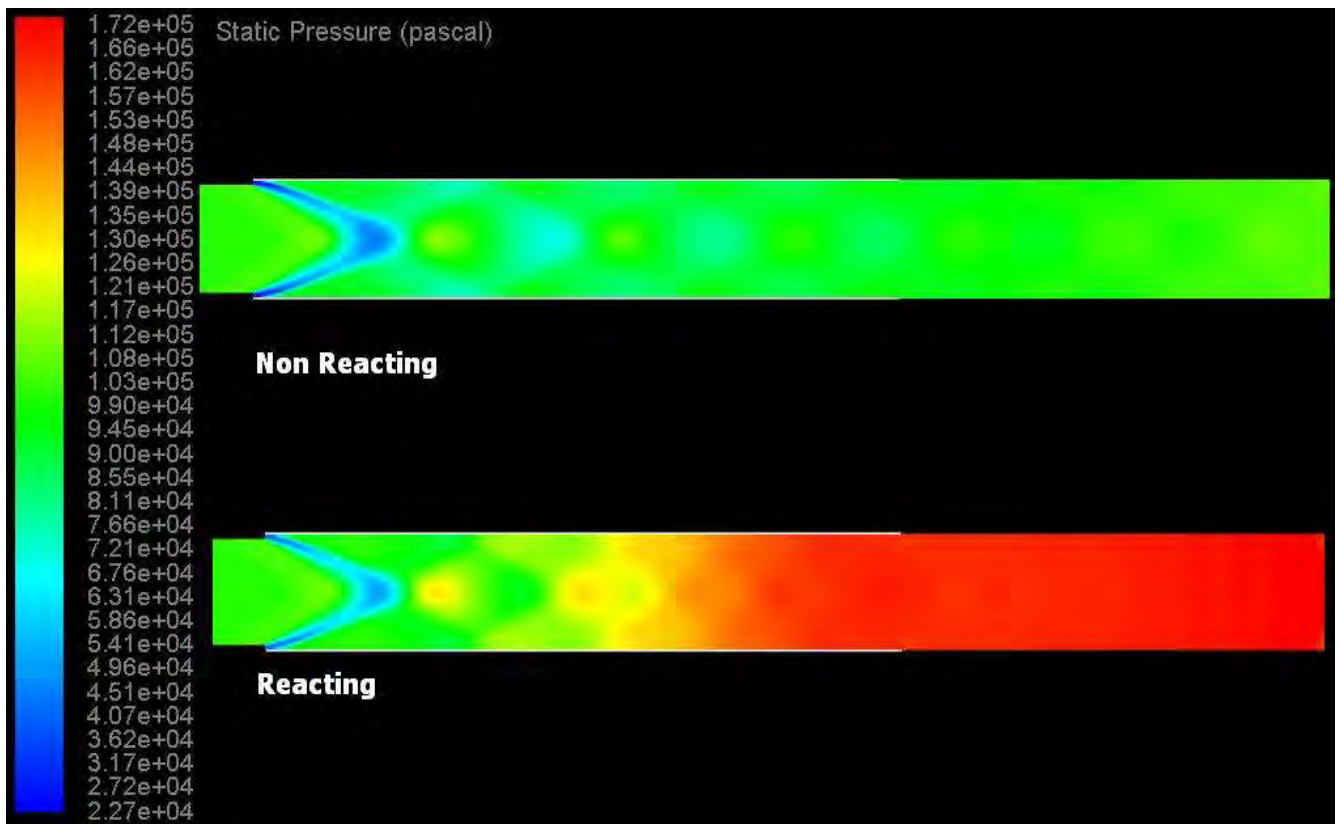


Fig. 38: Contours of static pressure (reacting and non reacting case)

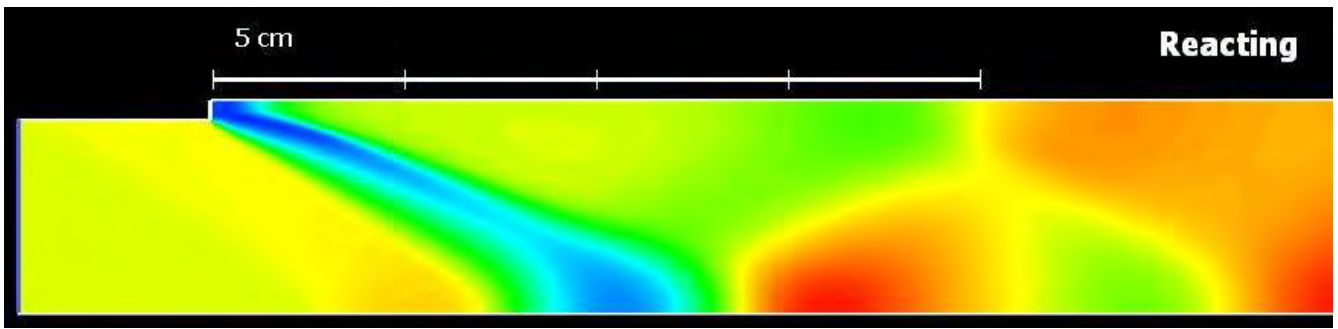


Fig. 39: Contours of static pressure (detail of reacting case)

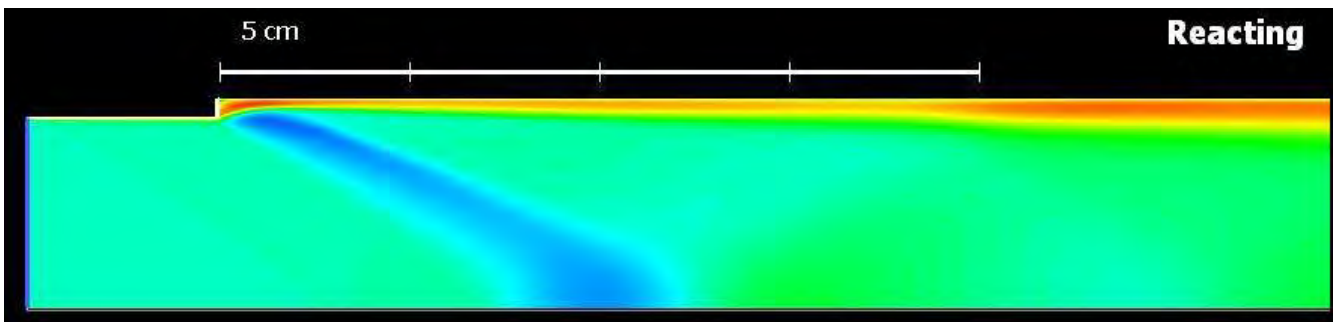


Fig. 40: Contours of static temperature (detail of reacting case)

The pressure behaviour along the axis chamber and the half radius line is shown in figures 41, 42.

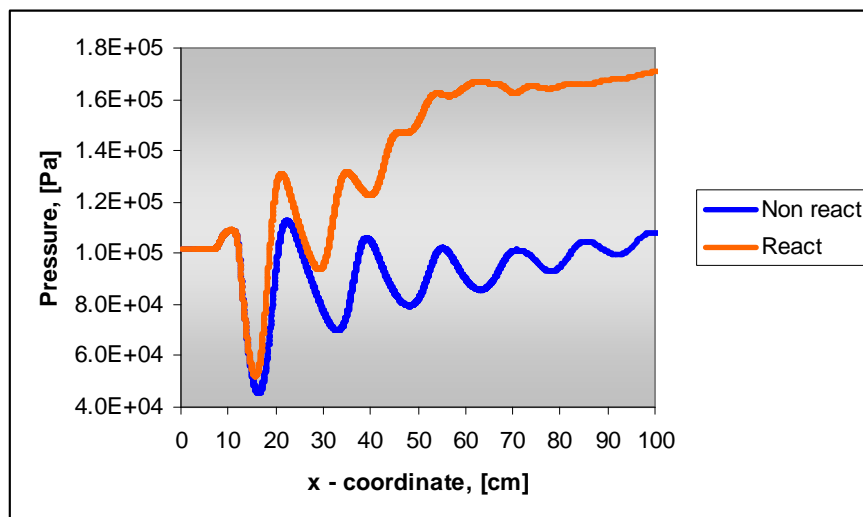
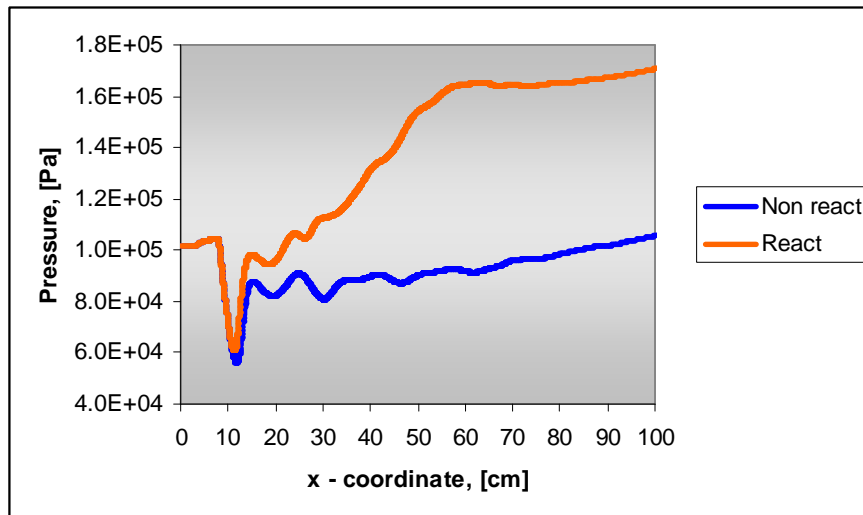
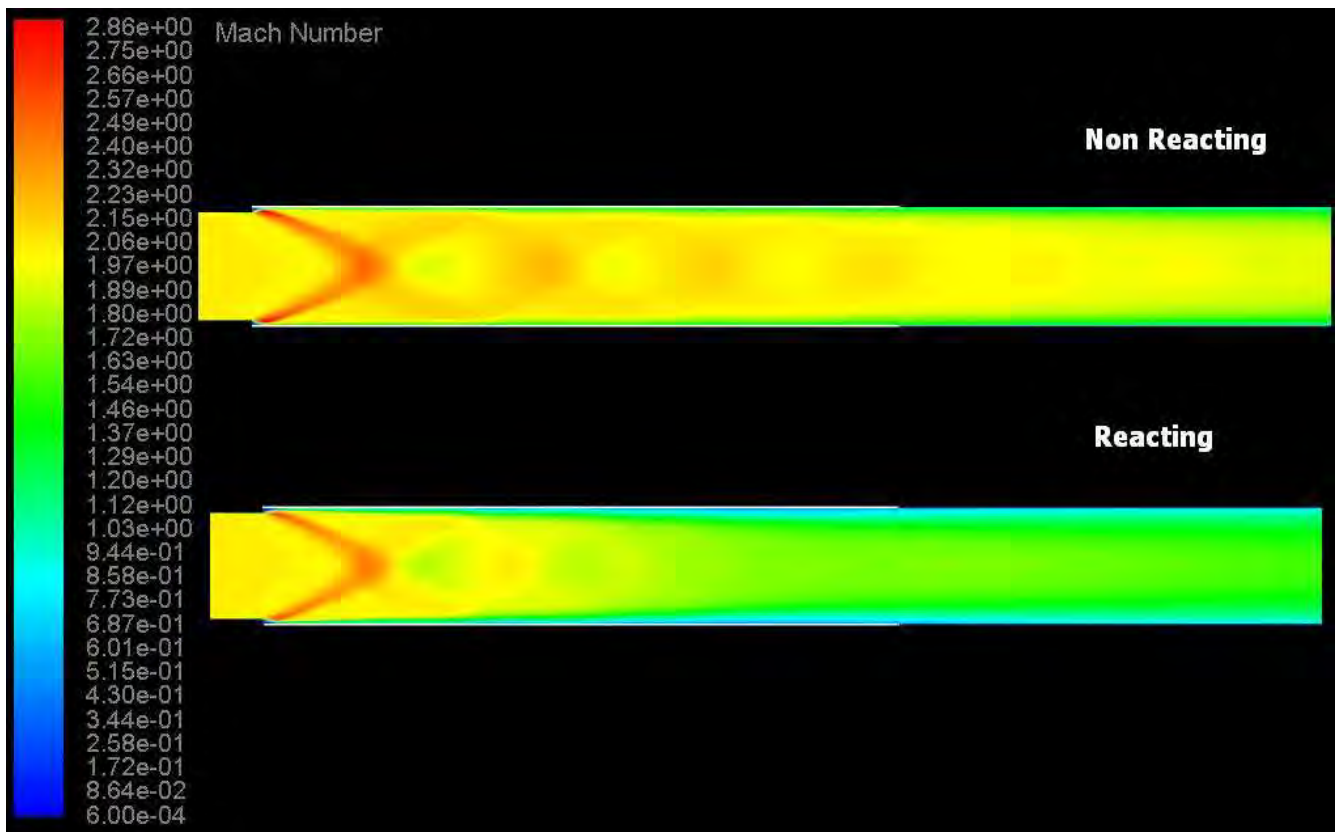


Fig. 41: Static pressure along the chamber axis



**Fig. 42: Static pressure along the half radius line**

Finally, figures 43 and 44 show respectively the Mach number contour and the mixing time contour of both non reacting and reacting cases.



**Fig. 43: Contour of Mach number (reacting and non reacting case)**

Observing figure 43 we can see the effect of the temperature increase; due to the good mixing times in the chamber (figure 44) and to the presence of a recirculation zone at the entrance inside the grain we obtain higher combustion temperatures than in the case of the cylindrical configuration, while maintaining a supersonic flow in the combustor exit section.

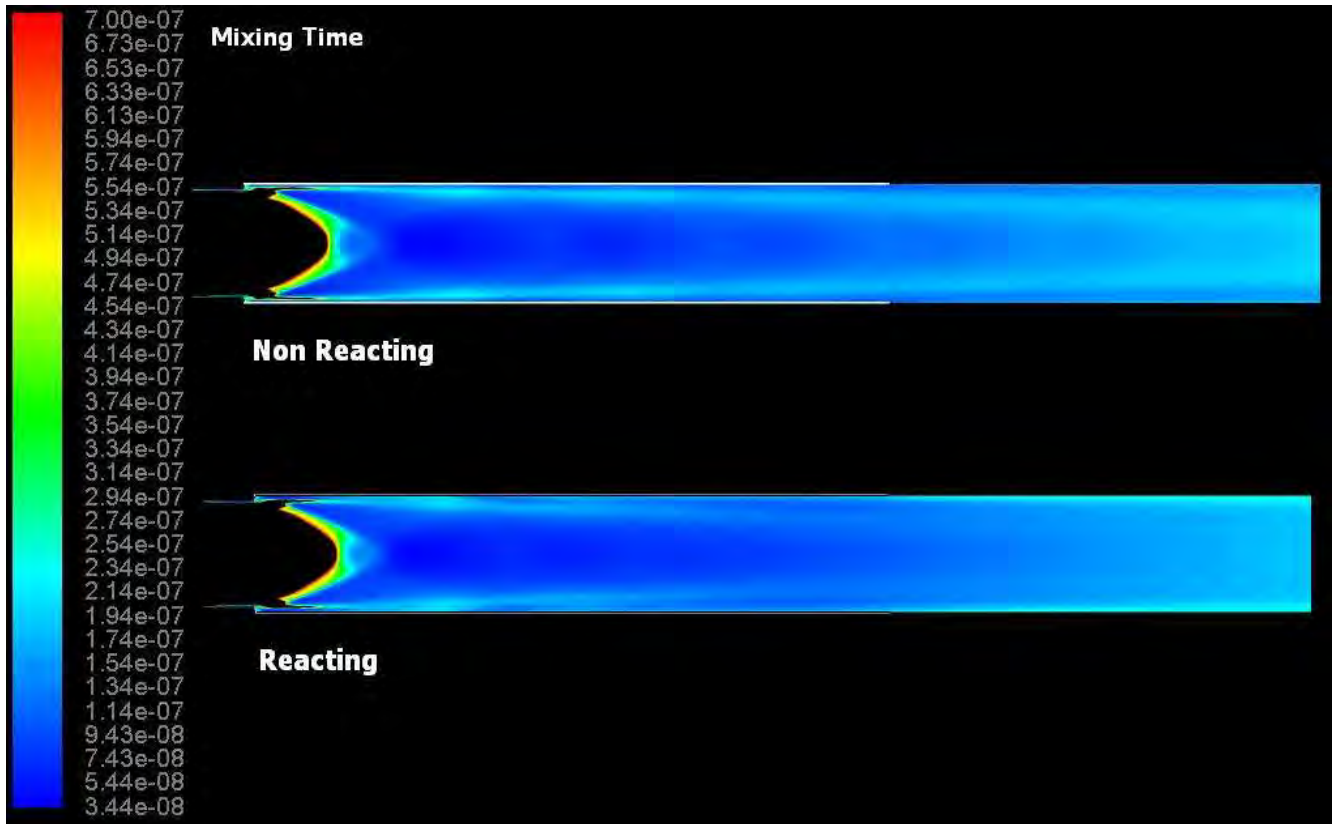
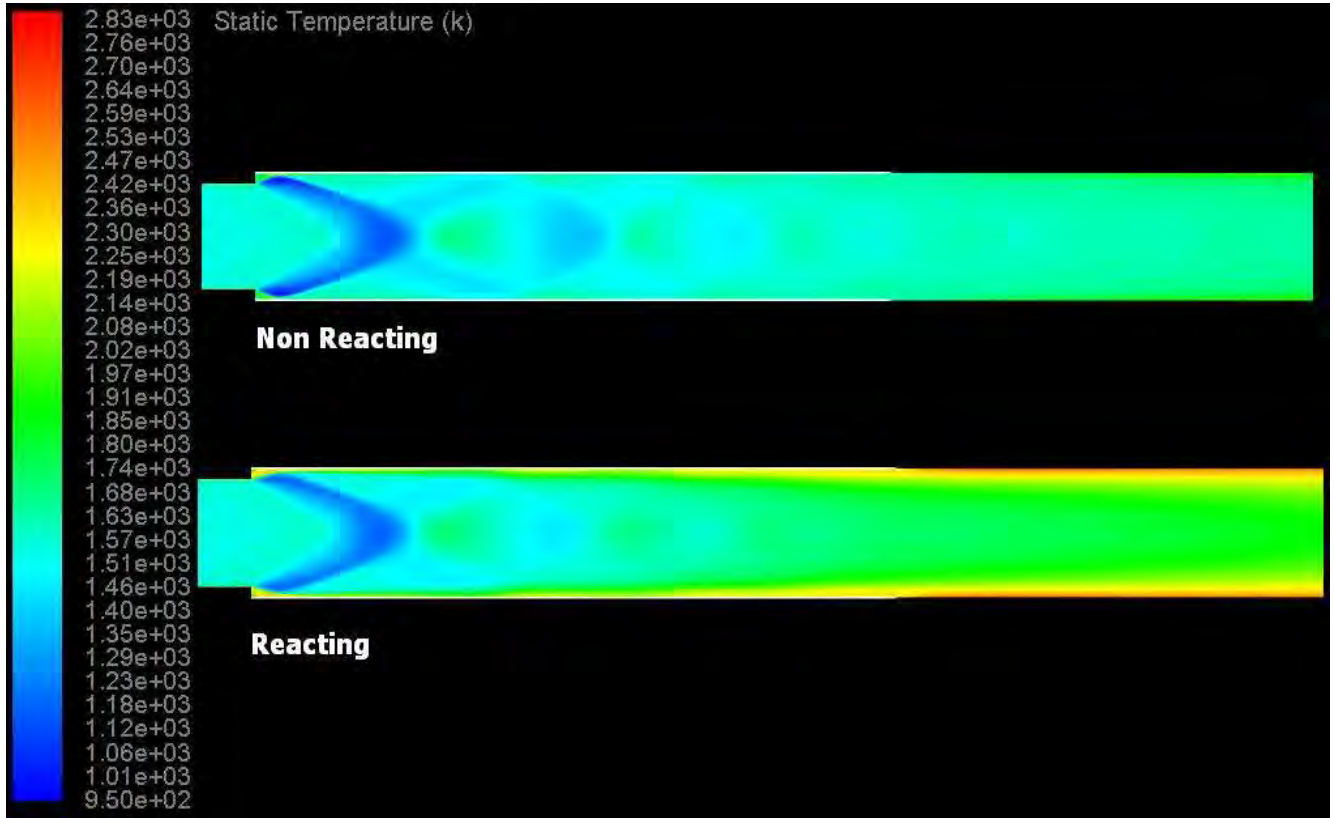


Fig. 44: Contour of mixing time (reacting and non reacting case)

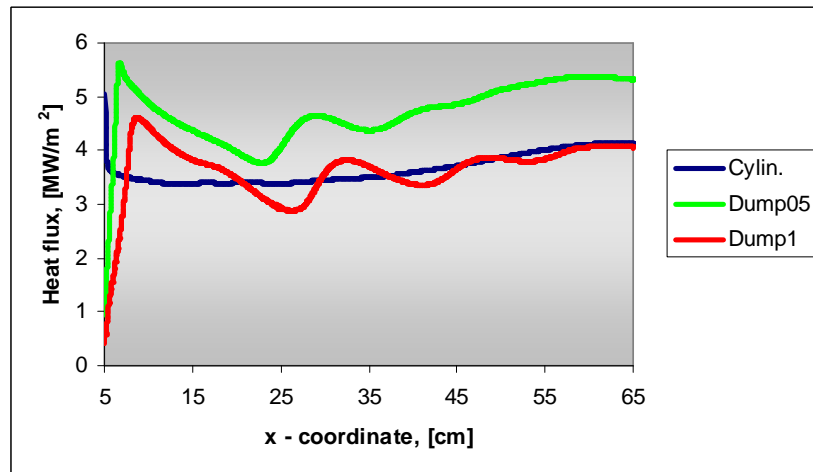
### III.3 Configuration Dump1 ( $Dr = 1.2$ ) and comparisons

Figure 45 shows the static temperature contours of both non reacting and reacting case.



**Fig. 45: Contours of static temperature (reacting and non reacting case)**

As in the case of the first two configuration examined, a flame is present over the fuel grain, growing along the combustor up to its end. However, comparing the heat flux obtained with those of cylindrical and dump05 configurations (figure 46), we can see that it is of the same order of that of the first, but at least  $1 \text{ MW/m}^2$  lower than that of the dump05 combustor.



**Fig. 46: Comparison among the heat fluxes over the grain surface**

As a consequence also the regression rate (fig. 46) and the maximum temperature along the chamber are lower than those of the Dump05 configuration

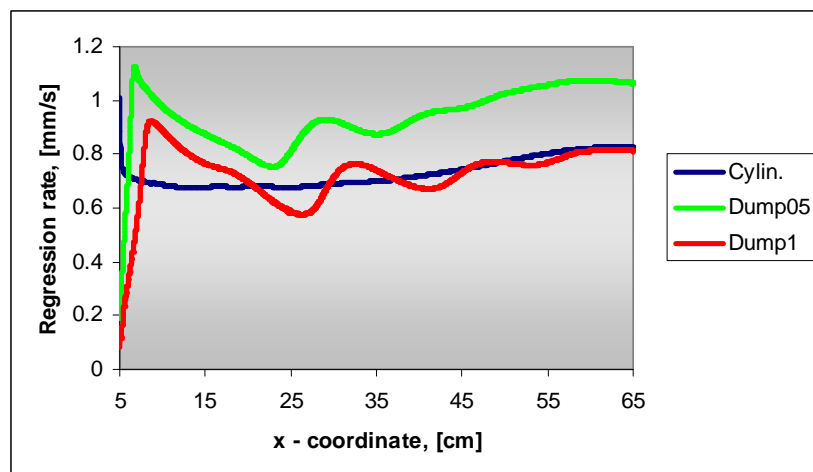


**Fig. 47: Comparison among regression rates**

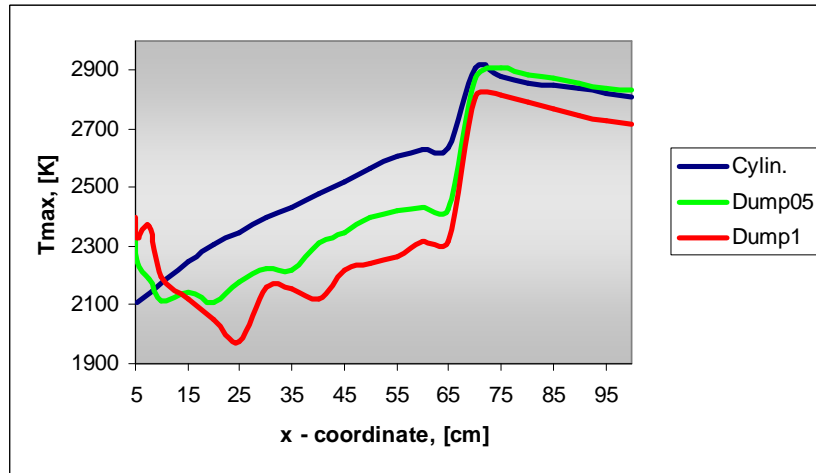


**Fig. 48: Comparison among maximum temperatures along the chambers**

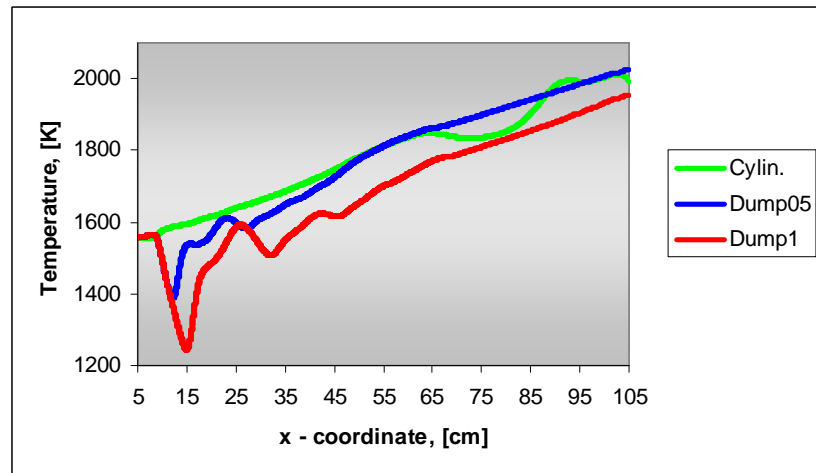


**Fig. 49: Comparison among temperatures along the chambers (half radius line)**

This effect may be explained considering that the higher dump (1 cm) allows more intense expansion and thus lower temperatures (with respect to the Dump05 configuration) of the air entering the chamber; furthermore the Dump1 configuration has a volume higher than that of Dump05. Thus, despite the better mixing obtainable by increasing the dump ratio from  $Dr = 1.1$  to  $Dr = 1.2$  (figures 50, 53) we cannot reach the high temperatures obtained in the others configurations.

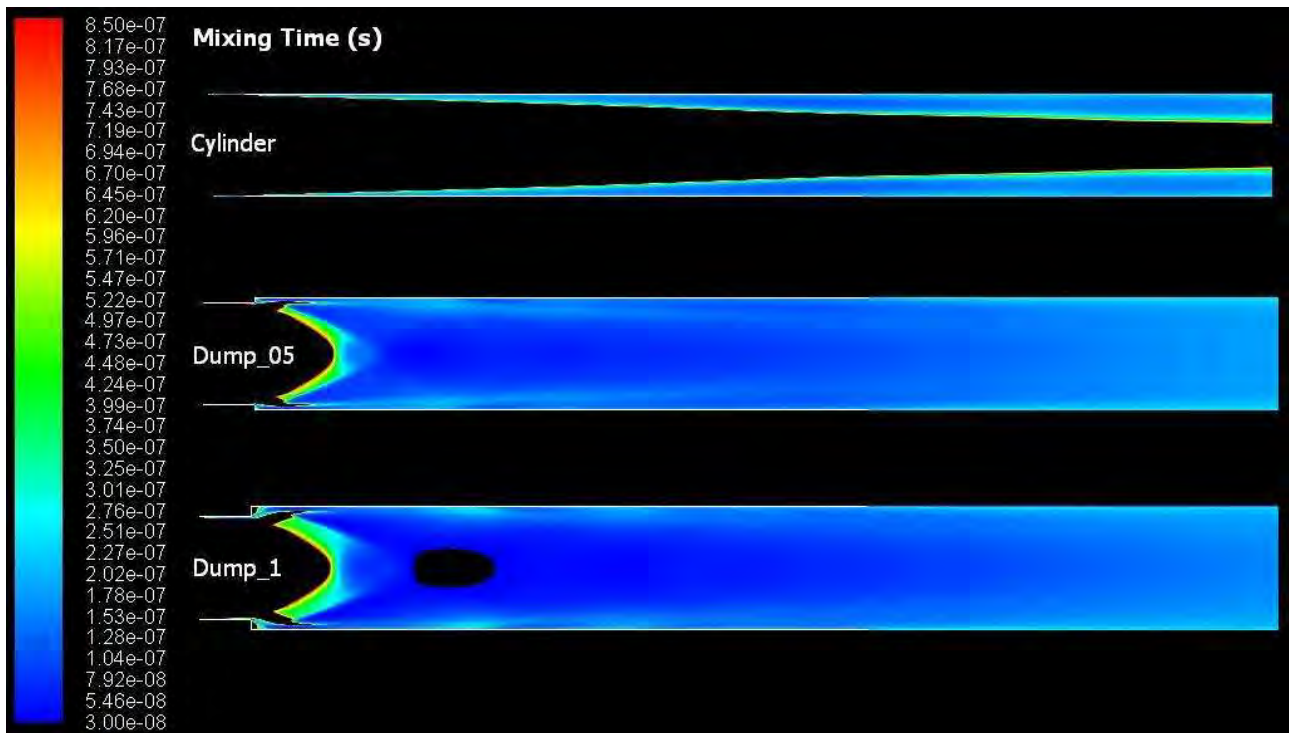
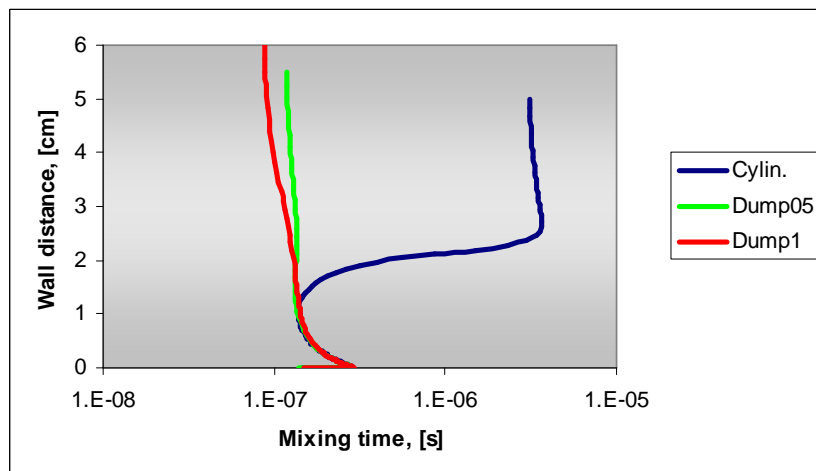


Fig. 50: Comparison among contours of mixing time

Fig. 51: Comparison among mixing times along the radius at  $x = 65$  (end of the grain)

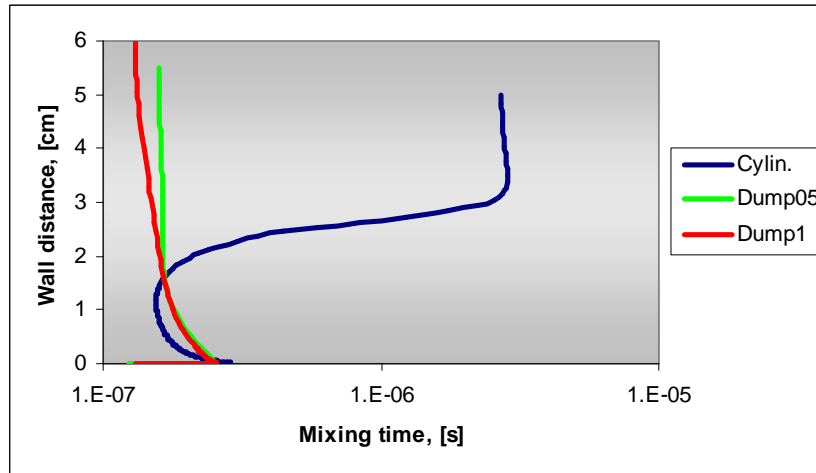


Fig. 52: Comparison among mixing times along the radius at  $x = 85$

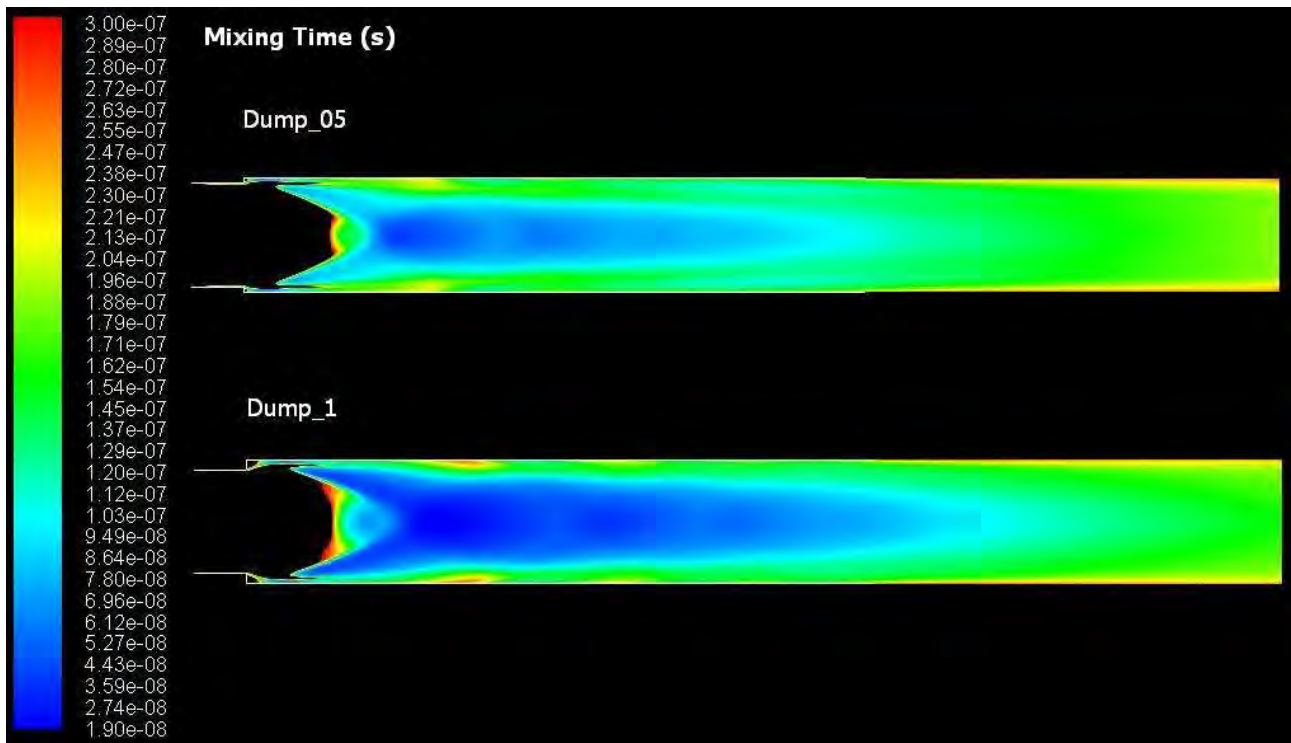


Fig. 53: Comparison among contours of mixing time (Dump05 vs Dump1)

The effect of the increased dump on the combustion in the recirculation region at the begin of the grain is shown in figure 54.

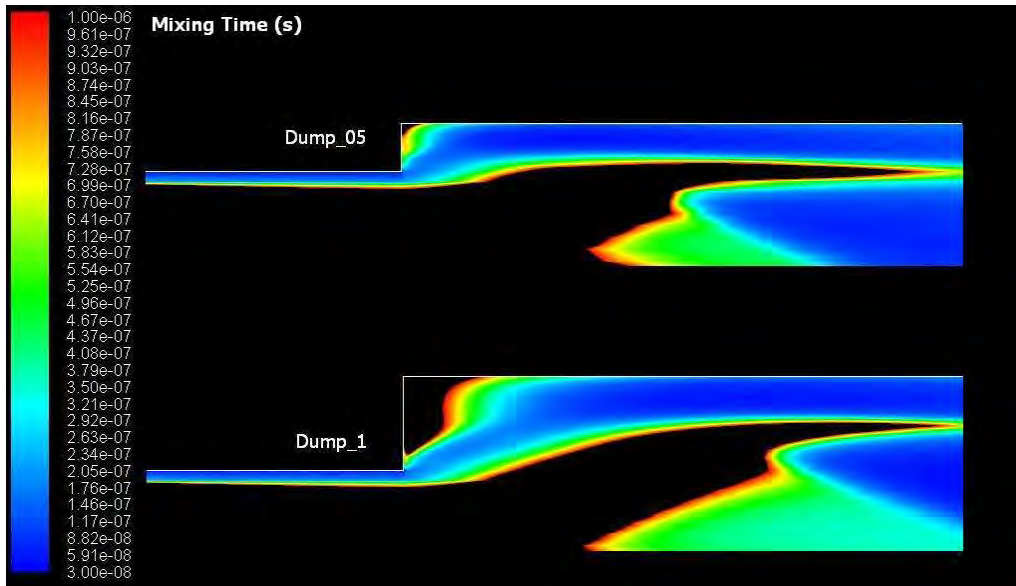


Fig. 54: Comparison among contours of mixing time (Dump05 vs Dump1- Detail)

As we can see a shorter dump allows shorter mixing times in the corner, favouring the flame holding (figures 55 and V56) and an higher mass flow rate of LiH injected in the reacting layer. That so enhances the combustion downstream of the zone of the boundary layer – expansion wave interaction.

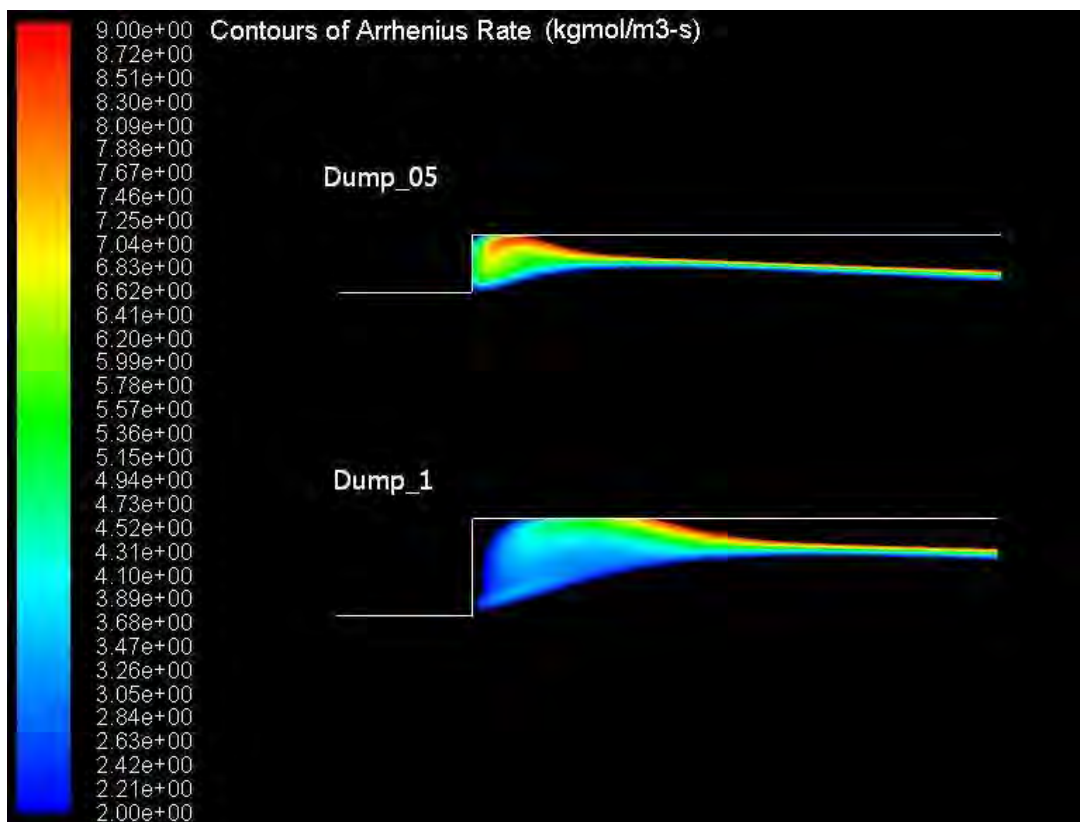


Fig. 55: Comparison among contours of  $H_2/O_2$  reaction rate (Dump05 vs Dump1- Detail)

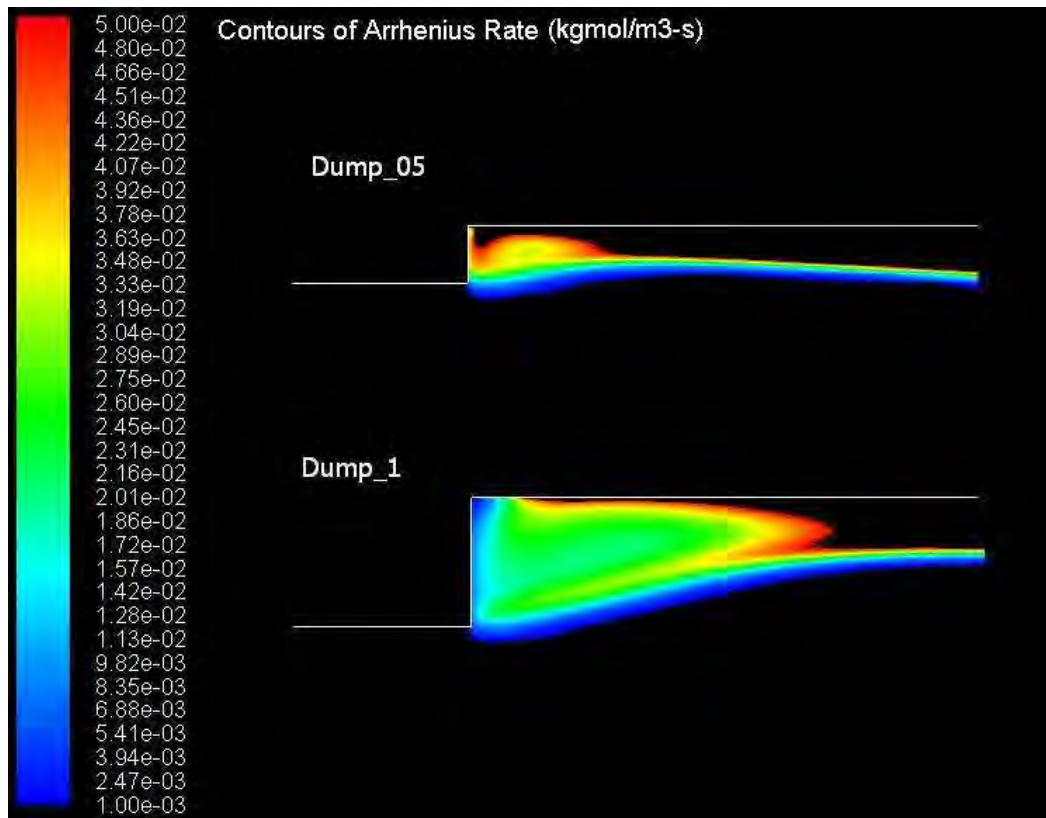


Fig. 56: Comparison among contours of Li/O<sub>2</sub> reaction rate (Dump05 vs Dump1- Detail)

The combined effect of enhanced mixing times and decreased air flow temperature on the rate of reactions is shown in figures 57 and 58.

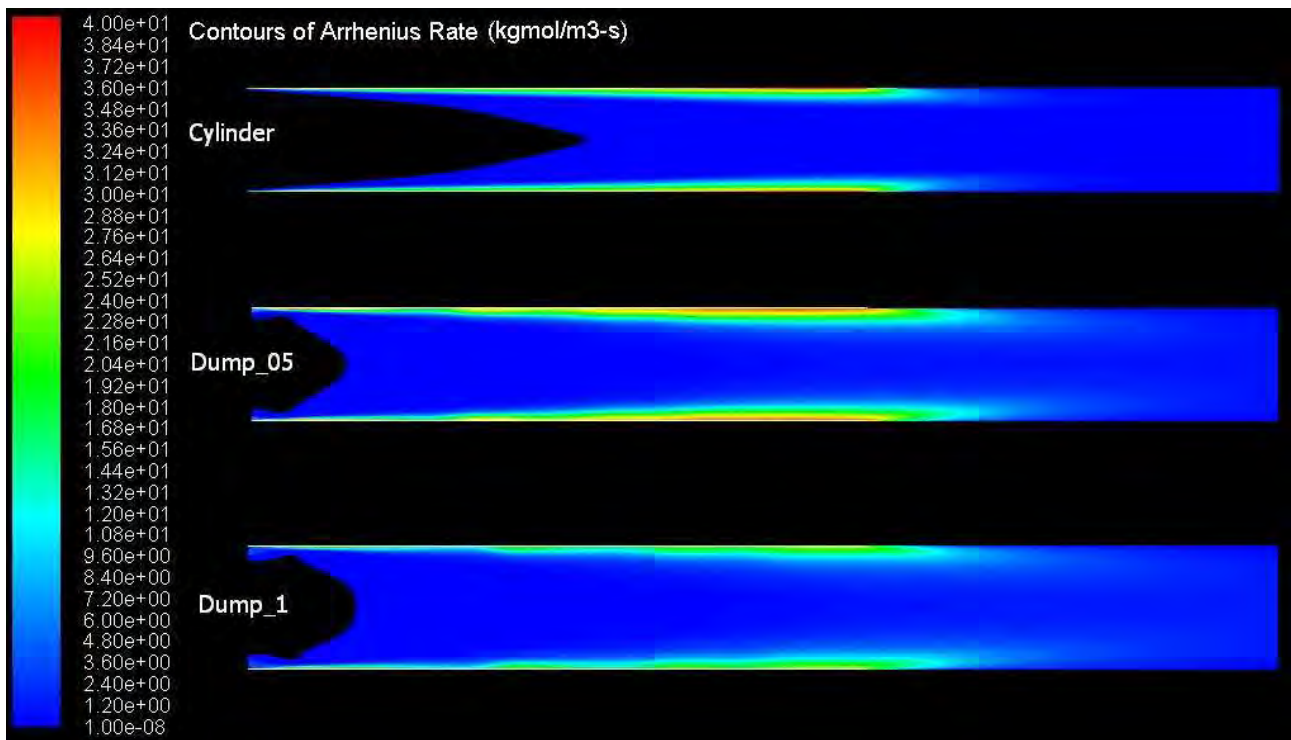
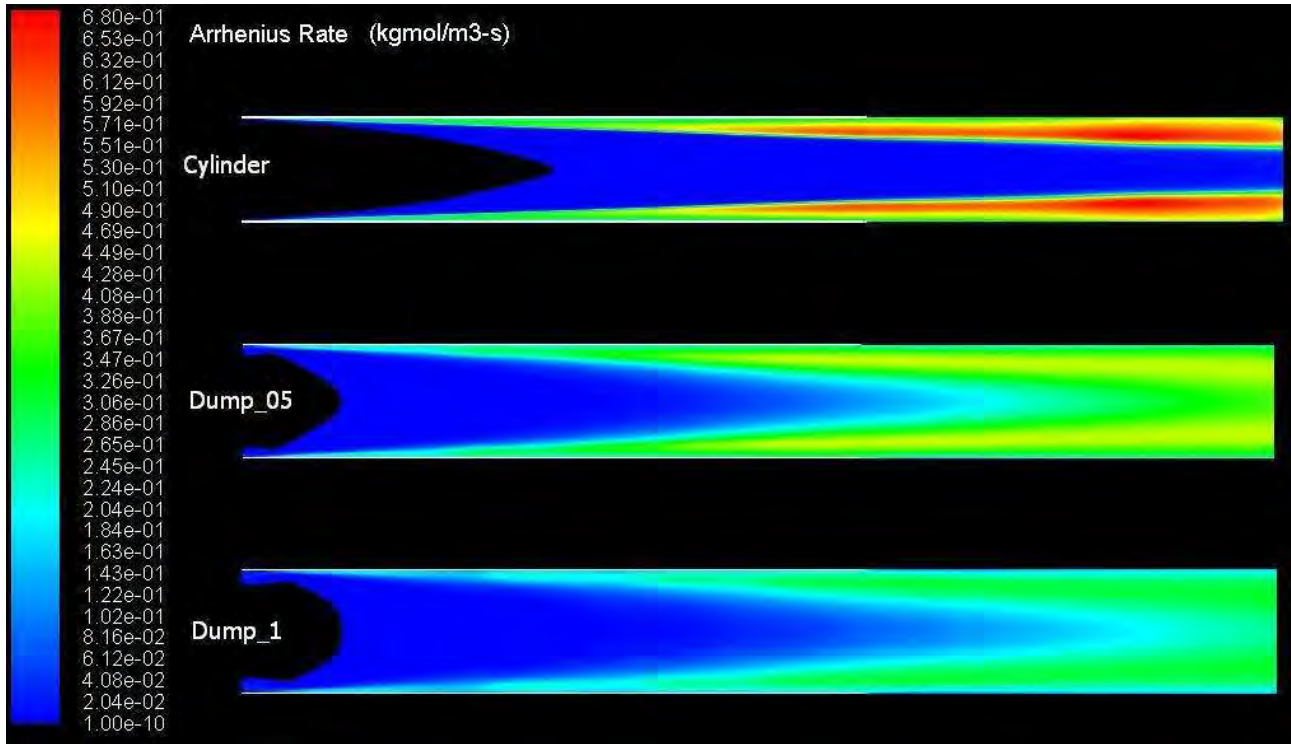


Fig. 57: Comparison among contours of H<sub>2</sub>/O<sub>2</sub> reaction rate

In both cases (Dump05 and Dump1 combustors) the  $H_2/O_2$  reaction is mainly developed over the grain, being more intense in the Dump05 configuration and, conversely, more extended downstream the grain for the Dump1 configuration.

Analogous considerations holds for the  $Li/O_2$  reaction, mainly present downstream the grain and reaching the core flow before the exit section.



**Fig. 58: Comparison among contours of  $Li/O_2$  reaction rate**

To complete the description of the flow path in the Dump1 combustor, the contours of pressure, Mach number and mixing time of both reacting and non reacting cases are also reported in the following figures 59, 60, 61.

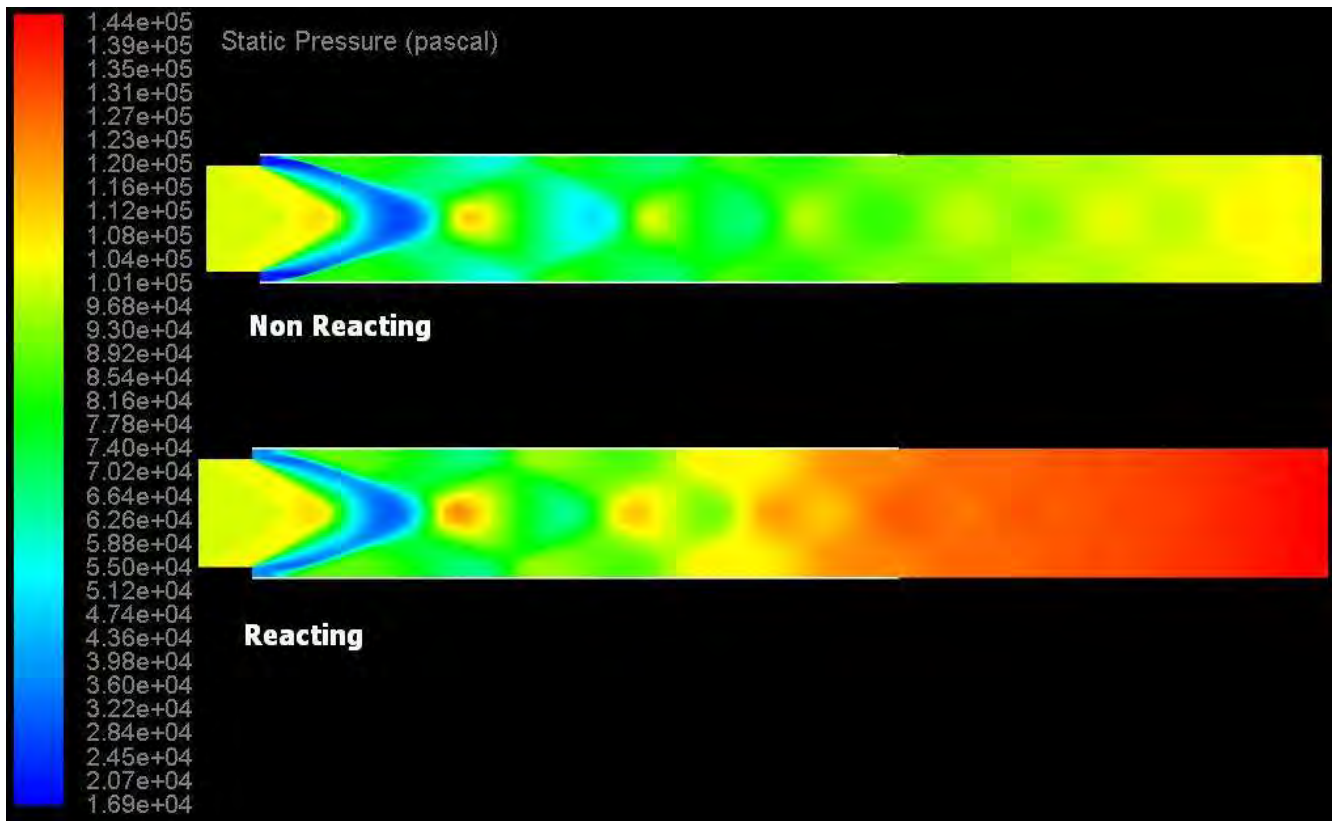


Fig. 59: Contours of static pressure (reacting and non reacting case)

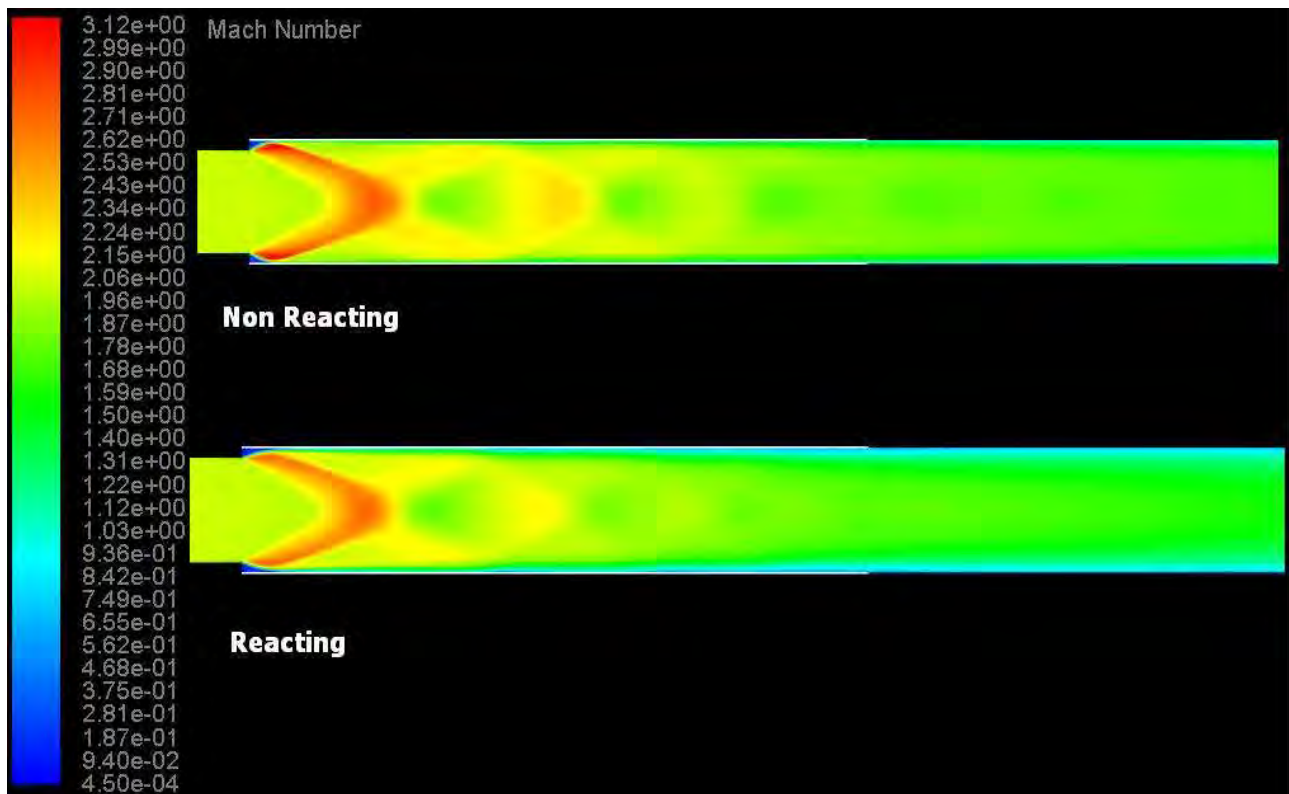


Fig. 60: Contours of Mach number (reacting and non reacting case)

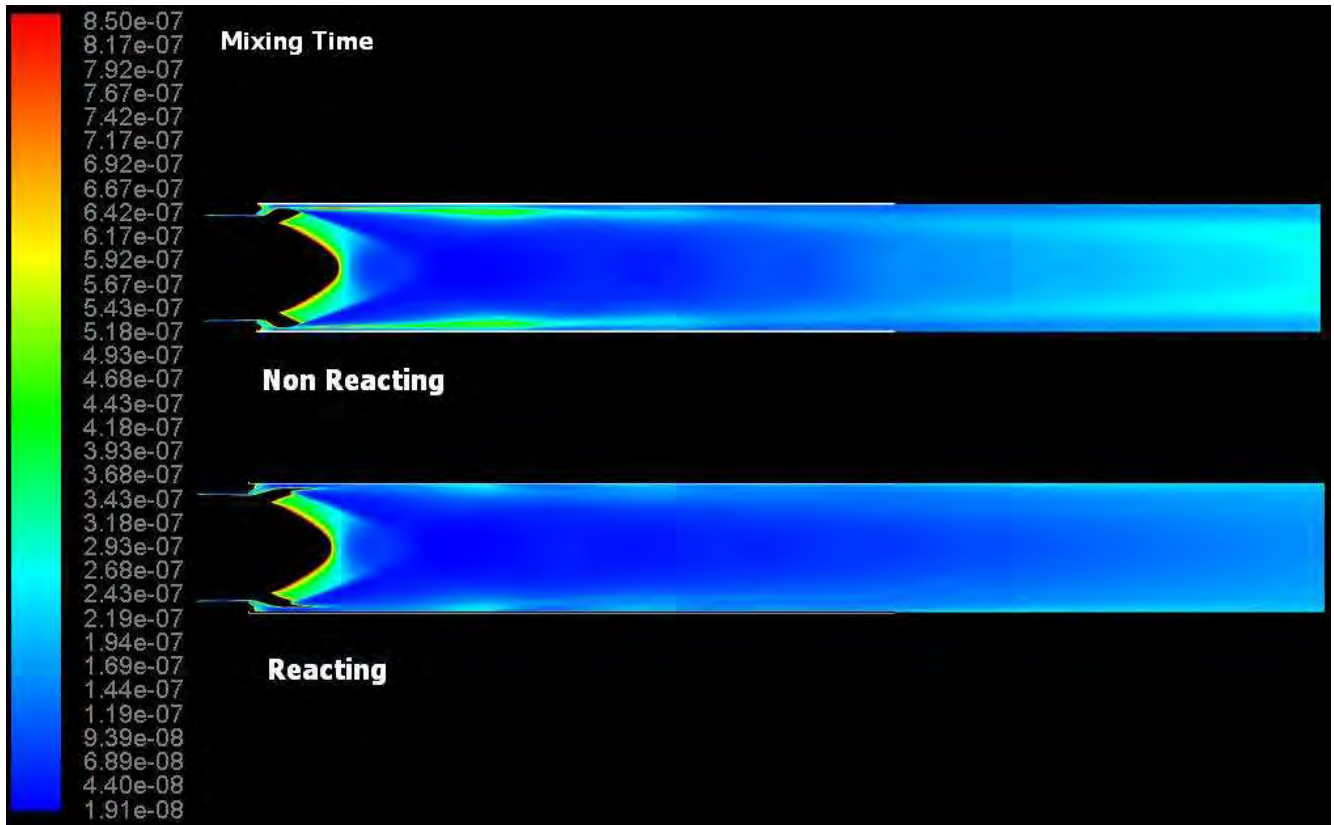


Fig. 61: Contours of mixing time (reacting and non reacting case)

## IV Conclusions

The analysis performed has shown that LiH, when used as fuel, offer performance comparable with those of commonly used fuels such as  $\text{LCH}_4$  and  $\text{LH}_2$ .

During this preliminary phase we have in particular explored their ability to release hydrogen by thermal decomposition, showing that LiH behaves not only as safe and compact hydrogen carrier system, but also as powerful bi-fuels systems, especially when Li is injected separately into the hot stream of  $\text{H}_2/\text{O}_2$  exhaust.

To overcome the scarcity (or non-existence) of data concerning LiH combustion at high temperature, we have investigated the behaviour of LiH at conditions similar to those expected in a scramjet combustion chamber by assuming chemical equilibrium. Results have been used to identify main species and reactions involved in the process; in particular we have highlighted the presence of large amount of hydrogen and lithium produced by thermal decomposition. This feature was stressed comparing the few theoretical and experimental data available in the open literature with those obtained from our simulation; as a result we have demonstrated that at high temperature the main responsible for the performance of LiH (together with the gaseous hydrogen produced) is the liquid lithium.

Still to overcome the non-existence of data concerning the Li combustion in presence of air, we have performed a similar parametric analysis based on simulations at chemical equilibrium. Results show that at temperature higher than 1100 K Li does not react with air nitrogen; moreover burning in oxygen it produces mainly gaseous  $\text{Li}_2\text{O}$ , showing at the same time many similarities, in terms of equilibrium composition, with  $\text{H}_2/\text{O}_2$  combustion. By means of a thermochemical analysis, we have thus compared the reactions potentially involved in Li combustion, concluding that as a first approximation, the reaction scheme can be simplified assuming an one-step global reaction. Furthermore, we have assumed that the rate of this reaction may be reasonably described by means of the reaction rate proposed by Plane et Rajasekhar. for the reaction forming Li superoxide.

We have then defined the physical model describing step by step the fuel injection from the grain surface; we have demonstrated, by means of an order of magnitude analysis, that almost all liquid lithium droplets produced by LiH thermal decomposition (and dragged away by the turbulent stream), vaporize and burn before exiting the combustor, contributing in a significant manner to heating the flow.

To complete our investigation, we have also performed a CFD simulation using as test cases three combustor geometries similar to those investigated by Jakimovicz et al. and Ben-Arosh et al. To describe the fuel injection process from the decomposing LiH grain we have defined and implemented a numerical model based on formulating mass, momentum, energy and species sources located near the surface.

Despite the limitations due to the adoption of a standard k-e model, and to the assumption made about the  $\text{Li}/\text{O}_2$  reaction rate, results are intriguing. The blowing model adopted describes fuel injection in a plausible way, if not correctly (as indicated when comparing the regression rates obtained with those calculated by Jarymowycz et al. and Ben-Arosh). An intense flame zone is predicted to be present over the decomposing surface and downstream of the grain in the cylindrical configuration; the flame does not extinguish and high temperatures (of order 2900 K) are obtainable. Introducing a sudden cross section enlargement (a 'dump') downstream of the inlet section, mixing in the combustor is enhanced, also increasing the heat released to the core flow. However, an excessive dump ratio decreases the core flow temperature (due to expansion waves) and increases the combustor volume, lowering the combustor performance.

To conclude we can state that LiH is an ideal candidate for solid fuelled scramjet applications, behaving as an high energy density bi-fuel system but also as a safe and compact hydrogen carrier.

## V. References

- [1] EOARD 2011 FA8655-10-1-3091 ITEM0001
- [2] EOARD 2011 FA8655-10-1-3091 ITEM0002
- [3] P. A. Czysz, C. Bruno, "Future Spacecraft Propulsion Systems – Enabling Technologies for Space Exploration", Springer-Verlag Berlin Heidelberg NY, ISBN 10: 3-540-23161-7
- [4] Heiser and D. T. Pratt, *Hypersonic Airbreathing Propulsion*, AIAA Education Series, III series, ISBN 1-56347-035-7, Washington, DC, 1994;
- [5] H. Wittenberg, *Some Fundamentals on the Performance of Ramjet with Subsonic and Supersonic Combustion*, TNO PrinsMaurits laboratory, ISBN 90-407-2024-X, The Netherlands, 2000;
- [6] J. L. Hunt, R. J. Pegg, D. H. Petley, *Airbreathing Hypersonic Vision: Operational - Vehicles Design Matrix*, NASA Langley Research Center, ISBN 1999-01-5515, Hampton, VA, 1999;
- [7] L. H. Townend, *Domain of the Scramjet*, Journal Of Propulsion And Power Vol 17, No 6 November –December, 2001
- [8] U. B. Mehta and J. V. Boweles, *Two-Stage-to Orbit Spaceplane Concept with Growth Potential*, Journal of Propulsion and Power, Vol 17, No 6, November –December 2001;
- [9] Hicks, J.W., Flight testing of Airbreathing Hypersonic Vehicles, NASA Technical Memorandum 4524, Dryden Flight Research Facility, Edwards, California, Ottobre 1993;
- [10] H. Wittenberg, *Some Fundamentals on the performance of Ramjets with Subsonic and Supersonic Combustion*, TNO Prints Maurits Laboratory, Netherlands, 2000;
- [11] E. T. Curran, W. H. Heiser and D. T. Pratt, *Fluid Phenomena in Scramjet Combustion System*, Annual Reviews Fluid Mechanics, Vol. 28, pagg. 323-360, 1996
- [12] D. Simone, C. Bruno, "Lithium Hydride for Microrockets Applications," 2nd International Conference on Green Propellants, Sardinia, Italy, June 6-7, 2004
- [13] D. Simone, C. Bruno, "Lithium Hydride as Propellant for Missile Applications," Workshop on Hybrid Propulsion for Tactical Applications," Colleferro, Rome, Italy, July 19-20, 2004
- [14] D. Simone, C. Bruno, "LiH as Fuel for Aerospace Propulsion", Paper ISTS-a-38, 25 ISTS Conference, Kanazawa, Japan, June 3-8, 2007;
- [15] Y. Ju, J. Austin, "AIAA - The Year in Review", Aerospace America, p. 55, December 2006
- [16] B. Hidding and M. Pfitzner, Rocket Propellant Characteristics of Silanes/O<sub>2</sub>, Journal of Propulsion and Power Vol. 22, No. 4, 2006
- [17] E.A. Fletcher, Scramjets and Surfboards: Some Forgotten History, Journal of Propulsion and Power, Vol. 23, No. 1, 2007
- [18] D. Simone, C. Bruno and B. Hidding, Silanes as Fuels for Scramjets, Journal of Propulsion and Power Vol. 22, No. 5, 2006
- [19] B. Hidding, M. Pfitzner, D. Simone and C. Bruno, Silanes/H<sub>2</sub>O<sub>2</sub> - A High-Performance Synthetic Bipropellant for Chemical Space Propulsion, Technical Note, accepted for publication, September 2007
- [20] Y. Ju, K. McManus, "AIAA - The Year in Review", Aerospace America, p. 62, December 2005

- 
- [21] R. Ben-Arosh, B. Natan, E. Spiegler and A. Gany: "Theoretical study of a Solid Fuel Scramjet Combustor", *Acta Astronautica*, Vol. 45, No. 3, pp. 155-166, 1999.
- [22] A. Ben-Yakar, B. Natan and A. Gany: "Investigation of a Solid Scramjet Combustor", *Journal of Propulsion and Power*, Vol. 14, No. 4, pp. 447-455, 1998.
- [23] A. Coen-Zur, B. Natan: "Experimental Investigation of a Supersonic Combustion Solid Fuel Ramjet", *Journal of Propulsion and Power*, Vol. 14, No. 6, pp. 880-889, 1998.
- [24] T. A. Jarymowycz, V. Yang and K. K. Kuo: "Numerical study of Solid-Fuel Combustion Under Supersonic Crossflows", *Journal of Propulsion and Power*, Vol. 8, No. 2, pp. 346-353, 1992.
- [25] R. Ben-Arosh, B. Natan, E. Spiegler and A. Gany: "Fuel-Air Mixing In Solid Fuel Scramjet Combustor", *International Journal of Turbo and Jet Engines*, Vol. 15, 1998, pp. 223-234
- [26] S. Gordon, J. B. McBride, "Computer Program for Calculation of Complex Chemical Equilibrium Compositions and Applications," NASA Reference Publication 1311, October 1994
- [27] D. G. Clifton, L. R. Sitney: "Theoretical Specific Impulses of Lithium-based Propellant Systems in Nuclear and Chemical Rockets", LA-2276, Los Alamos Scientific Laboratory, New Mexico, 1959.
- [28] T. L. Purpoint, J. J. Rousek: "Novel Organometallic Propellants for Hypergolic Applications", Swift Enterprises, Ltd., West Lafayette, Indiana, U.S.A.
- [29] F. H. Welch: "Lithium Hydride Properties", General Electric Aircraft Nuclear Propulsion Department, DC 61-3-73, March 14, 1961.
- [30] C. E. Holley, Jr., G. E. Challenger, D. Pavone: "The preparation of Pure Lithium hydride", LA-1705, Los Alamos Scientific Laboratory, New Mexico, 1955.
- [31] V. N. Brinza, I. V. Bavaitsev, S. T. Papaev: "Investigation of the Combustion Rate of Aerosuspensions of Lithium Hydride Powder", *Journal of Combustion, Explosion and Shock Waves*, Vol. 15, No. 1, pp. 100 – 101, 1979.
- [32] M. Balooch, L. N. Dinh, D. F. Calef: "The Reaction Kinetics of Lithium Salt with Water Vapor", *Journal of Nuclear Materials*, No. 303, 2002, pp. 200-209.
- [33] L. N. Dinh, D. M. Grant et al.: "Kinetics Measurement and Prediction of the Hydrogen Outgassing from the Polycrystalline LiH/Li<sub>2</sub>O/LiOH System", *Journal of Nuclear Materials*, No. 347, 2005, pp. 31-43.
- [34] C. Haertling, R. J. Hanarahan Jr., R. Smith: "A Literature Review of Reactions and Kinetics of Lithium Hydride Hydrolysis", *Journal of Nuclear Materials*, No. 349, 2006, pp. 195-233.
- [35] L. V. Gurvich, G. A. Bergman et al.: "Thermodynamic Properties of Alkali Metal Hydroxides. Part 1. Lithium and Sodium Hydroxides", *J. Phys. Chem. Ref. Data*, Vol. 25, No. 4, 1996, pp. 1211-1276.
- [36] F. E. Pretzel, D. T. Vier, E. G. Szklarz, W. B. Lewis: "Radiation Effects on Lithium Hydride", LA-2463, Los Alamos Scientific Laboratory, New Mexico, 1962.
- [37] S. Chung, H. Morioka: "Thermochemistry and Crystal Structures of Lithium, Sodium and Potassium Alanates as Determined by Ab-initio Simulations", *Journal of Alloys and Compounds*, No. 372, 2004, pp. 92-96.
- [38] H. S. Taylor: "The Potential Energy curve of the Lowest Lying Triplet Sigma State of Lithium Hydride", Technical report No. 32-493, Jet Propulsion Laboratory, California Institute of Technology, Pasadena, California, 1963.
- [39] A. W. McClaine, R. W. Breault et al. : "Hydrogen Transmission/Storage with Metal Hydride Organic Slurry and Advanced Chemical Hydride/Hydrogen for PEMFC vehicles", U.S. Department of Energy (DOE) Award Nos. DE-FC02-97EE50483
- [40] E. Veleckis, E. H. Van Deventer, M. Blander: "The Lithium – Lithium Hydride System", *The Journal of Physical Chemistry*, Vol 78, No. 19, 1974.

- 
- [41] J. V. Vogt: "Measurement of Thermal Properties of LiH and LiH-Li Mixtures: Enthalpy, Heat of Fusion, Conductivity", Topical Report ER-4809, TAPCO – Thompson Ramo Wooldridge Inc., Cleveland, OH, U.S.A., 1962.
- [42] E. E. Shpil'rayn, K.A. Yakimovich, D. N. Kagan, V. G. Shval'b: "A Theoretical and Experimental Study of the Thermophysical Properties of Lithium Hydride", NASA TT-20179, April, 1988.
- [43] K. A. Yakimovich, A. F. Tsitsarkin, A. G. Mozgovoi: "Experimental Investigation Of the Density of Liquid Lithium Hydride at High Temperatures", High Temperature, Vol 38, No. 6, 2000, pp. 867-874.
- [44] H. Kawano, Y. Zhu, A. Tanaka: "Thermal desorption of H<sub>2</sub>, H- and Electron by Temperature-Programmed Heating of Saline Hydrides in Vacuum", Thermochimica Acta 344, 2000, pp. 119-125.
- [45] S. W. Mayer, L. Schieler: "Computed Activation Energies and Rate Constants for Forward and Reverse Transfers of Hydrogen Atoms", The Journal of Physical Chemistry, Vol 72, No. 1, 1968.
- [46] S.W. Mayer, L. Schieler, H. Johnston: "Compute High-Temperature Rate Constant for Hydrogen-Atom Transfers Involving Light Atoms", The Journal of Chemical Physics, Vol. 45, No. 1, July 1966.
- [47] B. Jerry, L. Modisette: "Preliminary Investigation of Lithium Hydride as High-temperature Internal Coolant", NACA RM L57B12a, Washington, 1957.
- [48] B. Jerry, L. Modisette: "Investigation of Lithium Hydride and Magnesium as High-temperature Internal Coolants with Several Skin Materials", NACA RM L58B17, Washington, 1958.
- [49] H. W. Davison: "Compilation of Thermophysical Properties of Liquid Lithium", NASA Technical Note, NASA TN D-4650, July 1968.
- [50] G. E. Jaynes, G. S. Hanks, J. M. Taub, D. T. Doll: "The Fabrication of Lithium", Los Alamos Scientific Laboratory report LA-1191, January 1951.
- [51] R. K. Williams, G. L. Coleman, D. W. Yarbrough: "An Evaluation of Some Thermodynamic and Transport Properties of Solid and Liquid Lithium over the Temperature Range 200-1700 K", Oak Ridge National Laboratory report ORNL/TM-10622, March 1988.
- [52] D. W. Jeppson: "Interaction of Liquid Lithium with Various Atmospheres, Concretes, and Insulating Metals; and Filtration of Lithium Aerosols", Hanford Engineering Development Laboratory report HEDL-TME 79-7, 1978.
- [53] D. A. Dube, M. S. Kazimi: "Analysis of design Strategies for Mitigating the Consequences of Lithium Fire Within Containment of Controlled Thermonuclear Reactors", Department of Nuclear Engineering, Massachusetts Institute of Technology report MITNE-219, July 1978.
- [54] I. O. Bohachevsky, L. A. Booth, J. F. Hafer: "Lithium Flow on the Inside of a Spherical Fusion-Reactor Cavity", Los Alamos Scientific Laboratory report LA-6362-MS, June 1976.
- [55] M. S. Tillack, M. S. Kazimi: "Development and Verification of the LITFIRE Code for Predicting the Effects of Lithium Spills in Fusion reactor Containments", Department of Nuclear Engineering, Massachusetts Institute of Technology report PFC/RR-80-11, July 1980.
- [56] V. J. Gilberti, M. S. Kazimi: "Modeling of lithium and Lithium-Lead Reactions in Air Using LITFIRE", Plasma Fusion Center and the Department of Nuclear Engineering, Massachusetts Institute of Technology report PFC/RR-83-08, January 1983.
- [56] E. Yakimiak Jr., M. S. Kazimi: "Safety Analysis of Liquid Lithium-Lead Breeders in Fusion Reactor Geometries", Plasma Fusion Center and the Department of Nuclear Engineering, Massachusetts Institute of Technology report PFC/RR-84-10, June 1984.

- 
- [57] T. K. Gil, M. S. Kazimi: "The Kinetics of Lithium Reaction With Oxygen-Nitrogen Mixtures", Plasma Fusion Center and the Department of Nuclear Engineering, Massachusetts Institute of Technology report PFC/RR-86-1, January 1986.
- [58] D. S. Barnett, M. S. Kazimi: "Consequence of a Lithium Spill Inside the Containment and Vacuum Torus of a Fusion Reactor", Plasma Fusion Center and the Department of Nuclear Engineering, Massachusetts Institute of Technology report PFC/RR-87-9, June 1987.
- [59] D. S. Barnett, M. S. Kazimi: "The Chemical Kinetics of the Reactions of Lithium With Steam-Air Mixtures", Plasma Fusion Center and the Department of Nuclear Engineering, Massachusetts Institute of Technology report PFC/RR-89-3, April 1989.
- [60] T. T. Utschig, M. L. Corradini: "Computer Modeling for Lithium Safety in Fusion Systems: LINT and MELCOR", Fusion Technology Institute, University of Wisconsin report UWFD-1101, June 1999
- [61] B. J. Merrill: "Modification Made to the MELCOR Code for Analyzing Lithium Fires in Fusion Reactors", Idaho National Engineering and Environmental Laboratory report INEEL/EXT-2000-00489, April 2000.
- [62] D. L. Hildenbrand, W. F. Hall and N. D. Potter: "Thermodynamics of Vaporization of Lithium Oxide, Boric Oxide, and Lithium Metaborate", The Journal of Chemical Physics, Vol. 39, No. 2, July 1963, pp. 296-301
- [63] R. Patrick, D. M. Golden, "Termolecular Reaction of Alkali Metal Atoms with O<sub>2</sub> and OH", International Journal of Chemical Kinetics, Vol. 16, 1984, pp. 1567-1574
- [64] J. M. C. Plane, B. Rajasekhar: "A Study of the Reaction Li + O<sub>2</sub> + M (M = N<sub>2</sub>, He) over the Temperature Range 267 – 1100 K by Time Resolved Laser-Induced Fluorescence of Li (2<sup>2</sup>P<sub>J</sub>-2<sup>2</sup>S<sub>1/2</sub>)", J. Phys. Chem., Vol 92, 1988, pagg 3884-3890
- [65] NIST Chemistry WebBook <http://webbook.nist.gov/chemistry/>
- [66] W. Heiser, D. Pratt, "Hypersonic Airbreathing Propulsion", *AIAA Education Series*, 1994.
- [67] J.D. Anderson, "Hypersonic and high temperature gas dynamics", *McGraw-Hill*, 1989
- [68] H. Schlichting, "Boundary-layer Theory", *McGraw-Hill*, 1979
- [69] The Engineering Tool Box: <http://www.engineeringtoolbox.com/>
- [70] R. A. Svelha, "Estimated Viscosities and Thermal Conductivities of Gases at High temperatures", NASA TR-132, 1962
- [71] S. R. Turns, "An Introduction to Combustion", *McGraw-Hill*, 1996
- [72] F. A. Williams, "Combustion Theory", The Benjamin/Cummings Publishing Company, Inc., 1985
- [73] K. K. Kuo, "Principles of Combustion", John Wiley & Sons Inc., 1986.
- [74] S. B. Pope, "Turbulent Flows", Cambridge University Press, 2000
- [75] Pilch, M. and C. Erdman: "Use of break-up time data and velocity history data to predict the maximum size of stable fragments for acceleration-induced break-up of a liquid drop", Int. J. Multiphase Flow, 13, 1987, pp 741-757.
- [76] D. D. Joseph, J. Belanger & G.S. Beavers, "Breakup of a liquid drop suddenly exposed to a high-speed airstream", *University of Minnesota, Minneapolis, MN 55455*
- [77] R.S. Brodkey, "The Phenomena of Fluid Motions", Addison Wesley, Reading, MA., 1969.
- [78] J. R. Fessler, J. K. Eaton, "Turbulence Modification by Particles in a backward-facing step flow", J Fluid Mechanics, Vol 394, 1999, . pp 97 – 117.
- [79] G. P. Sutton, "Rocket Propulsion Elements, An Introduction to the Engineering of Rockets", John Wiley & Sons, Inc, 1992

- [80] C. Carmicino, “Alcuni Aspetti della Balistica Interna di un Endoreattore a Propellenti Ibridi e del Comportamento di Ugelli a Spina troncata”, Tesi di Dottorato di Ricerca in Ingegneria Aerospaziale, XV Ciclo, Università di Napoli Federico II, 2002.
- [81] C. Fournier, M. Michard and F. Bataille, “Numerical Simulations of a Confined Channel Flow Driven by Non-Isothermal Wall Injection”, Progress in Computational Fluid Dynamics, Vol 6, Nos 1/2/3, 2006
- [82] Ansys Fluent 6.3, User’s Guide Manual, 2007

## Appendix

### A1 Evaporation

The simplified evaporation model adopted assumes that the droplet surface temperature  $T_s$ , after a transient period in which the droplet rapidly heats up to a steady temperature, is near the liquid lithium boiling point ( $T_b = 1615\text{ K}$ ); this means that thanks to its high thermal conductivity  $k_l$  liquid lithium opposes a negligible thermal inertia and, hence, the evaporation rate is controlled by the heat transfer rate from the ambient to the droplet surface, see figure A1

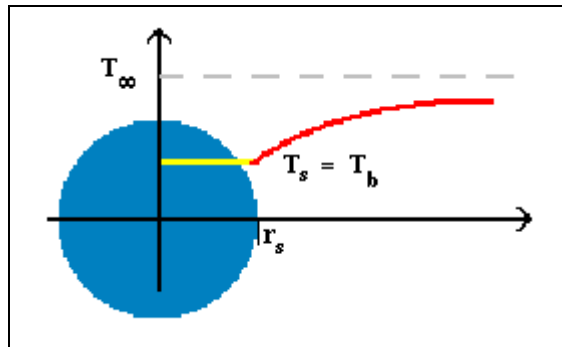


Fig. A1: Droplet and environment temperature profile adopted in the model

This assumption is justified considering that liquid lithium possesses a high thermal diffusivity ( $D^{th} \approx 5 \cdot 10^{-5} \text{ m}^2/\text{s}$ ): the characteristic time required to heat a  $10\mu\text{m}$  diameter droplet is thus of order  $10^{-6} \text{ s}$ , that is three orders of magnitude lower than the convective time.

Physically, heat from the environment supplies the energy necessary to vaporize the liquid fuel, and the fuel vapor then diffuses from the droplet surface into the core gas. The mass loss causes the droplet radius to shrink with time until the droplet is completely evaporated. This is a good approximation especially for the scramjet combustion chamber where the expected maximum temperature is very high ( $T_c$  about  $3500\text{ K}$ ); thus the problem is reduced to determining the mass flowrate of the fuel vapor from the surface at any instant in time. Knowledge of this will then enable us to calculate the droplet radius as a function of time, and droplet lifetime.

In summary, the model includes the following assumptions, commonly adopted in evaporation problems because they lead to great simplification while maintaining a reasonable agreement with experimental results.<sup>71</sup>

- The droplet evaporates in a quiescent, infinite medium.
- The evaporation process is quasi-steady. This means that at any instant in time the process can be described as if it were in steady state. This assumption eliminates the need to deal with partial differential equations.
- The fuel is a single-component liquid with zero solubility for other gases present.
- After a short transient, the droplet temperature is uniform, and, furthermore, the temperature is assumed to be the lithium boiling point,  $T_d = T_b$ . In many problems, the transient heating of the liquid does not greatly affect the droplet lifetime, and more rigorous calculations show that the droplet surface temperature is only slightly less than the liquid boiling point in combustion environments. This assumption eliminates the need to solve a liquid-phase (droplet) energy equation, and, more importantly, eliminates the need to solve the fuel vapor transport (species) equation in the gas phase. Implicit in this assumption is that  $T_\infty > T_b$ .
- We assume binary diffusion with a unity Lewis number ( $\alpha = D$ ). This permits us to use the simple Shvab - Zeldovich treatment for the energy equation.
- We also assume that all thermophysical properties, such as thermal conductivity, density, and specific heat, are constant. Although these properties may vary greatly as we move through the gas phase from the droplet surface to the faraway surroundings, constant properties allow a simple closed-form solution. In the final analysis, a judicious choice of mean values allows reasonably accurate predictions to be made.

Using these we can find the vaporized lithium mass flowrate focusing only on the gas phase analysis; thus we can write the mass conservation equation as:

$$\dot{m} = \rho v_r 4 \pi r^2 = \text{constant} \quad (\text{A1.1})$$

where  $\dot{m}$ ,  $r$ ,  $v_r$  are respectively the gaseous lithium mass flowrate (constant because of steady state evaporation assumptions), its density and the bulk flow velocity. Thus the conservation of energy is:

$$\frac{d \left( r^2 \frac{dT}{dr} \right)}{dr} = \frac{\dot{m} c_{pg}}{4\pi k} \frac{dT}{dr} \quad (\text{A1.2})$$

where we have assumed that no reaction are present. This equation requires the following boundary conditions:

$$\text{far from the droplet : } T(r \rightarrow \infty) = T_{\text{stream}}$$

$$\text{at the drop surface: } T = T_{\text{boil}}$$

Finally we can write the droplet – gas phase interface energy balance as

$$\dot{Q}_{\text{cond}} = 4 \pi k_g r_s^2 \left. \frac{dT}{dr} \right|_{r_s} = \dot{m} (h_{\text{vap}} - h_{\text{liq}}) + \dot{m} \Delta h_{\text{heating}} \quad (\text{A1.3})$$

where  $\Delta h_{\text{fg}} = \dot{m} (h_{\text{vap}} - h_{\text{liq}})$  is the lithium latent heat of vaporization and  $\Delta h_{\text{heating}}$  is the heat required to reach the lithium boiling temperature.

Solving equation (A1.3) we obtain the temperature distribution as a function of the droplet diameter; thus differentiating this relation, substituting in (A1.3) and solving for  $\dot{m}$  we obtain:

$$\dot{m} = \frac{4 \pi k_g r_s}{c_{pg}} \ln (B_q + 1) \quad (\text{A1.4})$$

where  $B_q$ , sometimes referred to as the Spalding number or transfer number, is:

$$B_q = \frac{c_{pg} (T_{\infty} - T_{\text{boil}})}{\Delta h_{\text{fg}} + \Delta h_{\text{heating}}} \quad (\text{A1.5})$$

The droplet lifetime can thus determined by following its radius history by writing an equation stating that the rate of the droplet mass consumption equals the vaporized mass flowrate:

$$\frac{dm_d}{dt} = - \dot{m} \quad (\text{A1.6})$$

and, since  $m_d = \rho_L V = \rho_L \pi D^3/6$  we can write a relation that is commonly expressed in terms of  $D^2$  rather than  $D$ :

$$\frac{dD^2}{dt} = - \frac{8 k_g}{\rho_L c_{pg}} \ln (B_q + 1) \quad (\text{A1.7})$$

and, solving:

$$D^2(t) = D_0^2 - K t \quad (A1.8)$$

with  $K = \frac{8 k_g}{\rho_L c_{pg}} \ln(B_q + 1)$  defined as the evaporation constant (figure A1.2) and  $D_0$  the initial droplet diameter.

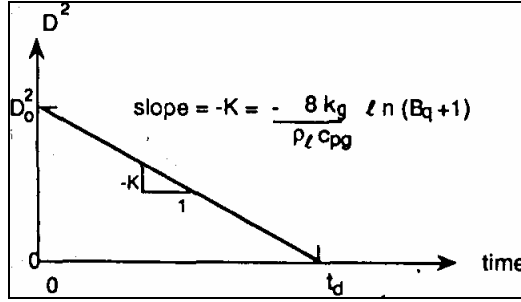


Fig. A1.2:  $D^2$  law

We can find the time it takes a droplet of given initial size to completely evaporate, i.e., the droplet lifetime  $t_d$ , by setting  $D^2(t_d) = 0$ :

$$t_d = \frac{D_0^2}{K} \quad (A1.9)$$

For the case under examination this characteristic time was calculated as a function of the temperature with the drop diameter as parameter; this choice was made because during the residence time in the combustion chamber the droplet are exposed to a temperature field, depending on where along the chamber axis they are released and heated. Due to the temperature dependence of the air thermal conductivity  $k_g$  and constant pressure specific heat  $c_{pg}$ , an average value  $T_m$  was defined for every ambient temperature:<sup>71, 72</sup>

$$T_m = (T_{boil} + T_\infty) / 2 \quad (A1.10)$$

Thus  $k_g$  and  $c_{pg}$  were calculate as average values of the air and lithium properties calculated at  $T_m$ :

$$c_{pg} = c_{p(Li)}(T_m) \quad (A1.11)$$

and

$$k_g = 0.4 k_{(Li)}(T_m) + 0.6 k_{air}(T_m) \quad (A1.12)$$

Lithium and air properties were calculated using the polynomials in the CEA600 database; results are shown in figure A1.3

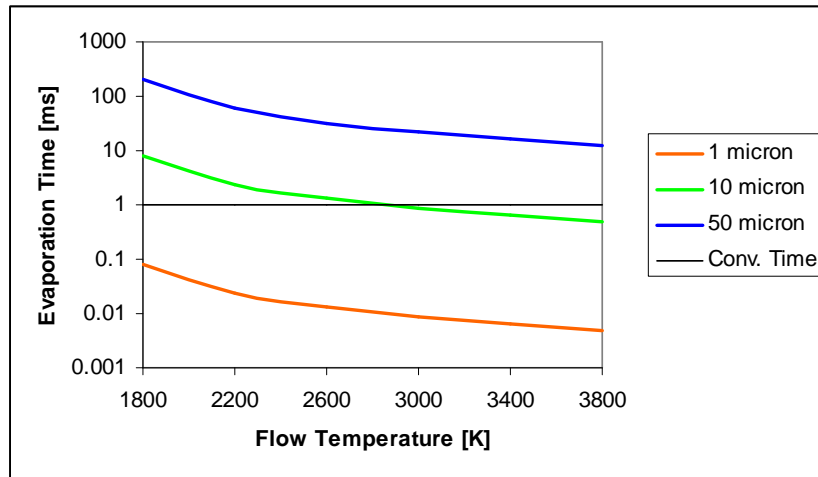


**Fig. A1.3: Evaporation rate**

As we can see the lifetime of droplets having diameters of few microns is of the order of ten millisecond at low temperatures (typical of the initial transient phase or far from the reacting zone); however it is important to highlight that these values are relatives to a quiescent and non reacting environment so neglecting the convective heat transfer and the coupled effects of the fuel mass driven diffusion and combustion. These will be analyzed in the next section.

### A1.1 Droplets evaporation and burning<sup>71</sup>

We can extend the model developed in the preceding section including a spherically symmetric diffusion flame that surrounds the droplet. While retaining the assumption of a quiescent environment and spherical symmetry and short heat-up time made in the initial development, we now couple in the analysis the mass and heat transfer. The method is thus based on the following assumptions:

- The burning droplet, surrounded by a spherically symmetric flame, exists in a quiescent, infinite medium. There are no interactions with any other droplets, and the effects of convection are ignored. This reasonable, as the droplets are stripped from the surface, so that the relative velocity is either zero or very small compared to the core gas velocity.

- As in our previous analysis, the burning process is quasi-steady.
- The fuel is a single-component liquid with zero solubility for gases. Phase equilibrium prevails at the liquid–vapor interface.
- The pressure is uniform and constant.
- The gas phase consists of only three "species:" lithium vapor, air and combustion products. The gas-phase region is divided into two zones. The inner zone between the droplet surface and the flame contains only lithium vapor and products, while the outer zone consists of air and products. Thus, binary diffusion prevails in each region.
- Lithium and air react in stoichiometric proportions at the flame. Chemical kinetics is assumed to be infinitely fast, resulting in the flame being represented as an infinitesimally thin sheet.
- The Lewis number is unity.
- Radiation heat transfer is negligible.
- The gas-phase thermal conductivity,  $k_g$ , specific heat,  $c_{pg}$  and the product of the density and mass diffusivity,  $\rho D$  are all constants.
- The liquid fuel droplet is the only condensed phase.

A schematic representation of the model is shown in figure A1.4 where we have outlined the process driving factors (that is the temperature and mass fraction gradients) as a function of the radial distance from the droplet core.

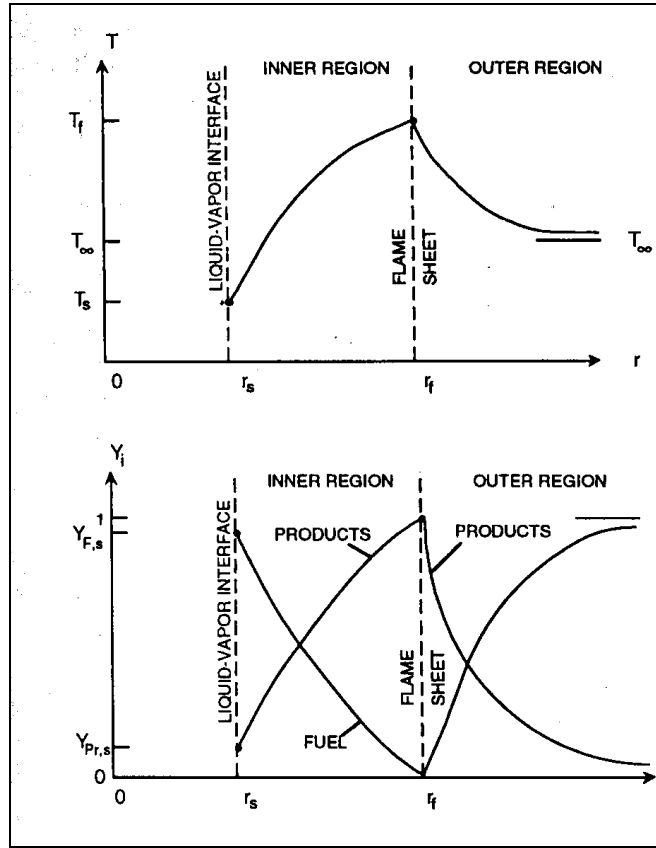


**Fig. A1.4: Temperature and mass fractions as a function of the radial distance**

This model thus involves the simultaneous solution of the following set of equation:

- An equation governing the lithium conservation in the inner region (that is  $r_s < r < r_f$  with  $r_s$  and  $r_f$  respectively the surface and flame sheet radial coordinates)
- An analogous equation governing the air species conservation in the outer region ( $r_f < r < r_\infty$ )
- The energy conservation at the droplet liquid-vapor interface
- The energy balance at the flame sheet
- The Clausius - Clapeyron equation governing the liquid-vapor equilibrium at the interface.

Solving the corresponding equation system we obtain the vaporized lithium mass flowrate:

$$\dot{m} = \frac{4 \pi k_g r_s}{c_{pg}} \ln (B_{o,q} + 1) \quad (\text{A1.13})$$

were  $\Delta h_c$  is heat of combustion and  $v$  is the lithium-air stoichiometric mass ratio; thus the transfer number  $B_{o,q}$  is defined as:

$$B_{o,q} = \frac{\frac{\Delta h_c}{v} + c_{pg} (T_\infty - T_s)}{\Delta h_{fg} + \Delta h_{heating}} \quad (A1.14)$$

the burning rate constant is:

$$K = \frac{8 k_g}{\rho_L c_{pg}} \ln (B_{o,q} + 1) \quad (A1.15)$$

and the droplet lifetime:

$$t_d = \frac{D_0^2}{K} \quad (A1.16)$$

As with the pure evaporation problem, the appropriate values of the gas thermal conductivity  $k_g$  and constant pressure specific heat  $c_{pg}$  were calculated defining an average temperature  $T_m$ ; since  $T_f = 3300$  K, the flame temperature of the lithium-air combustion calculated using the NASA CEA2 code,  $T_m$  is defined as:

$$T_m = (T_f + T_s) / 2 \quad (A1.17)$$

with  $T_s$  the droplet surface temperature. Results are shown in figure A1.5 where the droplet lifetime as a function of the environment temperature and the droplet diameter was compared with the convective time.

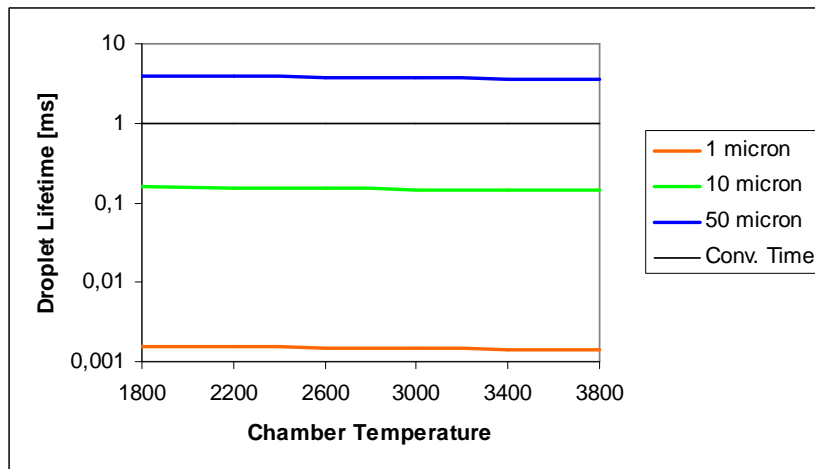
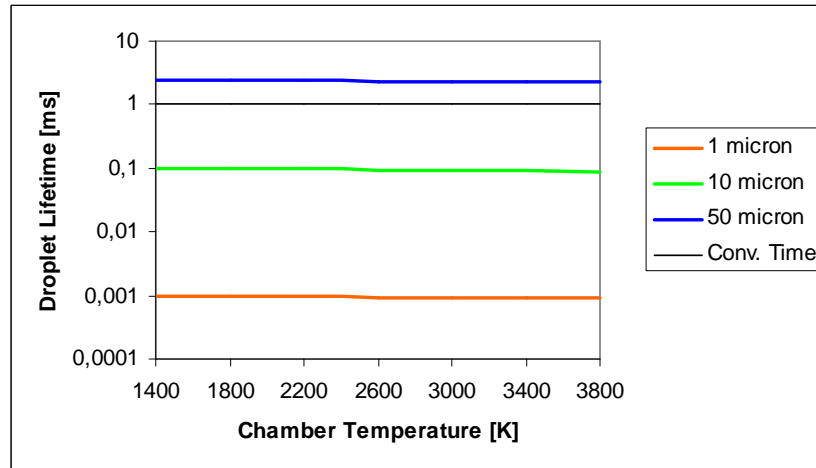


Fig. A1.5: Droplets lifetime

A more accurate evaluation of the gas characteristic was obtained using values of  $k_g$  and  $c_{pg}$  calculated using CEA600; results are shown in figure A1.6



**Fig. A1.6: Droplets lifetime (data obtained with CEA600)**

### A1.2 Extension to a convective environment

The last step of our investigation on lithium liquid droplets evaporation and combustion is to incorporate the convection effect into the model developed. We follow the approach suggested by Turns,<sup>71</sup> based on the “film theory”. The difference between this last and the preceding model consists in the replacement of the boundary conditions; that is the same boundary conditions used at infinity are now moved inward to a distance  $\delta_M$  for species and  $\delta_T$  for energy, see figure A1.7.

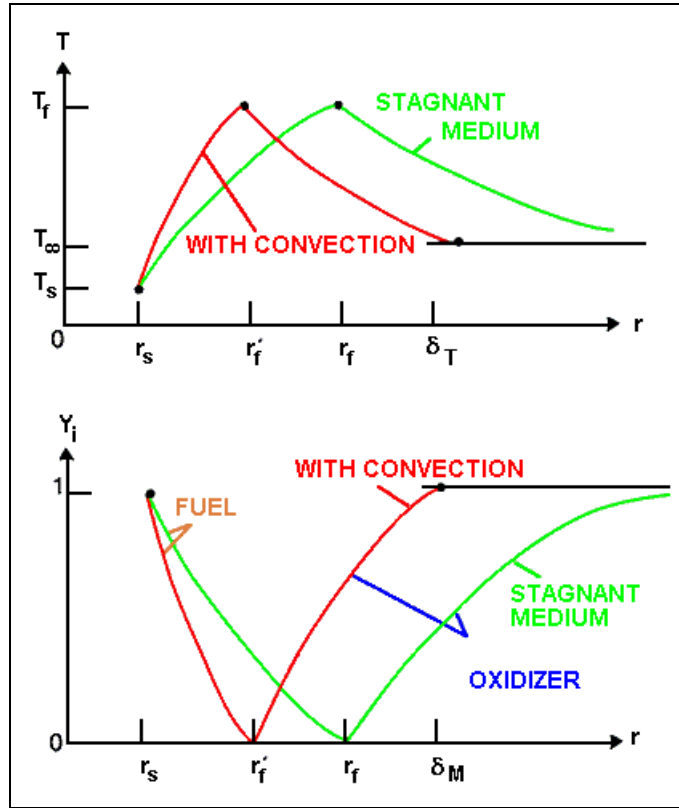


Fig A1.7: Effect of the convective environment

In figure A1.7, the film radius steepens the concentration and temperature gradients, so enhancing mass and heat transfer rates at the droplet surface. This means that convection increases the drop burning rate and lowers the characteristic time with respect to the preceding case (quiescent environment). The film radii are defined as:

$$\frac{\delta_T}{r_s} = \frac{Nu}{Nu - 2} \quad (A1.18)$$

where the Nusselt number physically represents the dimensionless temperature gradient at the droplet surface and

$$\frac{\delta_M}{r_s} = \frac{Sh}{Sh - 2} \quad (A1.19)$$

where the Sherwood number  $Sh$  is the dimensionless concentration at the surface. We can observe that for a quiescent environment  $Nu = 2$ ; in the limit  $\delta_T \rightarrow \infty$ , results agree with the boundary conditions used in the preceding case.

Assuming  $Sh = Nu$  (remembering that the Lewis number  $Le = 1$ ) a correlation to evaluate  $Nu$  is:

$$Nu = 2 + \frac{0.555 Re^{1/2} Pr^{1/3}}{\left[1 + 1.232 / (Re Pr^{4/3})\right]^{1/2}} \quad (A1.20)$$

were  $Re$  is based on the droplet diameter and the relative velocity, while the thermophysical properties can be calculated as in (A1.10 ; A1.12).

Finally the burning rate constant (A1.15) that can be extracted from this theory is:

$$K = Nu \frac{4 k_g}{\rho_L c_{pg}} \ln (B_{o,q} + 1) \quad (A1.21)$$

The impact of these more realistic assumption (considering the high flow speed into the chamber) can be shown by examining what happens to a droplet having a larger diameter than allowed by the analysis developed in the preceding sections. Assuming in fact the existence of 100  $\mu m$  diameter droplets, we can evaluate the time employed by one of these drops to reach, starting from rest, a velocity corresponding to 60% of the flow speed: this time, called relaxation time  $\tau_p$ , accounting for the stream turbulence, is defined by modifying the laminar relaxation time

$$\tau_{p,Stokes} = \frac{\rho_{Li} D^2}{18 \mu} \quad (A1.22)$$

with the term in squared brackets, becoming thus:<sup>78</sup>

$$\tau_p = \frac{\tau_{p,Stokes}}{\left[ 1 + 0.15 Re_d^{0.687} \right]} \quad (A1.23)$$

where  $Re_d$ ,  $\rho_{Li}$ ,  $D$  are respectively the Reynolds number of the droplet, the liquid lithium density and the droplet diameter. Using the same numerical values in the preceding section, the droplet relaxation time is of the order of  $10^{-4}$  seconds, that is smaller than the convective time; incidentally we can observe that calculated the corresponding acceleration, the distance covered by the drop during a time interval equal to the convective time is about 50 cm, showing that there is enough time for heating and combustion. Now if we calculate with (A1.21) and (A1.23) the  $Nu$  and  $K$  at the initial instant  $t_0 = 0$  and after  $t_1 = \tau_p$  seconds, we obtain for the droplet lifetime the results presented in figure A1.8:

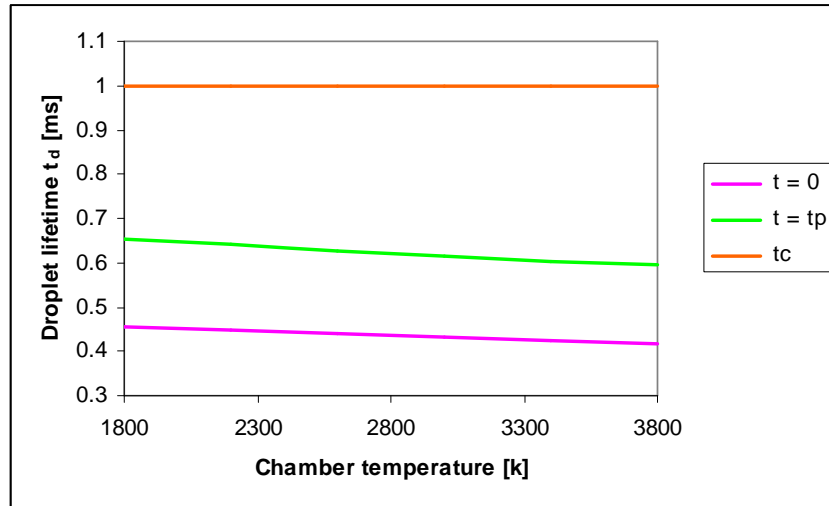


**Fig A1.8: 100  $\mu\text{m}$  droplet lifetime in convective environment**

Thus, despite the droplet size, its lifetime at the initial instants of the motion is of the same order of the relaxation time; and after a time interval corresponding to the relaxation time, the drop lifetime is still one half of the characteristic convective time. The lifetime is even shorter obviously when considering droplet having diameter smaller than 100  $\mu\text{m}$ .